

Flow Down a Wavy Inclined Plane

by

Kelly Anne Ogden

A thesis
presented to the University of Waterloo
in fulfillment of the
thesis requirement for the degree of
Master of Mathematics
in
Applied Mathematics

Waterloo, Ontario, Canada, 2011

© Kelly Anne Ogden 2011

I hereby declare that I am the sole author of this thesis. This is a true copy of the thesis, including any required final revisions, as accepted by my examiners.

I understand that my thesis may be made electronically available to the public.

Abstract

Under certain conditions, flow down an inclined plane destabilizes and a persistent series of interfacial waves develop. An interest in determining under what conditions a flow becomes unstable and how the interface develops has motivated researchers to derive several models for analyzing this problem.

The first part of this thesis compares three models for flow down a wavy, inclined plane with the goal of determining which best predicts features of the flow. These models are the shallow-water model (SWM), the integral-boundary-layer (IBL) model, and the weighted residual model (WRM). The model predictions for the critical Reynolds number for flow over an even bottom are compared to the theoretical value, and the WRM is found to match the theoretical value exactly. The neutral stability curves predicted by the three models are compared to two sets of experimental data, and again the WRM most closely matches the experimental data. Numerical solutions of the IBL model and the WRM are compared to numerical solutions of the full Navier-Stokes equations; both models compare well, although the WRM matches slightly better. Finally, the critical Reynolds numbers for the IBL model and the WRM for flow over a wavy incline are compared to experimental data. Both models give results close to the data and perform equally well. These comparisons indicate that the WRM most accurately models the flow.

In the second part of the thesis, the WRM is extended to include the effects of bottom heating and permeability. Based on the results of the first part of the thesis, the WRM is used, as it is expected to be the most realistic. The model is used to predict the effect of heating and permeability on the stability of the flow, and the results are compared to theoretical predictions from the Benney equation and to a perturbation solution of the Orr-Sommerfeld equation from the literature. The results indicate that the model does faithfully predict the theoretical critical Reynolds number with heating and permeability, and both effects destabilize the flow. Finally, numerical simulations of the model equations are compared to full numerical solutions of the Navier-Stokes equations for the case with bottom permeability. The results are found to agree, which indicates that the WRM remains appropriate when permeability is included.

Acknowledgements

I am grateful for the help of my supervisor, Serge D'Alessio, and his collaborator, J.P. Pascal. I would like to thank them, as well as H. Jasmine, for allowing me to contribute to a journal article, and for their collaboration on a paper that was published in a conference proceeding; the work that I contributed to these publications is included in my thesis. I am also thankful to the other professors in the UW Applied Math Fluids research group. I would like to acknowledge the financial support provided by NSERC.

Table of Contents

List of Figures	x
List of Tables	xi
1 Introduction	1
1.1 Problem Description	1
1.2 Outline	4
1.3 Literature Review	4
2 Governing Equations	7
2.1 Non-Dimensionalization	9
2.2 Stability	11
2.2.1 Orr-Sommerfeld Approach	12
2.2.2 Benney Approach	15
3 Models	18
3.1 Shallow Water Model	18
3.2 Integral-Boundary-Layer Model	19
3.3 Weighted Residual Model	21
3.4 Steady State Solutions	22
3.5 Model Stability	29
4 Numerical Solutions	31
4.1 Numerical Solutions of Model Equations	32
4.2 Numerical Solutions of the Full Navier-Stokes Equations	39

5	Results and Comparisons	45
5.1	Model Comparison	45
5.1.1	Critical Reynolds Number for the Even Bottom Case	46
5.1.2	Neutral Stability Curves	46
5.1.3	Simulation Results Compared to Full Navier-Stokes Numerical Solutions	50
5.1.4	Critical Reynolds Number with Bottom Topography	54
5.2	Effect of Surface Tension and Bottom Amplitude on Stability of Flow	56
6	Thermoporous Problem	59
6.1	Governing Equations and Boundary Conditions	60
6.2	Model Development	65
6.3	Steady-State Solutions	67
6.4	Linear Stability with an Even Bottom	73
6.4.1	Linear Stability using the Benney Equation	73
6.4.2	Linear Stability using the Model Equations	75
6.4.3	Comparison of Linear Stability Results	76
6.4.4	Effect of Heating and Porosity on Stability	77
6.5	Linear Stability with Bottom Topography	81
6.6	Numerical Simulation Results	90
6.6.1	Comparison to Full Navier-Stokes Numerical Solutions	93
7	Conclusions	95
	APPENDICES	98
A	Linear Stability over a Wavy Bottom	99
B	Effect of Surface Tension	104
	PERMISSIONS	108
	References	116

List of Figures

1.1	Problem setup for the case with an even bottom.	1
1.2	Problem setup for the case with bottom topography.	3
3.1	Numerical steady-state solutions for each model (top) for $Re = 1$, $\delta = 0.1$, $\cot \beta = 1$, $We = 5$, and $a_b = 0.1$, and numerical solutions for each model compared to the corresponding approximate analytical solution.	25
3.2	Numerical steady state-solutions compared with the approximate analytical solutions for $Re = 1$, $\delta = 0.1$, $\cot \beta = 1$, $We = 5$, and $a_b = 0.1$, top, and when one of the parameters is changed.	26
3.3	Numerical steady-state solutions for the weighted residual model for $Re = 1$, $\delta = 0.1$, $\cot \beta = 1$, $We = 5$, and $a_b = 0.1$ (top), and numerical solutions showing the effect of increasing one of the parameters. The left column shows the fluid layer thickness and the right column shows the interface location and the bottom topography.	28
4.1	Volume flow rate distribution for a case without surface tension, simulated using the weighted residual model, at various times (top), and final volume flow rate, (second from top), fluid thickness (third from top), and bottom and free surface (bottom), shown fully developed. The flow parameters are $Re = 2.28$, $a_b = 0.1$, $\delta = 0.1$, $\cot \beta = 1.5$, and $We = 0$	35
4.2	Volume flow rate distribution for a case without surface tension, simulated using the integral-boundary-layer model, at various times (top), and final volume flow rate, (second from top), fluid thickness (third from top), and bottom and free surface (bottom), shown fully developed. The flow parameters are $Re = 2.28$, $a_b = 0.1$, $\delta = 0.1$, $\cot \beta = 1.5$, and $We = 0$	36

4.3	Volume flow rate distribution for a case with surface tension, simulated using the weighted residual model, for various times (top), and final volume flow rate, (second from top), fluid thickness (third from top), and bottom and free surface (bottom), shown fully developed. The flow parameters are $Re = 2.28$, $a_b = 0.1$, $\delta = 0.1$, $\cot \beta = 1.5$, and $We = 20.04$	37
4.4	Volume flow rate distribution for a case with surface tension, simulated using the integral-boundary-layer model, for various times (top), and final volume flow rate, (second from top), fluid thickness (third from top), and bottom and free surface (bottom), shown fully developed. The flow parameters are $Re = 2.28$, $a_b = 0.1$, $\delta = 0.1$, $\cot \beta = 1.5$, and $We = 20.04$	38
4.5	A section of the mesh used for a CFX simulation of flow down an inclined plane.	41
4.6	Volume flow rate (top) and fluid interface and bottom surface (bottom) of fully developed flow. The flow parameters are $Re = 2.28$, $a_b = 0.1$, $\delta = 0.1$, $\cot \beta = 1.5$, and $We = 0$	42
4.7	Volume fraction contour plot of a section of the domain for the fully developed flow, showing one roll wave. The flow parameters are $Re = 2.28$, $a_b = 0.1$, $\delta = 0.1$, $\cot \beta = 1.5$, and $We = 0$	43
4.8	Velocity profile from CFX compared to model profile far from a wave (top) and in a wave (bottom). The flow parameters are $Re = 2.28$, $a_b = 0.1$, $\delta = 0.1$, $\cot \beta = 1.5$, and $We = 0$	44
5.1	Neutral stability curves for each model compared to experimental data. The flow parameters are $\nu = (5.02 \pm 0.05) \times 10^{-6} \frac{m^2}{s}$, $\gamma = (69 \pm 2) \times 10^{-3} \frac{N}{m}$, $\rho = 1.13 \frac{g}{cm^3}$, and $\beta = 5.6^\circ$	48
5.2	Neutral stability curves for each model compared to experimental data. The flow parameters are $\nu = 2.3 \times 10^{-6} \frac{m^2}{s}$, $\gamma = 67 \times 10^{-3} \frac{N}{m}$, $\rho = 1.07 \frac{g}{cm^3}$, and $\beta = 4.0^\circ$	49
5.3	Volume flow rate along the domain for IBL, WRM, and CFX. The flow parameters are $Re = 2.28$, $a_b = 0.1$, $\delta = 0.1$, $\cot \beta = 1.5$, and $We = 0$	51
5.4	Free surface height and bottom position along the domain for IBL, WRM, and CFX. The flow parameters are $Re = 2.28$, $a_b = 0.1$, $\delta = 0.1$, $\cot \beta = 1.5$, and $We = 0$	52
5.5	Volume flow rate along the domain for IBL, WRM, and CFX. The flow parameters are $Re = 2.28$, $a_b = 0.1$, $\delta = 0.1$, $\cot \beta = 1.5$, and $We = 5.05$	53
6.1	Models for flow over a porous layer	64

6.2	Fluid thickness h and interface temperature θ over one bottom wavelength for $a_b = 0.1$, $\delta = 0.1$, $\cot \beta = 1$, $W\acute{e} = 5$, and $Re = 1$; for cases with porosity, $\delta_1 = 0.1$, and for cases with heating, $Bi = Ma = 1$. The scaling $q_s = 1$ is used.	69
6.3	Fluid thickness h and interface temperature θ over one bottom wavelength for $a_b = 0.1$, $\delta = 0.1$, $\cot \beta = 1$, $W\acute{e} = 5$, $Bi = Ma = 1$, and $Re = 1$; for cases with porosity, $\delta_1 = 0.1$. The scaling $h_s = 1$ is used.	71
6.4	Fluid layer thickness and interface temperature over one bottom wavelength for $a_b = 0.1$, $\delta = 0.1$, $\cot \beta = 1$, $W\acute{e} = 100$, $Bi = Ma = 1$, $Re = 1$, and $\delta_1 = 0$	72
6.5	Fluid layer thickness and interface temperature over one bottom wavelength for $a_b = 0.1$, $\delta = 0.1$, $\cot \beta = 1$, $W\acute{e} = 100$, $Bi = Ma = 1$, $Re = 1$, and $\delta_1 = 0.2$. The scaling $q_s = 1$ is used.	72
6.6	Effect of increasing δ_1 on the critical Reynolds number.	78
6.7	Effect of increasing Ma on the critical Reynolds number.	79
6.8	Effect of increasing Ma and Bi together on the critical Reynolds number.	79
6.9	Effect of increasing Bi on the critical Reynolds number.	80
6.10	Effect of increasing $\cot \beta$ for the isothermal, impermeable case where $\delta = 0.05$ and $W\acute{e} = 5$, with even bottom (top), $a_b = 0.3$ (middle), and $a_b = 0.4$ (bottom).	84
6.11	Effect of increasing a_b for the isothermal, impermeable case where $\delta = 0.05$ and $W\acute{e} = 5$, with $\cot \beta = 3$ (top), $\cot \beta = 4$ (middle), and $\cot \beta = 5$ (bottom).	85
6.12	Effect of increasing $W\acute{e}$ for the isothermal, impermeable case where $\delta = 0.05$ and $\cot \beta = 4$, with $a_b = 0.0$ (top), $a_b = 0.3$ (middle), and $a_b = 0.4$ (bottom).	86
6.13	Effect of increasing δ for the isothermal, impermeable case where $W\acute{e} = 5$ and $\cot \beta = 4$, with $a_b = 0.3$ (top), and $a_b = 0.4$ (bottom).	87
6.14	Effect of increasing δ_1 for the case where $\delta = 0.05$, $W\acute{e} = 5$, $a_b = 0.4$, $\cot \beta = 4$, $Pr = 7$, and $Bi = 1$, with $Ma = 0.2$, (top) and $Ma = 0$, (bottom).	88
6.15	Effect of increasing Ma for the case where $\delta = 0.05$, $W\acute{e} = 5$, $\cot \beta = 4$, $Pr = 7$, $Bi = 1$, and $\delta_1 = 0.1$, with $a_b = 0.3$, (top) and $a_b = 0.4$, (bottom).	89
6.16	Volume flow rate evolution in time for a case with heating and permeability. $Re = 1.0$, $\delta = 0.1$, $\cot \beta = 0.5$, $W\acute{e} = 100$, $a_b = 0.2$, $Bi = Ma = 1$, and $\delta_1 = 0.1$. The WRM with the scaling $q_s = 1$ is used.	91

6.17	Comparison between a case with heating and bottom permeability and an impermeable, isothermal case at $t=200$. Both have $Re = 1.0$, $\delta = 0.1$, $\cot \beta = 0.5$, $We = 100$, $a_b = 0.2$, and a domain length of ten bottom wavelengths. The case with heating and permeability has $Bi = Ma = 1$ and $\delta_1 = 0.1$. The WRM with the scaling $q_s = 1$ is used.	92
6.18	CFX and WRM results for a case with bottom porosity. The flow parameters are $Re = 1.75$, $\delta = 0.089$, $\delta_1 = 0.14$, $\cot \beta = 1.38$, and $We = Ma = Bi = a_b = 0$	94

List of Tables

5.1	Comparison between experimental, numerical and theoretical values of Re_{crit} for a wavy-incline case with $\delta = 0.1$	56
6.1	Comparison of critical Reynolds number for limiting cases to Orr-Sommerfeld result	77

Chapter 1

Introduction

1.1 Problem Description

Flow down an inclined plane has been studied extensively in the past, and yet there continue to be many interesting features of the flow to analyze [1, 2]. This type of flow is a fascinating problem to investigate because, although the problem setup is simple, the dynamics of an unstable flow are not. Furthermore, there are many applications, in both engineering and nature, for this type of flow.

The problem is that of a thin fluid layer flowing down an inclined plane. The flow is driven by gravity, and the gravitational force is balanced by the friction between the bottom surface and the fluid. A stream-wise cross-section of the flow is shown in figure 1.1.

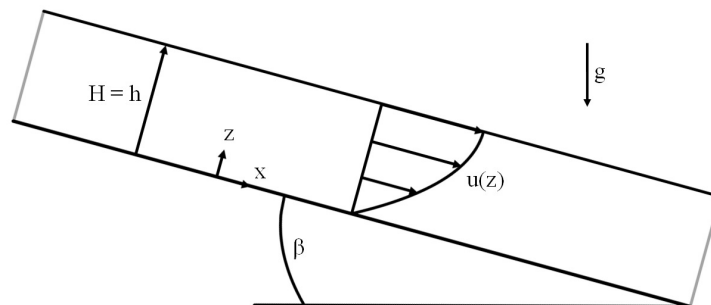


Figure 1.1: Problem setup for the case with an even bottom.

This flow has a simple steady-state solution, called the Nusselt Solution, which is an exact solution to the Navier-Stokes equations. The solution satisfying the conditions

$$\frac{\partial u}{\partial z} = 0 \quad \text{at } z = h , \quad (1.1)$$

$$u = w = 0 \quad \text{at } z = 0 , \quad (1.2)$$

and

$$p = P_a \quad \text{at } z = h , \quad (1.3)$$

is

$$u(z) = \frac{g}{\nu} \sin(\beta)z \left(h - \frac{z}{2} \right) , \quad (1.4)$$

$$w = 0 , \quad (1.5)$$

and

$$p(z) = p_{atm} + (z - h)\rho g \cos(\beta) , \quad (1.6)$$

where $u(z)$ is the stream-wise velocity, w is the cross-stream velocity, $p(z)$ is the pressure, and h is the fluid thickness, which is uniform. The angle of inclination is given by β , the fluid density and kinematic viscosity are ρ and ν , respectively, and g is gravity. A cross-section of this flow, with the velocity profile shown, can also be seen in figure 1.1.

Although a steady-state solution exists, it is unstable to long-wave disturbances under certain conditions. When the flow is unstable, perturbations grow, interact, and can form a series of individual waves called roll waves, which maintain their shape as they move along the free surface. The conditions under which the flow is stable and the shape of the interface that develops when the flow destabilizes are the focus of this thesis. In the first part of the thesis, the case where the flow is isothermal and the inclined plane is impermeable, but can have topography, is considered. Three models that can be used to describe the flow are compared by considering how well they predict the critical Reynolds number, the neutral stability curve, and the time evolution of the free surface. In the second part of the thesis, the most accurate of the three models is extended to include a wavy, heated, permeable, inclined plane, and the effect of heating and permeability are considered. The flow setup with a wavy bottom is shown in figure 1.2, where ζ describes the bottom topography.

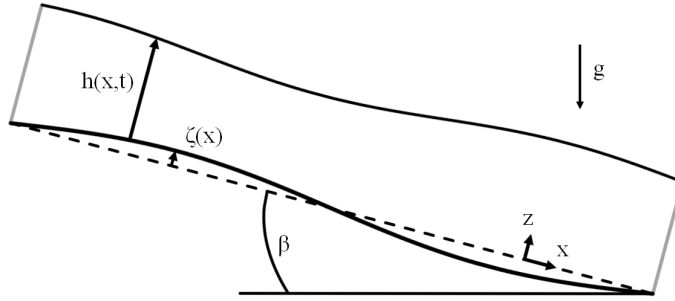


Figure 1.2: Problem setup for the case with bottom topography.

Applications of this problem include environmental phenomena such as mudslides and rain water flow over the ground; engineering applications such as aqueducts, manufacturing coatings, and food processing also exhibit this type of flow [3–7]. Analytical models for the flow are useful because they help predict key features of the flow, such as under what conditions it will become unstable and how the shape of the surface will develop after this happens. These are important predictions to make because the roll waves that are formed when the flow becomes unstable can overflow channel walls or damage measuring equipment in engineering situations. Alternatively, roll waves can be used to increase the heat transfer from a surface by increasing the interface area. In environmental flows, the roll waves result in more destructive surges of fluid due to the increased momentum associated with the wave [3]. Hence, models that correctly predict features of the flow can be used to determine when roll waves occur, and help prevent the destruction they might cause or take advantage of the benefits of their existence.

Extending the problem to include bottom heating and permeability makes the model more versatile to include flows such as rain water over the ground, where the ground is permeable, and flows involved in food processing [8]. Including heating allows the model to be used to predict the effectiveness of heat exchangers. Another application for the model including heating and permeability is modelling tear film over a contact lens as investigated by Nong and Anderson [9]. The contact lens is permeable and thus requires a model including bottom permeability. Furthermore, since the eye is warmer than the surrounding air, adding bottom heating will make the model more realistic.

1.2 Outline

Chapter 2 introduces the governing equations, which are the two-dimensional Navier-Stokes equations, and the corresponding boundary conditions. It also presents two stability analyses for the even bottom case using the Orr-Sommerfeld equation and the Benney equation. Chapter 3 presents the derivations of three models that describe the flow over a wavy bottom and methods used to find their steady-state solutions. Further, the stability predictions made by each of the three models for the case of the even bottom are discussed. The numerical solution procedure used to solve the model equations and compute the time evolution of the free surface is detailed in Chapter 4. The use of the software package CFX to solve the full Navier-Stokes equations for this problem is also discussed in Chapter 4. In Chapter 5, the three models are compared using the stability results and transient simulations to determine which model best describes the flow. Also in Chapter 5, the effects of bottom topography and surface tension on the stability of the flow are discussed. In Chapter 6, the problem is extended to include the effects of bottom permeability and bottom heating. The most accurate model, as determined in Chapter 5, is developed for this extended problem, and the stability and interface evolution of this problem are investigated.

1.3 Literature Review

The first experiments simulating the development of interfacial waves in thin film flow over an inclined plane, conducted in a laboratory setting, were performed by Kapitza [10] in 1948, and additional work was then conducted by Kapitza and Kapitza [11] in 1949. The problem was approached mathematically in 1949 by Dressler [12], who developed a periodic mathematical solution describing roll waves that appear on the surface of unstable flows. Dressler used the shallow-water equations and focused his study on the behaviour of the fully developed interfacial waves. His solution is pieced together from continuous segments through shocks, and he considers both laminar and turbulent flow.

In 1957, Benjamin [1] studied the stability of laminar thin film flow down an inclined plane. He calculated the critical Reynolds number using a perturbation solution to the Orr-Sommerfeld equation by assuming perturbations of small wavenumber are the most unstable. This assumption, which has since been shown to be correct for an even bottom incline [1, 13], was initially based on experimental evidence. Yih [2] confirmed Benjamin's long wave result in 1963, and also considered small Reynolds number and large wavenumber flows. In 1966, Benney [14] developed a single equation that governs the fluid layer thickness for stable flows and flows near the onset of instability. The equation becomes

invalid shortly after the onset of instability, and therefore cannot be used to predict how roll waves develop. However, it can be used in conjunction with a linear stability analysis to predict the critical Reynolds number. It also offers a simpler approach than the Orr-Sommerfeld method for obtaining the critical Reynolds number.

Shkadov [15] developed the integral-boundary-layer model in 1967. This model, which is one of the three considered in this work, uses the boundary-layer approximations and assumes a parabolic velocity profile to eliminate the depth dependence of the equations. The motivation for developing this model was to include non-linear effects in the mathematical formulation of the problem with the goal of closely matching experimental data. The model can be used to simulate the development of the fluid interface with time.

More recently, experimental data have been collected describing the stability of the flow. Liu et al. [16] collected data describing two-dimensional instabilities, including points along the neutral stability curve, which can be used to evaluate the validity of model predictions. Liu et al. [17] also conducted experiments considering both three- and two-dimensional instabilities, and collected additional data for the neutral stability curve of the flow. Additionally, Wierschem et al. [18] collected critical Reynolds number values for various flows while experimenting with thin film flow over a wavy bottomed inclined plane.

Numerical Simulations of flow down an inclined plane have been carried out by Ramaswamy et al. [19] in 1996, who applied a finite element method to solve the full two-dimensional governing equations of the problem, rather than considering a simplified model.

In a series of papers from 1998 to 2002, Ruyer-Quil and Manneville [20–22] developed the weighted-residual model, which combines the idea of the integral-boundary-layer model with the weighted residual method. They tested a variety of weight functions to determine which one allows the model to predict the theoretical critical Reynolds number. Further, they compare the neutral stability curve of this derived model to the experimental data collected by Liu et al. [16] and Liu et al. [17] and they calculate the development of roll waves using their model. In their second paper, they also extend the model to include three-dimensional effects [21]. Ruyer-Quil and Manneville [20] also noted the importance of including second-order terms in the model to reproduce important features of the flow.

Balmforth and Mandre [5] added bottom topography to the problem and studied this case using a shallow-water model. The shallow-water model is developed from the shallow-water equations with terms added to account for viscosity and bottom friction. Balmforth and Mandre focus on the case with turbulence, but also repeat their analysis for laminar flow.

They conduct a multiple-scales asymptotic analysis to investigate the effect of bottom topography on the stability of the flow, although their result is incorrect due to limitations of the shallow-water model [3]. They also develop an amplitude equation to establish the stability of the fully developed interfacial waves. The effect of bottom topography on the flow has also been investigated using the weighted residual model by D'Alessio et al. [3].

The effects of heating on thin film flow down a wavy incline have recently been considered. In 2003, Kalliadasis et al. [23] used a first-order integral-boundary-layer model to study flow over a wavy incline having a constant bottom temperature that exceeds that of the surrounding fluid. Ruyer-Quil et al. [24] and Scheid et al. [25] applied the second-order weighted residual model to the problem, which more accurately predicts the critical Reynolds number of the flow. Trevelyan et al. [7] considered both constant temperature and constant heat flux bottom boundary conditions using the weighted residual model, and conclude that in the long wave limit, heating has a destabilizing effect on the flow in both cases. The problem with bottom heating, using the constant temperature bottom boundary condition, and including bottom topography, was analyzed by D'Alessio et al. [13].

A thin film flow over a permeable inclined plane was considered by Pascal in 1999 [26], who performed a series solution to the Orr-Sommerfeld equation to determine the effect of bottom permeability on the stability of the flow. It was shown that bottom permeability destabilizes the flow. Later, Pascal and D'Alessio [8] applied the weighted residual model to flow over a permeable, wavy inclined plane to investigate the stability and interfacial wave development. Both of these studies make use of the bottom boundary condition first formulated by Beavers and Joseph [27], and extended it to uneven bottom topography using the work by Saffman [28]. Nong and Anderson [9] present a different model for flow over a permeable surface applied to the specific problem of a tear layer over a contact lens, which highlights the applicability of this problem. Craster and Matar [29] give an extensive review on thin film flows, including the basic problem of a gravity driven flow down an inclined plane, the effects of heating and bottom permeability, as well as several other related problems.

Very recently, Sadiq et al. [4] published a paper investigating the combined effects of heating and permeability. They perform a series solution to the Orr-Sommerfeld equation, showing the combined effect of heating and permeability. Their work provides an important comparison for the current study where the weighted residual model is applied to the problem including both heating and permeability.

Chapter 2

Governing Equations

The first problem considered is the two dimensional flow of a thin film down a wavy, isothermal, impermeable, inclined plane. Although disturbances will be three-dimensional in reality, this work will focus on two-dimensional instabilities. For the purposes of determining when the flow becomes unstable, considering only the two-dimensional case is justified because two-dimensional perturbations are more unstable than their three-dimensional counterparts [21, 30].

The governing equations of the flow are the two-dimensional Navier-Stokes equations, which are

$$\frac{\partial u}{\partial t} + u \frac{\partial u}{\partial x} + w \frac{\partial u}{\partial z} = -\frac{1}{\rho} \frac{\partial p}{\partial x} + g \sin(\beta) + \nu \left(\frac{\partial^2 u}{\partial x^2} + \frac{\partial^2 u}{\partial z^2} \right) , \quad (2.1)$$

$$\frac{\partial w}{\partial t} + u \frac{\partial w}{\partial x} + w \frac{\partial w}{\partial z} = -\frac{1}{\rho} \frac{\partial p}{\partial z} - g \cos(\beta) + \nu \left(\frac{\partial^2 w}{\partial x^2} + \frac{\partial^2 w}{\partial z^2} \right) , \quad (2.2)$$

and the continuity equation,

$$\frac{\partial u}{\partial x} + \frac{\partial w}{\partial z} = 0 . \quad (2.3)$$

The boundary conditions along an impermeable bottom are the no normal flow condition given by

$$\vec{v} \cdot \hat{N} = 0 , \quad (2.4)$$

and the no slip condition given by

$$\vec{v} \cdot \hat{T} = 0, \quad (2.5)$$

where \hat{N} is the unit outward normal vector to the bottom surface, defined by

$$\hat{N} = \frac{(-\zeta', 1)^T}{\sqrt{1+(\zeta')^2}}, \quad (2.6)$$

and \hat{T} is the unit tangent vector to the bottom surface, defined by

$$\hat{T} = \frac{(1, \zeta')^T}{\sqrt{1+(\zeta')^2}}. \quad (2.7)$$

These boundary conditions reduce to

$$u = w = 0 \quad \text{at } z = \zeta, \quad (2.8)$$

for this problem.

At the fluid interface, the kinematic and dynamic boundary conditions are applied. The dynamic conditions in vector form, which ensure continuity of normal and tangential stress respectively, are

$$\left. \begin{aligned} P_a + \hat{n} \cdot \tau \cdot \hat{n} &= -\sigma \vec{\nabla} \cdot \hat{n} \\ \hat{n} \cdot \tau \cdot \hat{t} &= 0 \end{aligned} \right\} \text{at } z = \eta. \quad (2.9)$$

The normal stress condition requires that the normal stress at the interface within the fluid layer is balanced by the ambient pressure outside of the fluid layer and the normal force on the interface due to surface tension and the curvature of the interface. The tangential stress condition required that tangential stresses at the interface and within the fluid layer are balanced by tangential stresses applied by surface tension; it is assumed that the ambient gas does not apply tangential stresses on the fluid. Here, P_a is the ambient pressure outside of the fluid flow, σ is the surface tension, $\eta = h + \zeta$ is the free surface location, and τ is the symmetric stress tensor, defined by

$$\tau = \begin{pmatrix} -P + 2\mu u_x & \mu(u_z + w_x) \\ \mu(u_z + w_x) & -P + 2\mu w_z \end{pmatrix}, \quad (2.10)$$

where μ is the dynamic viscosity of the fluid and P is the pressure in the fluid. The vectors \hat{n} and \hat{t} are the outward facing normal vectors at the fluid interface, defined by

$$\hat{n} = \frac{(-(\frac{\partial \eta}{\partial x}), 1)^T}{\sqrt{1+(\frac{\partial \eta}{\partial x})^2}}, \quad (2.11)$$

and

$$\hat{t} = \frac{(1, \frac{\partial \eta}{\partial x})^T}{\sqrt{1 + (\frac{\partial \eta}{\partial x})^2}}. \quad (2.12)$$

Substituting equations (2.10) to (2.12) into equation (2.9), these conditions become

$$2 \frac{\partial \eta}{\partial x} \left(\frac{\partial w}{\partial z} - \frac{\partial u}{\partial x} \right) + \left(1 - \left(\frac{\partial \eta}{\partial x} \right)^2 \right) \left(\frac{\partial u}{\partial z} + \frac{\partial w}{\partial x} \right) = 0 \quad \text{at } z = \eta, \quad (2.13)$$

which expresses continuity of tangential stress, and

$$\frac{\sigma \frac{\partial^2 \eta}{\partial x^2}}{\left(1 + \left(\frac{\partial \eta}{\partial x} \right)^2 \right)^{\frac{3}{2}}} - P_a + P - \frac{2\mu}{\left(1 + \left(\frac{\partial \eta}{\partial x} \right)^2 \right)} \left[\frac{\partial u}{\partial x} \left(\frac{\partial \eta}{\partial x} \right)^2 + \frac{\partial w}{\partial z} - \frac{\partial \eta}{\partial x} \left(\frac{\partial u}{\partial z} + \frac{\partial w}{\partial x} \right) \right] = 0 \quad \text{at } z = \eta, \quad (2.14)$$

which expresses continuity of normal stress. In these equations, η is the free surface location, which can be a function of position, x , and time, t .

The kinematic condition, which states that a fluid particle on the interface must remain on the interface, is

$$w = \frac{\partial \eta}{\partial t} + u \frac{\partial \eta}{\partial x} \quad \text{at } z = \eta. \quad (2.15)$$

In determining the boundary conditions, the simplifying assumption that the ambient fluid above the fluid layer is a gas and therefore has a negligible effect on the fluid flow, is made. For this to be valid, the gas must have a much smaller viscosity, μ , and density than the fluid of interest, which is true for most liquid-gas interfaces.

2.1 Non-Dimensionalization

The equations can be cast in dimensionless form and will involve dimensionless parameters such as the Reynolds number, Re , the Weber number, We , and a small shallowness parameter δ . The Reynolds number characterizes the importance of the inertial forces, the Weber number characterizes the importance of surface tension, and the parameter δ measures the thinness of the fluid layer. It is assumed that the fluid layer thickness is much less than the characteristic bottom length, making δ a small parameter; the other parameters are assumed to be $O(1)$. The parameters are defined as

$$Re = \frac{Q}{\nu}, \quad We = \frac{\sigma H}{\rho Q^2}, \quad \delta = \frac{H}{l}, \quad (2.16)$$

where Q is the characteristic volume flow rate, σ is the surface tension, H is the characteristic fluid layer thickness, and l is a characteristic length in the flow direction. For a wavy bottom, l can be taken to be the wavelength of the bottom topography.

If the characteristic fluid thickness for flow over an even bottom is chosen to be H , then the scales for the flow rate, Q , and the velocity, U , are given by

$$Q = \frac{H^3 \rho g \sin \beta}{3\mu}, \quad U = \frac{Q}{H} = \frac{H^2 \rho g \sin \beta}{3\mu}. \quad (2.17)$$

The scale for velocity, U , comes from the average of the velocity of flow over an even bottom incline, which is given in equation (1.4). The scale for volume flow rate is given by $Q = UH$. The non-dimensionalized continuity and x - and z - momentum equations are then

$$\frac{\partial u}{\partial x} + \frac{\partial w}{\partial z} = 0, \quad (2.18)$$

$$\delta Re \left(\frac{\partial u}{\partial t} + u \frac{\partial u}{\partial x} + w \frac{\partial u}{\partial z} \right) = -\delta Re \frac{\partial P}{\partial x} + 3 + \delta^2 \frac{\partial^2 u}{\partial x^2} + \frac{\partial^2 u}{\partial z^2}, \quad (2.19)$$

$$\delta^2 Re \left(\frac{\partial w}{\partial t} + u \frac{\partial w}{\partial x} + w \frac{\partial w}{\partial z} \right) = -Re \frac{\partial P}{\partial z} - 3 \cot \beta + \delta^3 \frac{\partial^2 w}{\partial x^2} + \delta \frac{\partial^2 w}{\partial z^2}, \quad (2.20)$$

respectively. Here, the pressure has been non-dimensionalized using ρU^2 .

The dynamic boundary conditions when non-dimensionalized become

$$-4\delta^2 \frac{\partial \eta}{\partial x} \frac{\partial u}{\partial x} + \left(1 - \delta^2 \left(\frac{\partial \eta}{\partial x} \right)^2 \right) \left(\frac{\partial u}{\partial z} + \delta^2 \frac{\partial w}{\partial x} \right) = 0 \quad \text{at } z = \eta, \quad (2.21)$$

for the tangential stress condition, and

$$\begin{aligned} & \frac{\delta^2 We \frac{\partial^2 \eta}{\partial x^2}}{\left(1 + \delta^2 \left(\frac{\partial \eta}{\partial x} \right)^2 \right)^{\frac{3}{2}}} + p \\ &= \frac{2}{Re \left(1 + \delta^2 \left(\frac{\partial \eta}{\partial x} \right)^2 \right)} \left[\delta^3 \frac{\partial u}{\partial x} \left(\frac{\partial \eta}{\partial x} \right)^2 + \delta \frac{\partial w}{\partial z} - \delta \frac{\partial \eta}{\partial x} \left(\frac{\partial u}{\partial z} + \delta^2 \frac{\partial w}{\partial x} \right) \right] \quad \text{at } z = \eta, \end{aligned} \quad (2.22)$$

for the normal stress condition, where $p = P - P_a$.

Next, only terms to $O(\delta^2)$ are retained so as to capture the essential physics of the problem. Higher order terms do not make a significant difference in the predictions of the models [3, 22]. To second order, the governing equations are

$$\frac{\partial u}{\partial x} + \frac{\partial w}{\partial z} = 0, \quad (2.23)$$

$$\delta Re \left(\frac{\partial u}{\partial t} + u \frac{\partial u}{\partial x} + w \frac{\partial u}{\partial z} \right) = -\delta Re \frac{\partial p}{\partial x} + 3 + \delta^2 \frac{\partial^2 u}{\partial x^2} + \frac{\partial^2 u}{\partial z^2}, \quad (2.24)$$

$$\delta^2 Re \left(\frac{\partial w}{\partial t} + u \frac{\partial w}{\partial x} + w \frac{\partial w}{\partial z} \right) = -Re \frac{\partial p}{\partial z} - 3 \cot \beta + \delta \frac{\partial^2 w}{\partial z^2}. \quad (2.25)$$

The dynamic boundary conditions to second order are

$$\left. \begin{aligned} p - \frac{2\delta}{Re} \frac{\partial w}{\partial z} + \delta^2 We \frac{\partial^2 (h+\zeta)}{\partial x^2} = 0 \\ \frac{\partial u}{\partial z} - 4\delta^2 \frac{\partial (h+\zeta)}{\partial x} \frac{\partial u}{\partial x} + \delta^2 \frac{\partial w}{\partial x} = 0 \end{aligned} \right\} \text{ at } z = \eta. \quad (2.26)$$

Using $\eta = h + \zeta$, the non-dimensionalized kinematic condition takes the form

$$w = \frac{\partial h}{\partial t} + u \frac{\partial}{\partial x} (h + \zeta) \quad \text{at } z = \eta. \quad (2.27)$$

The no-slip conditions remain

$$u = w = 0 \quad \text{at } z = \zeta. \quad (2.28)$$

2.2 Stability

The conditions under which the flow is stable can be found by determining the critical Reynolds number. When the Reynolds number is increased beyond this value, the flow becomes unstable to perturbations of a particular wavenumber. It has been shown by Yih [2] that, for flow over an even bottom, perturbations having long wavelengths are the most unstable; this has been observed experimentally and shown by calculating neutral stability curves for the flow [1, 2]. Because of this, the critical Reynolds number can be found by allowing the perturbation wavenumber, k , to go to zero. These perturbations then grow and combine, and can eventually form roll waves. The critical Reynolds number for flow over an even bottomed incline can be found using the Orr-Sommerfeld equation or by developing a Benney-type equation [14] and performing a linear stability analysis. The details of these two methods are given in the following sections, and their results are then compared.

2.2.1 Orr-Sommerfeld Approach

The Orr-Sommerfeld equation for flow over an even incline is developed using the non-dimensionalized governing equations and boundary conditions, equations (2.23) to (2.25) and (2.26) to (2.28). These equations can be solved to find the steady-state solution for streamwise velocity, $\bar{u}(z)$, and pressure, $\bar{p}(z)$, given by

$$\begin{aligned}\bar{u}(z) &= 3z \left(1 - \frac{z}{2}\right) \\ \bar{p}(z) &= (1 - z)3\frac{\cot\beta}{Re}.\end{aligned}\tag{2.29}$$

In the governing equations, each flow variable is replaced with the steady-state solution plus a perturbation. The scaling is chosen so that the steady state solution for the fluid layer thickness is $h = 1$. It follows from the continuity equation and the no-slip conditions that the steady-state vertical velocity is $w = 0$. All other steady-state variables are functions of only z because the physical setup does not change along the flow direction. Therefore, the variables are replaced with the following:

$$\begin{aligned}h &= 1 + \hat{\eta}(x, t), \\ u &= \bar{u}(z) + \hat{u}(x, z, t), \\ w &= \hat{w}(x, z, t), \\ p &= \bar{p}(z) + \hat{p}(x, z, t).\end{aligned}\tag{2.30}$$

For small perturbations, the momentum equations can be linearized in the perturbed variables to give

$$\begin{aligned}\frac{\partial \hat{u}}{\partial t} + \bar{u}\frac{\partial \hat{u}}{\partial x} + \hat{w}\frac{d\bar{u}}{dz} &= -\frac{\partial \hat{p}}{\partial x} + \frac{1}{\delta Re}\frac{\partial^2 \hat{u}}{\partial z^2}, \\ \frac{\partial \hat{w}}{\partial t} + \bar{u}\frac{\partial \hat{w}}{\partial x} &= -\frac{1}{\delta^2}\frac{\partial \hat{p}}{\partial z} + \frac{1}{\delta Re}\frac{\partial^2 \hat{w}}{\partial z^2}.\end{aligned}\tag{2.31}$$

Substituting equations (2.29) and (2.30) into the boundary conditions, equations (2.26) to (2.28), linearizing, and using the steady-state solution, the following boundary conditions are found

$$\left. \begin{aligned}\delta^2 \frac{\partial \hat{w}}{\partial x} + \frac{\partial \hat{u}}{\partial z} &= 3\hat{\eta}, \\ \hat{w} &= \frac{\partial \hat{\eta}}{\partial t} + \frac{3}{2}\frac{\partial \hat{\eta}}{\partial x}, \\ \hat{p} &= 3\hat{\eta}\frac{\cot\beta}{Re} - 2\frac{\delta}{Re}\frac{\partial \hat{w}}{\partial z} + \delta^2 We\frac{\partial^2 \hat{\eta}}{\partial x^2}\end{aligned}\right\} \text{ at } z = 1.\tag{2.32}$$

Next, the stream function is introduced. It is defined by

$$\hat{u} = \frac{\partial \psi}{\partial z} \quad , \quad \hat{w} = -\frac{\partial \psi}{\partial x} \quad . \quad (2.33)$$

The form of ψ is assumed to be

$$\psi = \phi(z) e^{ik(x-ct)} \quad . \quad (2.34)$$

Substituting this into equation (2.31) and combining the two momentum equations to eliminate pressure gives the Orr-Sommerfeld equation,

$$\frac{1}{\delta Re} \phi^{(iv)} + \left(ikc - \frac{\delta k^2}{Re} - 3z \left(1 - \frac{z}{2} \right) ik \right) \phi'' + \left(3z \left(1 - \frac{z}{2} \right) ik^3 \delta^2 - 3ik + ik^3 \delta^2 c \right) \phi = 0 \quad , \quad (2.35)$$

where the primes denote derivatives with respect to z . The tangential stress boundary condition, which is the first condition in equation (2.32), is used to find $\hat{\eta}$, and the pressure is found by integrating the x -momentum equation. These are then substituted into the other two conditions in equation (2.32) to find the boundary conditions for the Orr-Sommerfeld equation. The boundary conditions are

$$\left. \begin{aligned} \frac{d^2 \phi}{dz^2} + \left(k^2 \delta^2 - \frac{3}{c - \frac{3}{2}} \right) \phi &= 0 \\ \frac{1}{i \delta Re} \frac{d^3 \phi}{dz^3} + k \left(c - \frac{3}{2} + \frac{2 \delta ik}{Re} \right) \frac{d\phi}{dz} - k \left(\frac{\delta^2 We k^2}{c - \frac{3}{2}} + \frac{3 \cot \beta}{Re \left(c - \frac{3}{2} \right)} \right) \phi &= 0 \end{aligned} \right\} \text{ at } z = 1 \quad , \quad (2.36)$$

and

$$\phi = \phi_z = 0 \quad \text{at } z = 0 \quad . \quad (2.37)$$

The problem is now posed as an eigenvalue problem where the real part of c , $\Re(c)$, denotes the phase speed of the disturbances, and $k \Im(c)$, where $\Im(c)$ is the imaginary part of c , gives the growth rate. Therefore, the critical Reynolds number is found by setting $\Im(c) = 0$ and allowing k to go to zero as previously explained. This motivates a perturbation solution where ϕ and c are expanded in powers of the wavenumber k to give

$$\begin{aligned} \phi &= \phi_0 + k \phi_1 + O(k^2) \\ c &= c_0 + k c_1 + O(k^2) \end{aligned} \quad . \quad (2.38)$$

Substituting these into equations (2.35) to (2.37) leads to a hierarchy of problems at each order of k . The $O(1)$ problem is

$$\begin{aligned}
\phi_0^{(iv)} &= 0, \\
\phi_0(0) &= 0, \\
\phi_0'(0) &= 0, \\
\phi_0''(1) - \frac{3}{c_0 - \frac{3}{2}}\phi_0(1) &= 0, \\
\phi_0'''(1) &= 0,
\end{aligned} \tag{2.39}$$

which can be solved to give

$$\begin{aligned}
\phi_0 &= z^2, \\
c_0 &= 3.
\end{aligned} \tag{2.40}$$

This gives the phase speed of disturbances with wavenumbers approaching zero. However, because information about the imaginary part of c is required to determine the critical Reynolds number, the problem at the next order of k is considered. The $O(k)$ problem gives

$$\begin{aligned}
\frac{\phi_1^{(iv)}}{\delta Re} + i \left(c_0 - 3z \left(1 - \frac{z}{2} \right) \right) \phi_1'' - 3i\phi_1 &= 0, \\
\phi_1(0) &= 0, \\
\phi_1'(0) &= 0, \\
\phi_1''(1) - \frac{3}{c_0 - \frac{3}{2}}\phi_1(1) + \frac{3c_1}{\left(c_0 - \frac{3}{2} \right)^2}\phi_0(1) &= 0, \\
\frac{\phi_1'''(1)}{i\delta Re} + 3 - \frac{3 \cot \beta}{2 Re} &= 0.
\end{aligned} \tag{2.41}$$

This problem can be solved and yields

$$c_1 = i\delta Re \left(\frac{6}{5} - \frac{\cot \beta}{Re} \right). \tag{2.42}$$

Setting $c_1 = 0$ gives the following critical Reynolds number,

$$Re_{crit} = \frac{5}{6} \cot \beta . \quad (2.43)$$

Next, another approach for determining the critical Reynolds number is presented.

2.2.2 Benney Approach

The Benney equation represents an evolution equation for the free surface of flow over an even bottom; it is only valid near the onset of instability and can also be used to determine the critical Reynolds number. The Benney equation can also be derived from the governing equations (2.23) to (2.25) and boundary conditions (2.26) and (2.28). First, the variables u , w , and p are expanded in powers of δ about the steady-state solutions u_s , w_s , and p_s :

$$\begin{aligned} u &= u_s + \delta u_1 + \delta^2 u_2 + \dots , \\ w &= w_s + \delta w_1 + \delta^2 w_2 + \dots , \\ p &= p_s + \delta p_1 + \delta^2 p_2 + \dots . \end{aligned} \quad (2.44)$$

These expansions are then substituted into the governing equations and boundary conditions, which are then separated into problems at each order of δ . The $O(1)$ problem is given by

$$\begin{aligned} \frac{\partial u_s}{\partial x} + \frac{\partial w_s}{\partial z} &= 0 , \\ \frac{\partial^2 u_s}{\partial z^2} + 3 &= 0 , \\ Re \frac{\partial p_s}{\partial z} + 3 \cot \beta &= 0 , \end{aligned} \quad (2.45)$$

with the bottom boundary conditions

$$u_s = w_s = 0 \quad \text{at } z = 0 , \quad (2.46)$$

and the free surface conditions

$$\left. \begin{aligned} p_s &= 0 \\ \frac{\partial u_s}{\partial z} &= 0 \end{aligned} \right\} \text{at } z = h . \quad (2.47)$$

This problem can be solved to find the solution

$$\begin{aligned}
u_s &= \frac{3}{2}z(2h - z) , \\
w_s &= -\frac{3}{2}\frac{\partial h}{\partial x}z^2 , \\
p_s &= 3\frac{\cot\beta}{Re}(h - z) ,
\end{aligned} \tag{2.48}$$

which gives the steady-state solution if h is constant. The kinematic condition at $O(1)$ then gives

$$\frac{\partial h}{\partial t} + 3h^2\frac{\partial h}{\partial x} = 0 \quad \text{at } z = 0 . \tag{2.49}$$

The $O(\delta)$ problem satisfies

$$\begin{aligned}
\frac{\partial u_1}{\partial x} + \frac{\partial w_1}{\partial z} &= 0 , \\
\frac{\partial^2 u_1}{\partial z^2} &= Re\frac{\partial p_s}{\partial x} + Re\left(\frac{\partial u_s}{\partial t} + u_s\frac{\partial u_s}{\partial x} + w_s\frac{\partial u_s}{\partial z}\right) , \\
Re\frac{\partial p_1}{\partial z} &= \frac{\partial^2 w_s}{\partial z^2} ,
\end{aligned} \tag{2.50}$$

together with the bottom boundary conditions

$$u_1 = w_1 = 0 \quad \text{at } z = 0 , \tag{2.51}$$

and the free surface conditions

$$\left. \begin{aligned}
p_1 &= \frac{2}{Re}\frac{\partial w_s}{\partial z} \\
\frac{\partial u_1}{\partial z} &= 0
\end{aligned} \right\} \quad \text{at } z = h . \tag{2.52}$$

This problem can be solved for u_1 and w_1 . Evaluating these at the free surface and using the $O(1)$ kinematic condition to eliminate the time derivative of h , these can then be substituted into the $O(\delta)$ kinematic condition to give the following $O(\delta)$ Benney equation:

$$\frac{\partial h}{\partial t} + \frac{\partial(h^3)}{\partial x} + \delta\left(\frac{6}{5}Re\frac{\partial}{\partial x}\left(h^6\frac{\partial h}{\partial x}\right) - \cot\beta\frac{\partial}{\partial x}\left(h^3\frac{\partial h}{\partial x}\right)\right) = 0 . \tag{2.53}$$

Performing a linear stability analysis on this equation gives the critical Reynolds number of the flow. The fluid height h is set equal to the steady state-solution plus a perturbation, given by

$$h = 1 + h_0e^{ik(x-ct)} . \tag{2.54}$$

Linearizing the Benney equation in the perturbation gives

$$-ikc + 3ik - \delta k^2 \left(\frac{6}{5} Re - \cot \beta \right) = 0 . \quad (2.55)$$

Solving for c and setting the imaginary part to zero gives the critical Reynolds number

$$Re_{crit}^{Ben} = \frac{5}{6} \cot \beta . \quad (2.56)$$

This result matches the result obtained from the Orr-Sommerfeld equation. This method is also simpler, and will be used instead of the Orr-Sommerfeld method when tackling the problem with bottom heating and porosity. The real part of c gives the propagation speed of the longest disturbances, which is $c = 3$; this also matches the Orr-Sommerfeld result.

Chapter 3

Models

Three models for flow over a wavy, inclined plane will be compared. These are the shallow water model (SWM), the integral-boundary-layer model (IBL), and the weighted residual model (WRM), which is a modified integral-boundary-layer model. In this chapter, the development of each model is described, steady-state solutions for each model with bottom topography are obtained, and the even bottom stability predictions are drawn for each model.

3.1 Shallow Water Model

The shallow-water model is the simplest model and is based on the shallow-water equations. It has empirical terms added to account for viscosity and bottom friction, and an empirical coefficient multiplying the advective terms. The added viscosity is in the form proposed by Gent [31] to ensure that the term is energetically consistent. The model has been investigated thoroughly by Balmforth and Mandre [5], who used it to study flow down a wavy inclined plane. Although the model is simple, it has serious limitations due to the empirical development; these limitations will be discussed later.

As suggested by the name, the shallow-water model is based on shallow-water theory and hence assumes that the fluid is incompressible and inviscid, and that the thickness of the fluid is much smaller than the characteristic length in the flow direction. It then follows that the pressure distribution is approximately hydrostatic and that the stream-wise velocity is depth independent. This model is limited to gentle inclines.

After these simplifications are made, three modifications are added to make the model more realistic. A flow factor multiplying the advective term is added; the value is empirically

determined, and depends on whether the flow is laminar or turbulent. For the laminar model, a value of $\frac{4}{5}$ is used [5]. A term partially accounting for viscosity and a bottom friction term are also added.

Two different forms of the shallow-water equations have been developed: one pertaining to laminar flow and the other to turbulent flow. The difference between the two is in the viscosity parameter of the added viscous term, the form of the bottom friction term, and the coefficient of the advection term. Balmforth and Mandre [5] give a thorough description of the two versions of the model. The laminar model is used in this study because flows having a Reynolds number of order unity are considered, and because the other two models to be developed assume laminar flow. The shallow-water model equations are

$$\frac{\partial h}{\partial t} + \frac{\partial(hu)}{\partial x} = 0, \quad (3.1)$$

$$\frac{\partial u}{\partial t} + \frac{4}{5}u\frac{\partial u}{\partial x} = g \cos \beta \left(\tan \beta - \frac{\partial h}{\partial x} - \zeta' \right) - \nu \frac{u}{h^2} + \frac{1}{h} \frac{\partial}{\partial x} \left(h\nu \frac{\partial u}{\partial x} \right) + \frac{\sigma}{\rho} \frac{\partial^3}{\partial x^3} (h + \zeta). \quad (3.2)$$

Non-dimensionalizing the equations using the same scaling as in section 2.1 and changing the variables to h and $q = uh$, the equations become

$$\frac{\partial h}{\partial t} + \frac{\partial q}{\partial x} = 0, \quad (3.3)$$

$$\begin{aligned} \frac{\partial q}{\partial t} + \frac{\partial}{\partial x} \left(\frac{4}{5} \frac{q^2}{h} + \frac{\cot \beta}{2Re} h^2 \right) &= -\frac{1}{5} \frac{q}{h} \frac{\partial q}{\partial x} - \frac{\cot \beta}{Re} h \zeta' \\ &+ \frac{1}{\delta Re} \left(h - \frac{q}{h^2} \right) + \delta^2 h We \frac{\partial^3}{\partial x^3} (\zeta + h) \\ &+ \frac{\delta}{Re} \left(\frac{\partial^2 q}{\partial x^2} - \frac{q}{h} \frac{\partial^2 h}{\partial x^2} - \frac{1}{h} \frac{\partial h}{\partial x} \frac{\partial q}{\partial x} + \frac{q}{h^2} \left(\frac{\partial h}{\partial x} \right)^2 \right). \end{aligned} \quad (3.4)$$

The non-dimensional flow variables are h , the height of the free surface from the bottom, and q , the volume flow rate.

3.2 Integral-Boundary-Layer Model

The integral-boundary-layer model is derived more rigorously from the Navier-Stokes equations. The second order non-dimensionalized continuity and momentum equations, from equations (2.23) to (2.25), are

$$\frac{\partial u}{\partial x} + \frac{\partial w}{\partial z} = 0 , \quad (3.5)$$

$$\delta Re \left(\frac{\partial u}{\partial t} + u \frac{\partial u}{\partial x} + w \frac{\partial u}{\partial z} \right) = -\delta Re \frac{\partial p}{\partial x} + 3 + \delta^2 \frac{\partial^2 u}{\partial x^2} + \frac{\partial^2 u}{\partial z^2} , \quad (3.6)$$

$$0 = -Re \frac{\partial p}{\partial z} - 3 \cot \beta + \delta \frac{\partial^2 w}{\partial z^2} . \quad (3.7)$$

Here, the advective term in the z -momentum equation is neglected because it will become third order in δ when the pressure is eliminated from the momentum equations. This model more accurately accounts for the fluid viscosity since most of the viscous terms from the Navier-Stokes equations are retained. It also accounts for a non-hydrostatic pressure distribution by including a viscosity term in the z -momentum equation, and it is valid for steeper inclines. These are improvements over the shallow-water model.

At the free surface, the dynamic and kinematic conditions are applied and are given in non-dimensional form by

$$\left. \begin{aligned} 0 &= p - \frac{2\delta}{Re} \frac{\partial w}{\partial z} + \delta^2 We \frac{\partial^2}{\partial x^2} (h + \zeta) \\ 0 &= \frac{\partial u}{\partial z} - 4\delta^2 \frac{\partial}{\partial x} (h + \zeta) \frac{\partial u}{\partial x} + \delta^2 \frac{\partial w}{\partial x} \end{aligned} \right\} \text{ at } z = h + \zeta , \quad (3.8)$$

$$w = \frac{\partial h}{\partial t} + u \frac{\partial (h + \zeta)}{\partial x} \left. \right\} \text{ at } z = h + \zeta . \quad (3.9)$$

As well, the following no-slip conditions are imposed at the bottom surface:

$$u = w = 0 \text{ at } z = \zeta . \quad (3.10)$$

The pressure can be eliminated by integrating the z -momentum equation and using the first condition in equation (3.8) to find an expression for the pressure, and then substituting this expression into the x -momentum equation. This leaves the continuity equation and a single momentum equation. The form of the streamwise velocity is then assumed based on the known steady flow over an even-bottom inclined plane. The profile, modified to account for bottom topography defined by $\zeta(x)$, is given by

$$u = \frac{3q(x,t)}{2h^3} (2(h + \zeta)z - z^2 - \zeta^2 - 2h\zeta) . \quad (3.11)$$

The z dependence is then eliminated from the momentum and continuity equations by integrating the equations across the fluid layer thickness and applying the boundary conditions. The final form of the integral-boundary-layer model equations are

$$\frac{\partial h}{\partial t} + \frac{\partial q}{\partial x} = 0 , \quad (3.12)$$

$$\begin{aligned} \frac{\partial q}{\partial t} + \frac{\partial}{\partial x} \left(\frac{6}{5} \frac{q^2}{h} + \frac{3}{2} \frac{\cot \beta}{Re} h^2 \right) &= \delta^2 h We \frac{\partial^3}{\partial x^3} (h + \zeta) - 3h \frac{\cot \beta}{Re} \zeta' + \frac{3}{\delta Re} \left(h - \frac{q}{h^2} \right) \\ &+ \frac{\delta}{Re} \left(\frac{9}{2} \frac{\partial^2 q}{\partial x^2} - \frac{6}{h} \frac{\partial h}{\partial x} \frac{\partial q}{\partial x} - \frac{3}{h} \frac{\partial q}{\partial x} \zeta' + 3 \frac{q}{h^2} \frac{\partial h}{\partial x} \zeta' \right) \\ &+ \frac{\delta}{Re} \left(6 \frac{q}{h^2} \left(\frac{\partial h}{\partial x} \right)^2 - 6 \frac{q}{h^2} (\zeta')^2 - 6 \frac{q}{h} \frac{\partial^2 h}{\partial x^2} - \frac{9}{2} \frac{q}{h} \zeta'' \right) . \end{aligned} \quad (3.13)$$

It should be noted that for both the integral-boundary-layer and weighted residual models, the flow rate q is defined by $q = \int_{\zeta}^{\zeta+h} u dz$.

3.3 Weighted Residual Model

The weighted residual model is derived following a similar procedure to that used for the integral-boundary layer model. However, before integrating in the cross-stream direction, the equations are multiplied by a weighting function; in this case, a parabolic profile is used as the weighting function. The parabolic profile is the shape of the velocity profile of the Nusselt solution for flow over an even-bottomed incline, which is the assumed shape of the velocity profile for the model. This was shown by Ruyer-Quil and Manneville [22] to be the optimal weighting function in that it allows the model to reproduce the known critical Reynolds number for the onset of instability for the even bottom case, and is therefore assumed to give more realistic predictions for related flows as well. In this way, a weighted average over the depth of the fluid is used. The resulting model equations are

$$\frac{\partial h}{\partial t} + \frac{\partial q}{\partial x} = 0 , \quad (3.14)$$

$$\begin{aligned} \frac{\partial q}{\partial t} + \frac{\partial}{\partial x} \left(\frac{9}{7} \frac{q^2}{h} + \frac{5}{4} \frac{\cot \beta}{Re} h^2 \right) &= \frac{5}{6} \delta^2 h We \frac{\partial^3}{\partial x^3} (h + \zeta) \\ &+ \frac{q}{7h} \frac{\partial q}{\partial x} - \frac{5h}{2} \frac{\cot \beta}{Re} \zeta' + \frac{5}{2\delta Re} \left(h - \frac{q}{h^2} \right) \\ &+ \frac{\delta}{Re} \left(\frac{9}{2} \frac{\partial^2 q}{\partial x^2} - \frac{9}{2h} \frac{\partial h}{\partial x} \frac{\partial q}{\partial x} - \frac{5}{2} \frac{q}{h^2} \frac{\partial h}{\partial x} \zeta' + 4 \frac{q}{h^2} \left(\frac{\partial h}{\partial x} \right)^2 \right) \\ &+ \frac{\delta}{Re} \left(-5 \frac{q}{h^2} (\zeta')^2 - 6 \frac{q}{h} \frac{\partial^2 h}{\partial x^2} - \frac{15}{4} \frac{q}{h} \zeta'' \right) . \end{aligned} \quad (3.15)$$

3.4 Steady State Solutions

Constant steady-state solutions to equation 3.16 for h and q , the flow variables of interest, can easily be found for the even bottom case. Choosing their values as the characteristic value by which the equations are scaled gives non-dimensional steady state solutions of $q_s = 1$ and $h_s = 1$.

The steady-state solutions for a flow over an incline with bottom topography are more complicated, and cannot be found exactly. However, solutions can be found numerically, or analytically using a perturbation series solution. In all cases, the steady-state continuity equation requires that q is constant, and the scaling is chosen so that $q = 1$. The momentum equation then gives a single ordinary differential equation for h . For the integral-boundary-layer model, for example, this differential equation is

$$\begin{aligned} \frac{6}{5} \frac{h'}{h^2} - 3 \frac{\cot \beta}{Re} h(h' + \zeta') + \delta^2 h We (h''' + \zeta''') + \frac{3}{\delta Re} \left(h - \frac{1}{h^2} \right) \\ + \frac{\delta}{Re} \left(\frac{3}{h^2} h' \zeta' + \frac{6}{h^2} ((h')^2 + (\zeta')^2) - \frac{6}{h} h'' - \frac{9}{2h} \zeta'' \right) = 0, \end{aligned} \quad (3.16)$$

and is solved subject to periodic boundary conditions applied at $x = 0$ and $x = 1$.

To find the perturbation series solution, h is expanded in powers of the shallowness parameter δ :

$$h = h_s + \delta h_1 + \delta^2 h_2 + \delta^3 h_3 + O(\delta^4). \quad (3.17)$$

By substituting this into equation (3.16) and separating into problems at each order of δ , h_1 , h_2 , and h_3 can be found; h_s is the steady-state solution for the even bottom case, so $h_s = 1$. The approximate analytical steady-state solution for the integral-boundary-layer model to $O(\delta^2)$ has been found to be

$$h = 1 + \delta \left(\frac{\cot \beta}{3} \zeta' \right) + \delta^2 \left(\frac{-2}{45} Re \cot \beta \zeta'' + \frac{\zeta''}{2} + \frac{2}{3} (\zeta')^2 + (\cot \beta)^2 \left(\frac{2}{9} (\zeta')^2 + \frac{\zeta''}{9} \right) \right) + O(\delta^3). \quad (3.18)$$

Two numerical methods are used to find the steady-state solution; the first employs a built-in Matlab routine. Using Matlab's `bvp4c` algorithm requires re-writing the model equations as a system of first order differential equations. For example, the third order equation, (3.16), for the the case of the integral-boundary-layer model, is written as a

system of three first order differential equations, which can be expressed as

$$\begin{aligned}
y_0(x) &= h(x) , \\
y_1(x) &= \frac{dh}{dx} , \\
y_2(x) &= \frac{dy_1}{dx} = \frac{d^2h}{dx^2} , \\
y_3(x) &= \frac{dy_2}{dx} = \frac{d^3h}{dx^3} \\
&= \frac{1}{\delta^2 We y_1^2} \left[\frac{-6}{5} \frac{y_2}{y_1} + 3 \frac{y_1^2}{Re} \cot \beta (y_1 + \zeta') - \frac{3}{\delta Re} \left(y_1^2 - \frac{1}{y_1} \right) \right. \\
&\quad \left. - \frac{\delta}{Re} \left(3 \zeta' \frac{y_2}{y_1} + 6 \frac{y_2^2}{y_1} - 6 \frac{(\zeta')^2}{y_1} - 6 y_3 - \frac{9}{2} \zeta'' \right) \right] - \zeta''' .
\end{aligned} \tag{3.19}$$

The `bvp4c` routine is then used to solve this system of equations. The routine is applicable to boundary value problems and it uses a collocation method to solve the system with fourth order accuracy. This method of finding the steady-state solution is simple to program in Matlab, and it is effective for many sets of flow parameters. However, for sufficiently small Weber number flows, difficulty in finding a steady-state solution can be encountered as a result of a small quantity, $\delta^2 We$, multiplying the highest derivative in equation (3.16). For these flows, Newton's method is used to find a numerical solution for the weighted residual and integral-boundary-layer models. This method involves an iterative approach to solving the differential equation for h .

Using the Newton's method involves discretizing equation (3.16) using the central differencing scheme on a grid of N points spanning $x = 0$ to $x = 1$. All terms are moved to the same side of the equation and set equal to zero. A vector \vec{F} is defined with components f_i equal to the discretized momentum equation about point i . For example, f_i for the integral-boundary-layer model is

$$\begin{aligned}
f_i &= -2\delta^2 We \frac{h_i^3}{\Delta x} (h_{i+2} - 2h_{i+1} + 2h_{i-1} - h_{i-2}) + 24 \frac{\delta}{Re} h_i (h_{i+1} + h_i - 1 - 2h_i) \\
&\quad - \frac{\delta}{Re} (h_{i+1} - h_{i-1})^2 + \Delta x \left(6 \frac{\cot \beta}{Re} h_i^3 - 6 \frac{\delta}{Re} \zeta'_i - \frac{12}{5} \right) (h_{i+1} - h_{i-1}) + 18 \Delta x^2 \frac{\delta}{Re} \zeta''_i h_i \\
&\quad - 4 \Delta x^2 h_i^3 \left[\frac{3}{\delta Re} - \frac{\cot \beta}{Re} \zeta'_i + \delta^2 We \zeta'''_i \right] + 12 \Delta x^2 \frac{\cot \beta}{Re} + 24 \Delta x^2 \frac{\delta}{Re} (\zeta'_i)^2 ,
\end{aligned} \tag{3.20}$$

where Δx is the uniform grid spacing.

The Jacobian matrix \mathbf{J} is defined such that $J_{i,j} = \frac{\partial f_i}{\partial h_j}$. An initial guess for \vec{h} , which gives the fluid layer thickness at each grid point along one bottom wavelength, is provided using the even bottom steady-state solution. The wavy bottom steady-state solution is then calculated iteratively using the formula

$$\vec{h}_{n+1} = \vec{h}_n + \mathbf{J}^{-1}(-\vec{F}_n) . \quad (3.21)$$

Next, example steady-state solutions are presented for selected sets of parameters to illustrate the dependence on the parameters, and also to show how the numerical solutions compare with the perturbation expansion solutions. Figure 3.1 shows the numerical steady-state solutions for all three models for the parameters $Re = 1$, $\delta = 0.1$, $\cot \beta = 1$, and $\tilde{We} = 5$. The bottom topography is taken to be sinusoidal, and is expressed in non-dimensional form as

$$\zeta = a_b \cos(2\pi x) \text{ where } a_b = \frac{A_b}{H} , \quad (3.22)$$

with $a_b = 0.1$ denoting the dimensionless bottom amplitude. The bottom wavelength has been scaled to be unity. The top panel shows that the IBL model and the WRM steady-state solutions match very closely, with the curves for the fluid thickness, h , almost overlapping. For the SWM, however, the numerical and analytical solutions differ more due to the weight of each term in the steady-state equation; the leading order term compared to the $O(\delta)$ term is smaller in the SWM equation than in the other models, so the higher order terms are more important. The effect of truncating the analytical solution is therefore more significant for the SWM. The lower three panels of the figure show that the approximate analytical solutions match the numerical solutions very closely for this set of parameters, particularly for the integral-boundary-layer and weighted residual models.

Figure 3.2 shows, for the weighted residual model, how the approximate analytical solutions match the numerical solutions when the parameters are changed. The top panel shows the basic case again; the middle panel shows the solutions for the same parameters, except with $\tilde{We} = 75$, and the bottom panel shows the basic case but with $\cot \beta = 5$. Since both \tilde{We} and $\cot \beta$ were assumed to be $O(1)$ in the perturbation expansion solution, changing the order of magnitude of these, or other parameters, causes noticeable discrepancies between the numerical and approximate analytical solutions.

In figure 3.3, numerical solutions are shown for the basic case with small parameters, and for cases with a single parameter increased from the basic case. The top panel shows the basic set of parameters for comparison. The second panel shows the effect of increasing the bottom amplitude, which increases the variation in fluid layer thickness, and also increases the variation in the height of the fluid interface. This is expected because the even bottom solution has a constant fluid layer thickness and interface height, and adding bottom

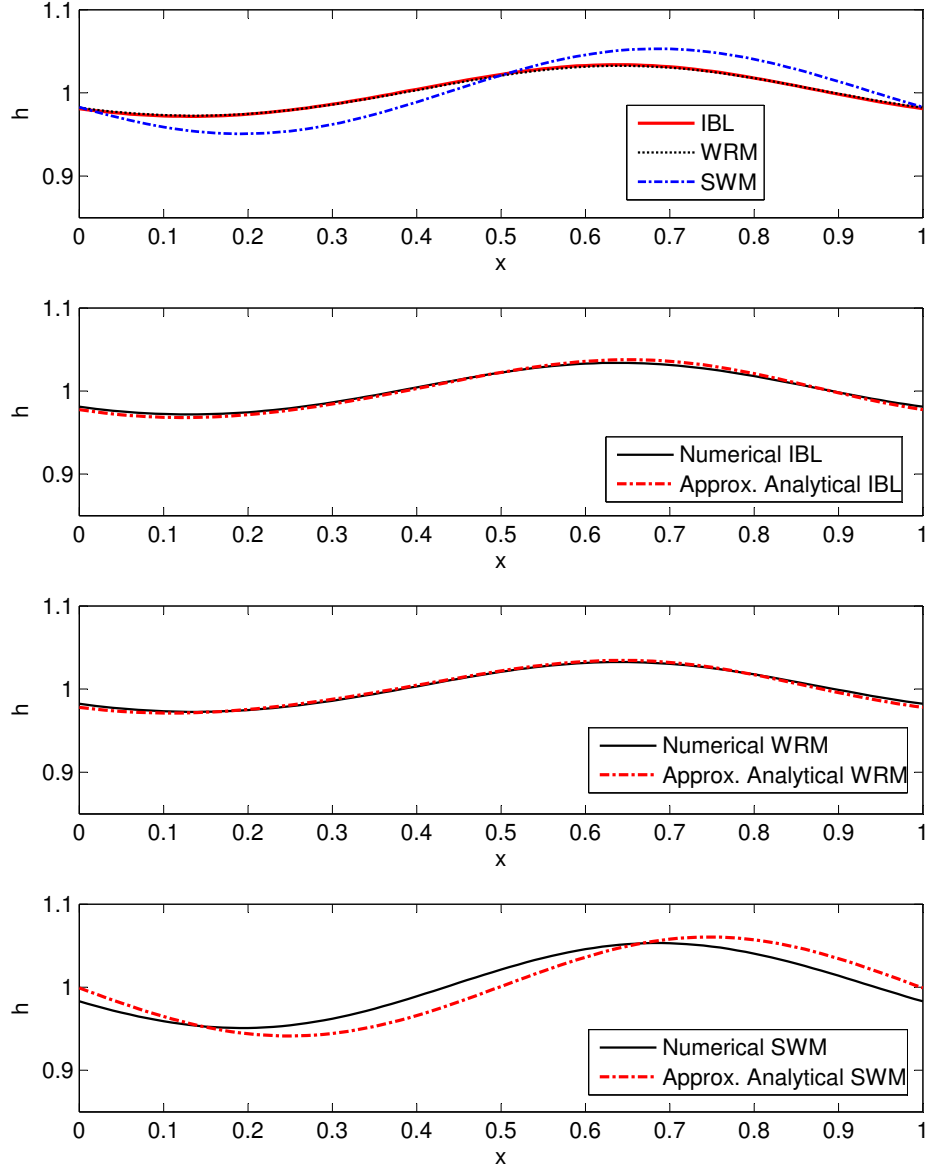


Figure 3.1: Numerical steady-state solutions for each model (top) for $Re = 1$, $\delta = 0.1$, $\cot \beta = 1$, $We = 5$, and $a_b = 0.1$, and numerical solutions for each model compared to the corresponding approximate analytical solution.

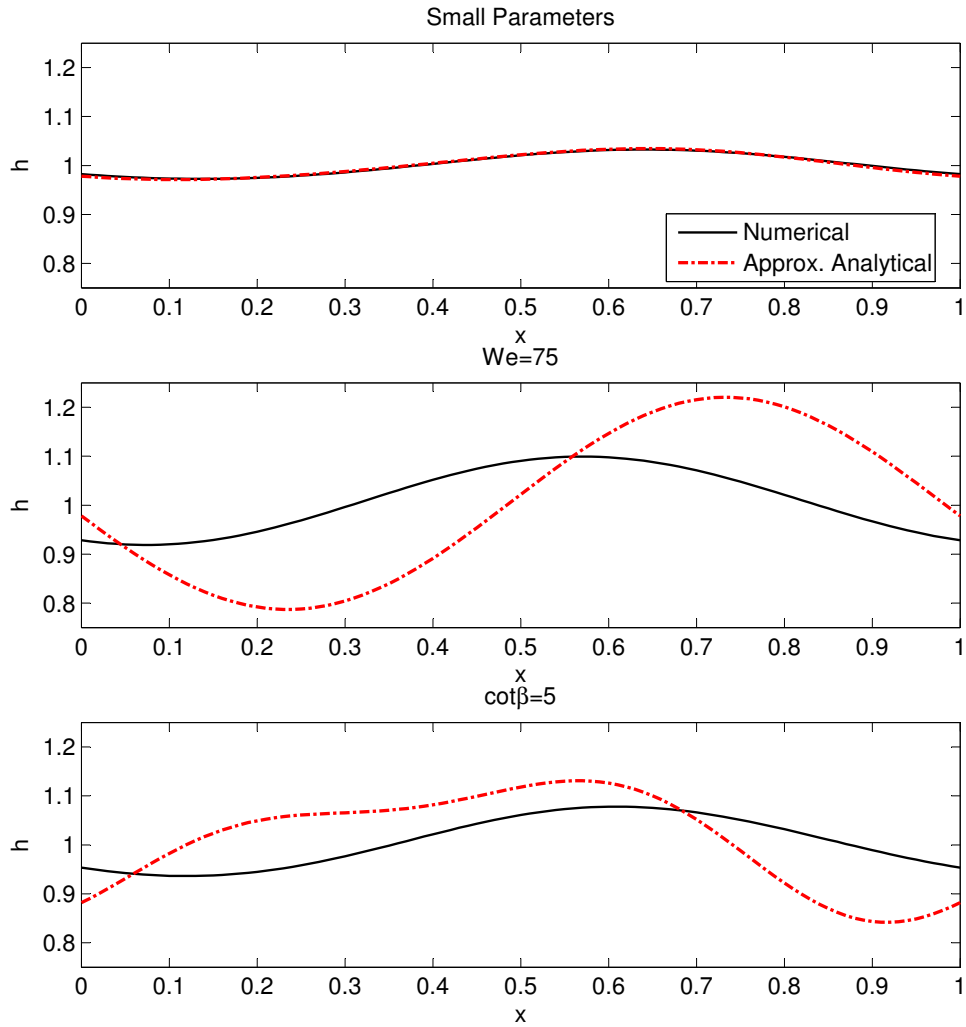


Figure 3.2: Numerical steady state-solutions compared with the approximate analytical solutions for $Re = 1$, $\delta = 0.1$, $\cot \beta = 1$, $We = 5$, and $a_b = 0.1$, top, and when one of the parameters is changed.

topography introduces variations, so increasing the bottom amplitude should increase the variations of fluid layer thickness and interface height. In the third panel, the effect of decreasing the angle of inclination is shown; the fluid thickness varies more than in the basic case, but the location where the fluid layer is thickest shifts slightly such that the free surface location is very similar to the basic case. This can be explained physically by considering how the steady-state solution would develop; the fluid would build up in the troughs of the bottom topography because, due to the small angle on inclination, it would not have the momentum to overcome the bottom surface peaks. This accounts for the greater variation in fluid layer thickness, as well as the location of the maximum fluid layer thickness, which explains the relatively even free surface. In the fourth panel, the Reynolds number is increased, and the effect is similar to that of the decreased angle of inclination.

In the fifth panel of figure 3.3, the Weber number is increased, and in the last panel, the shallowness parameter is increased; both of these changes have a similar effect, which is to drastically increase the variation in fluid layer thickness, as well as to shift the location of the maximum fluid layer thickness. The location of the maximum fluid layer thickness is shifted toward the lowest point of the bottom surface, resulting in a relatively flat free surface. An increased Weber number represents greater surface tension, which tends to flatten the interface. A larger δ indicates that the fluid layer thickness is larger compared to the wavelength of the bottom topography, resulting in a relatively even free surface because the interface is farther from the bottom surface and therefore less influenced by it.

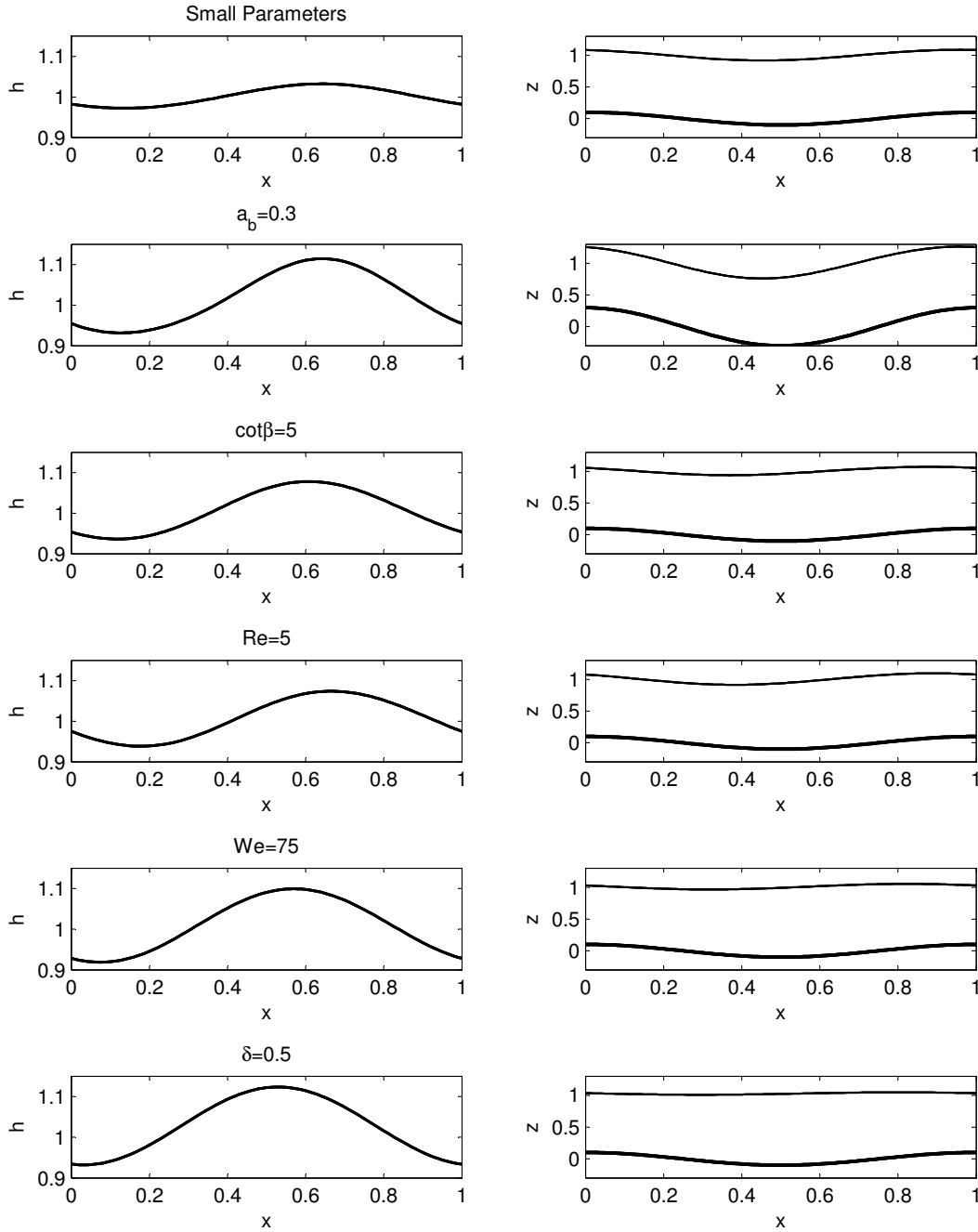


Figure 3.3: Numerical steady-state solutions for the weighted residual model for $Re = 1$, $\delta = 0.1$, $\cot \beta = 1$, $We = 5$, and $a_b = 0.1$ (top), and numerical solutions showing the effect of increasing one of the parameters. The left column shows the fluid layer thickness and the right column shows the interface location and the bottom topography.

3.5 Model Stability

Each of the three models can be used to predict the stability of the flow. As a first approach, the even bottom case is considered, so ζ in the model equations is set to zero. A linear stability analysis is then performed on the model equations where each of the variables is perturbed about the steady-state value:

$$h = h_s + \hat{h} = 1 + h_0 e^{ik(x-ct)}, \quad (3.23)$$

$$q = q_s + \hat{q} = 1 + q_0 e^{ik(x-ct)}. \quad (3.24)$$

Substituting these into the model equations and linearizing in the perturbation gives two equations in terms of h_0 , q_0 , c , k , and the flow parameters. With the weighted residual model, for example, the equations are

$$q_0 = ch_0, \quad (3.25)$$

$$-cq_0 + \frac{9}{7}(2q_0 - h_0) = \frac{q_0}{7} - \frac{5i}{2\delta k Re}(3h_0 - q_0) - \frac{5}{2} \frac{\cot \beta}{Re} h_0 + \frac{5}{6} \delta^2 We (ik)^2 h_0 + \frac{\delta}{Re} ik \left(\frac{9}{2} q_0 - 6h_0 \right). \quad (3.26)$$

These two equations can be combined to give the dispersion equation:

$$c^2 - c \left(\frac{17}{7} - \frac{i}{2Re} \left[\frac{5}{\delta k} + 9\delta k \right] \right) + \left(\frac{9}{7} - \frac{5}{2} \frac{\cot \beta}{Re} - \frac{5}{6} We (\delta k)^2 - \frac{3i}{Re} \left[\frac{5}{2\delta k} + 2\delta k \right] \right) = 0. \quad (3.27)$$

Solving for the imaginary part of c and setting it equal to zero gives the neutral stability curve, which, for the weighted residual model is,

$$Re_{cr}^{WRM} = 10 \cdot \cot \beta \cdot \left(\frac{\left(\frac{125}{7\delta k} + \frac{15}{7} \cdot \delta k \right)^2}{\left(\frac{5}{\delta k} + 9\delta k \right)^2} - \frac{37}{49} - \frac{10}{3} \cdot We (\delta k)^2 \right)^{-1}. \quad (3.28)$$

Repeating this to calculate the neutral stability curve for the integral-boundary-layer model gives

$$Re_{cr}^{IBL} = 75 \cdot \cot \beta \cdot \left(\frac{\left(\frac{9}{\delta k} + \delta k \right)^2}{\left(\frac{1}{\delta k} + \frac{3}{2} \delta k \right)^2} - 6 - 25 \cdot We (\delta k)^2 \right)^{-1}, \quad (3.29)$$

and for the shallow water model,

$$Re_{cr}^{SWM} = 16 \cdot \cot \beta \cdot \left(\frac{\left(\frac{42}{5\delta k} + \frac{2}{5} \delta k \right)^2}{\left(\frac{1}{\delta k} + \delta k \right)^2} - \frac{4}{25} - 16 \cdot We (\delta k)^2 \right)^{-1} \quad (3.30)$$

is obtained.

The critical Reynolds number for the even bottom case can then be found for each model by allowing the wavenumber, k , to go to zero, giving

$$\begin{aligned}
 Re_{crit}^{WRM} &= \frac{5}{6} \cot \beta , \\
 Re_{crit}^{IBL} &= \cot \beta , \\
 Re_{crit}^{SWM} &= \frac{5}{22} \cot \beta .
 \end{aligned}
 \tag{3.31}$$

Only the weighted residual model results matches the theoretical result, given in equation (2.56). These predicted critical Reynolds numbers will be discussed further in chapter 5.

Chapter 4

Numerical Solutions

The model equations, unlike the Benney equation, are valid for both stable and unstable flows, and can therefore be solved numerically to find how the interface develops in time. In cases where the flow is expected to be stable based on the linear stability analysis, imposed perturbations should diminish, and the flow should recover to the steady state solution. In flows that are unstable, however, perturbations grow into waves, which interact and combine to form solitary waves, or roll waves. These roll waves eventually reach a stable form, as shown by Balmforth and Mandre [5], and they simply move along the incline without changing shape. To find the fully developed shape of the interface, the fractional step method is used to solve the model equations, following D'Alessio et al. [3].

The full Navier-Stokes equations can be solved for this problem using CFX, which is a commercial CFD software package. This avoids making the same assumptions used to develop the model equations, such as the assumed velocity profile and the truncation of the equations to $O(\delta^2)$; however, other approximations are made by modelling the flow with CFX, as discussed in section 4.2. Setting up equivalent problems using the model equations and CFX, the results can be compared to determine how well the model equations represent the unstable flow.

The numerical method used to solve the model equations, the numerical methods used in CFX, and the problem setup required for the CFX simulations are discussed in this chapter.

4.1 Numerical Solutions of Model Equations

The two equations for each model involve the two unknowns $h(x, t)$, the fluid layer thickness, and $q(x, t)$, the volume flow rate. Unlike the Benney equation, these model equations are valid beyond the onset of instability, and can therefore be used to predict the evolution of the free surface after the flow destabilizes. In this way, the number and shape of roll waves that will develop in a given flow can be predicted. The interface development as predicted by the three models can therefore be computed.

The model equations are solved numerically using the fractional step method [32], as outlined in D'Alessio et al. [3]. In this method, the model equations are rearranged into flux form, separating the advective and diffusive terms, and solved in two steps. For example, the IBL model equations are written as

$$\frac{\partial h}{\partial t} + \frac{\partial q}{\partial x} = 0, \quad (4.1)$$

and

$$\begin{aligned} \frac{\partial q}{\partial t} + \frac{\partial}{\partial x} \left(\frac{6}{5} \frac{q^2}{h} + \frac{3}{2} \frac{\cot \beta}{Re} h^2 \right) &= \delta^2 h We \frac{\partial^3}{\partial x^3} (h + \zeta) - 3h \frac{\cot \beta}{Re} \zeta' + \frac{3}{\delta Re} \left(h - \frac{q}{h^2} \right) \\ &+ \frac{\delta}{Re} \left(\frac{9}{2} \frac{\partial^2 q}{\partial x^2} - \frac{6}{h} \frac{\partial h}{\partial x} \frac{\partial q}{\partial x} - \frac{3}{h} \frac{\partial q}{\partial x} \zeta' + 3 \frac{q}{h^2} \frac{\partial h}{\partial x} \zeta' \right) \\ &+ \frac{\delta}{Re} \left(6 \frac{q}{h^2} \left[\left(\frac{\partial h}{\partial x} \right)^2 - (\zeta')^2 \right] - 6 \frac{q}{h} \frac{\partial^2 h}{\partial x^2} - \frac{9}{2} \frac{q}{h} \zeta'' \right) \\ &= \Psi. \end{aligned} \quad (4.2)$$

They are then solved in two steps. In the first step, a system of equations involving only the advective terms is solved:

$$\frac{\partial h}{\partial t} + \frac{\partial q}{\partial x} = 0, \quad (4.3)$$

and

$$\frac{\partial q}{\partial t} + \frac{\partial}{\partial x} \left(\frac{6}{5} \frac{q^2}{h} + \frac{3}{2} \frac{\cot \beta}{Re} h^2 \right) = 0. \quad (4.4)$$

This system of hyperbolic conservation laws can also be written as

$$\frac{\partial \vec{U}}{\partial t} + \frac{\partial F(\vec{U})}{\partial x} = 0, \quad (4.5)$$

where

$$\vec{U} = \begin{bmatrix} h \\ q \end{bmatrix}, \quad (4.6)$$

and

$$F(\vec{U}) = \left[\frac{6}{5} \frac{q^2}{h} + \frac{3}{2} h^2 \frac{\cot \beta}{Re} \right] . \quad (4.7)$$

The system is solved using MacCormack's explicit predictor-corrector scheme; in the predictor step, a forward differencing scheme is used, and a backward differencing scheme is used in the corrector step [33, 34]. The method can be expressed as

$$\vec{U}_j^* = \vec{U}_j^n - \frac{\Delta t}{\Delta x} \left[F(\vec{U}_{j+1}^n) - F(\vec{U}_j^n) \right] , \quad (4.8)$$

and

$$\vec{U}_j^{n+1} = \frac{1}{2} \left(\vec{U}_j^n + \vec{U}_j^* \right) - \frac{\Delta t}{2\Delta x} \left[F(\vec{U}_j^*) - F(\vec{U}_{j-1}^*) \right] , \quad (4.9)$$

where \vec{U}_j^n is \vec{U} at grid point j at time step n , and Δt is the time step and Δx is the uniform grid spacing.

In the second step, the diffusive terms are considered. For the integral-boundary-layer model, the equation

$$\frac{\partial q}{\partial t} = \Psi , \quad (4.10)$$

is discretized using the Crank-Nicolson scheme and solved iteratively. This method of solving the model equations is second order accurate in x and first order accurate in t .

This method determines the fluid thickness and volume flow rate at each time step, showing how the fluid interface develops with time. For a flow with a super-critical Reynolds number, the numerical perturbations can be enough to destabilize the flow; the perturbations grow into waves, which interact and eventually form a stable wave pattern. This wave pattern circles through the domain due to the periodic boundary conditions applied at the ends.

The volume flow rate and interface location for a particular flow setup are shown for the integral-boundary-layer and weighted residual models in the following figures. The initial conditions used are the steady state solution for h for the corresponding model, found using Matlab's `bvp4c` algorithm as described in chapter 3, and the steady-state solution plus a perturbation for q , the volume flow rate. A perturbation is added to q to cause the flow to destabilize faster and allow the flow to reach the final form of the interface more quickly. For stable flows, the perturbation will die down, and the steady-state solution

will be achieved. Periodic boundary conditions are imposed at the ends of the domain so that the flow circulates through it; when roll waves develop, they too circulate through the domain.

Figure 4.1 shows a flow modelled using the weighted residual model, with $Re = 2.28$, $a_b = 0.1$, $\delta = 0.1$, $\cot \beta = 1.5$, and with no surface tension, so $We = 0$. In the top panel, the volume flow rate, calculated using the weighted residual model, is shown for various times, illustrating how the free surface develops. The second, third, and fourth panels show the final volume flow rate, fluid thickness, and bottom surface and free surface of the flow, respectively. For the same case, simulation results using the integral-boundary-layer model equations are shown in figure 4.2. The interface development is noticeably different, although the final configuration is quite similar.

A case with the same parameters but with surface tension included through $We = 20.04$ is shown in figure 4.3, using the weighted residual model, and in figure 4.4, using the integral-boundary-layer model. A notable difference between these plots and those without surface tension is in the shape of the volume flow rate profile; the peaks, representing roll waves in the flow, are very sharp without surface tension and they are much smoother when surface tension is added. They are also shorter and wider when surface tension is added.

Simulation results for the shallow water model are not included because the shallow water model is meant for gentle inclines, whereas the integral-boundary-layer and weighted residual models are developed assuming $\cot \beta = O(1)$, which gives an incline that is steeper than appropriate for the shallow water model. Furthermore, the disparity between the critical Reynolds number of the shallow water model and that of the other two models makes finding an appropriate simulation in which all models are unstable difficult. Finally, as will be discussed in chapter 5, the shallow water model can be excluded as an accurate model based on its performance in predicting the critical Reynolds number and the neutral stability curve of the flow.

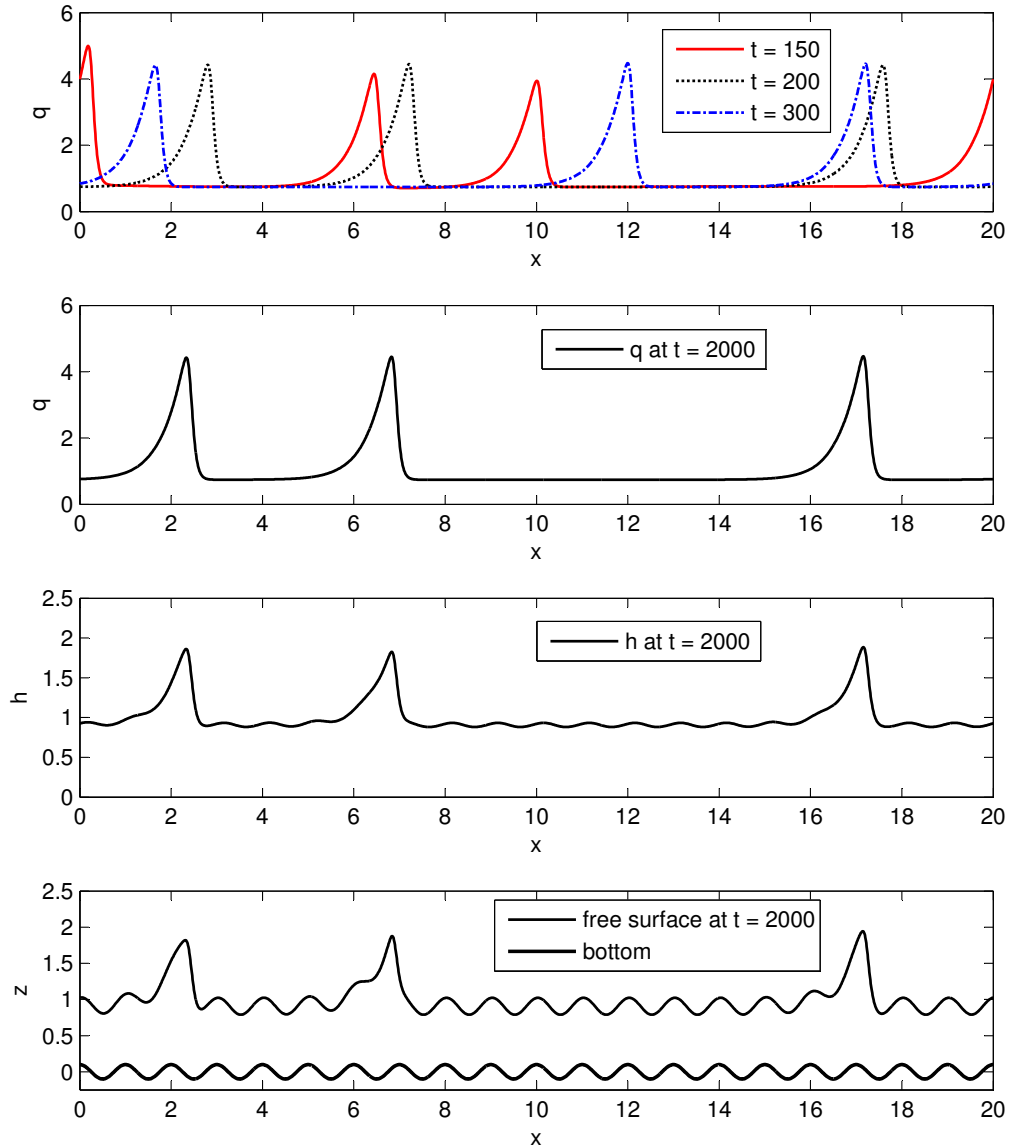


Figure 4.1: Volume flow rate distribution for a case without surface tension, simulated using the weighted residual model, at various times (top), and final volume flow rate, (second from top), fluid thickness (third from top), and bottom and free surface (bottom), shown fully developed. The flow parameters are $Re = 2.28$, $a_b = 0.1$, $\delta = 0.1$, $\cot \beta = 1.5$, and $We = 0$.

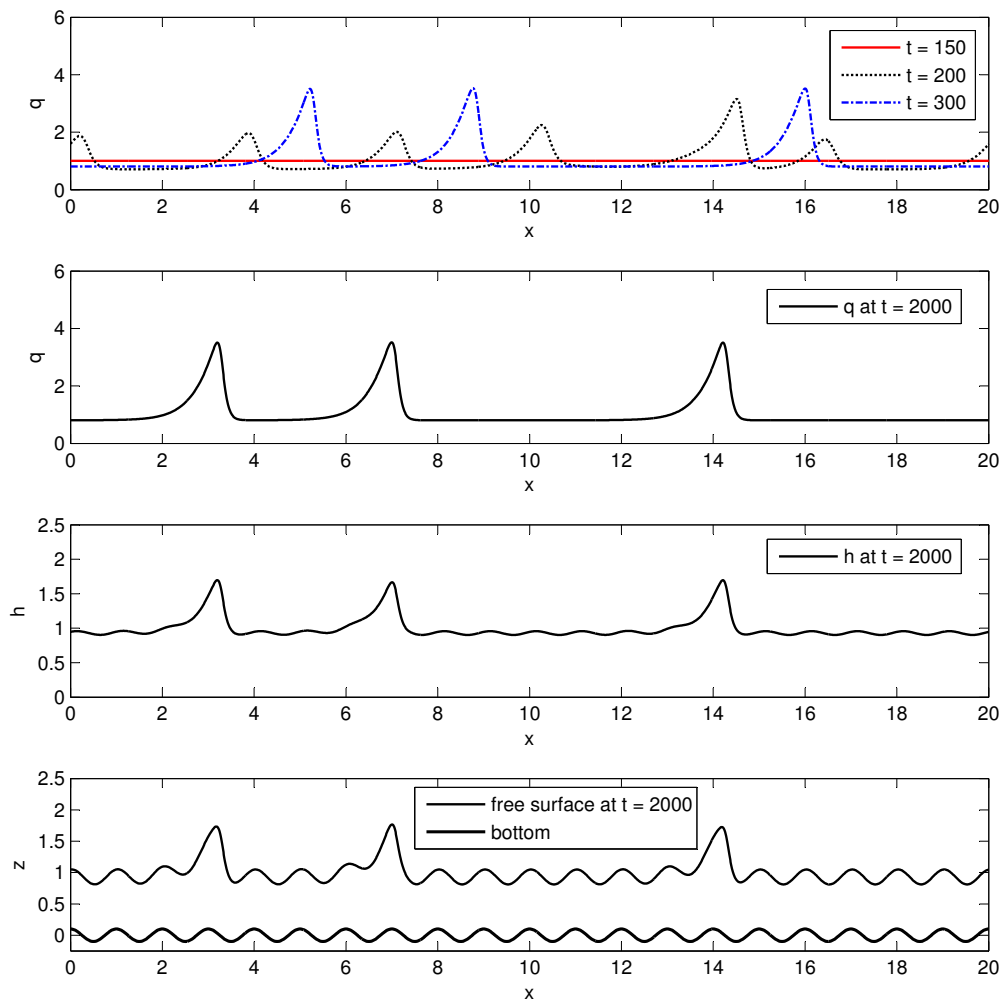


Figure 4.2: Volume flow rate distribution for a case without surface tension, simulated using the integral-boundary-layer model, at various times (top), and final volume flow rate, (second from top), fluid thickness (third from top), and bottom and free surface (bottom), shown fully developed. The flow parameters are $Re = 2.28$, $a_b = 0.1$, $\delta = 0.1$, $\cot \beta = 1.5$, and $We = 0$.

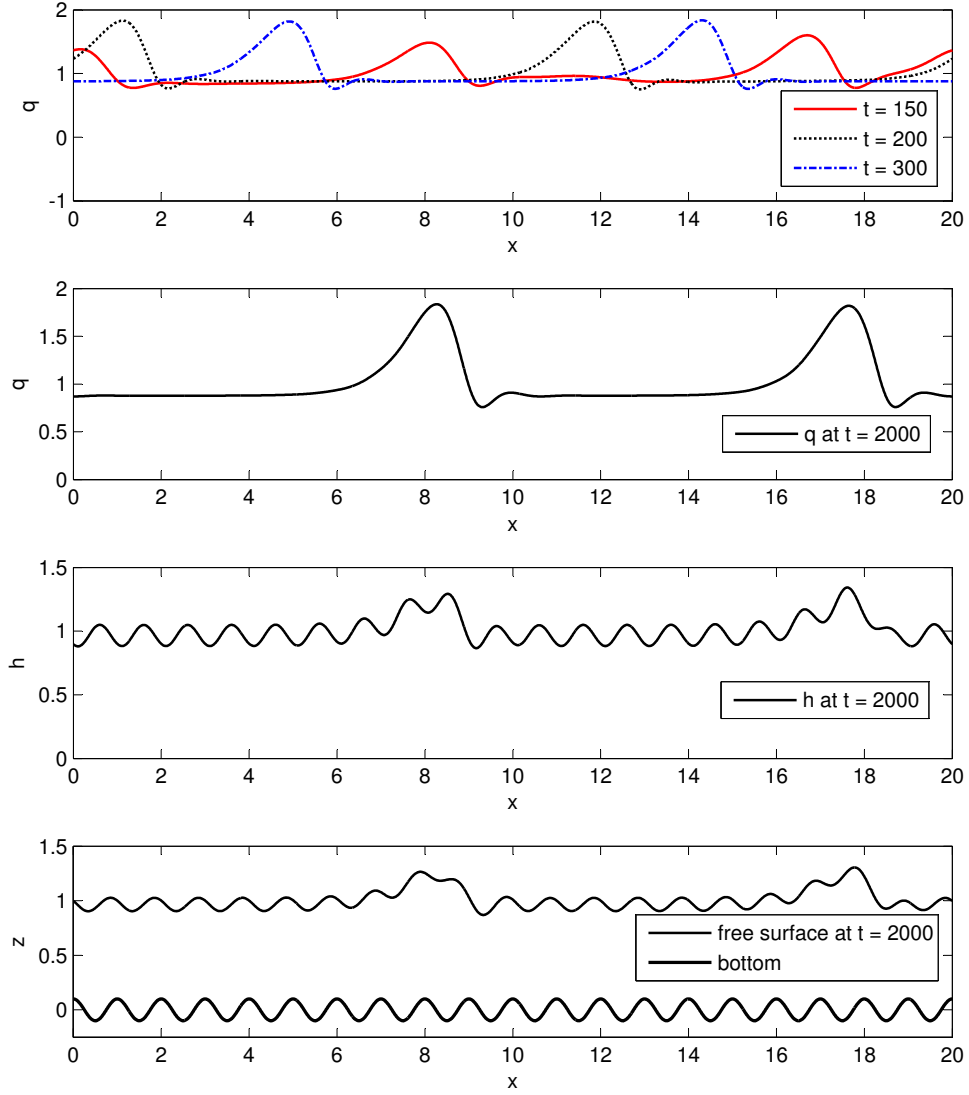


Figure 4.3: Volume flow rate distribution for a case with surface tension, simulated using the weighted residual model, for various times (top), and final volume flow rate, (second from top), fluid thickness (third from top), and bottom and free surface (bottom), shown fully developed. The flow parameters are $Re = 2.28$, $a_b = 0.1$, $\delta = 0.1$, $\cot \beta = 1.5$, and $We = 20.04$.

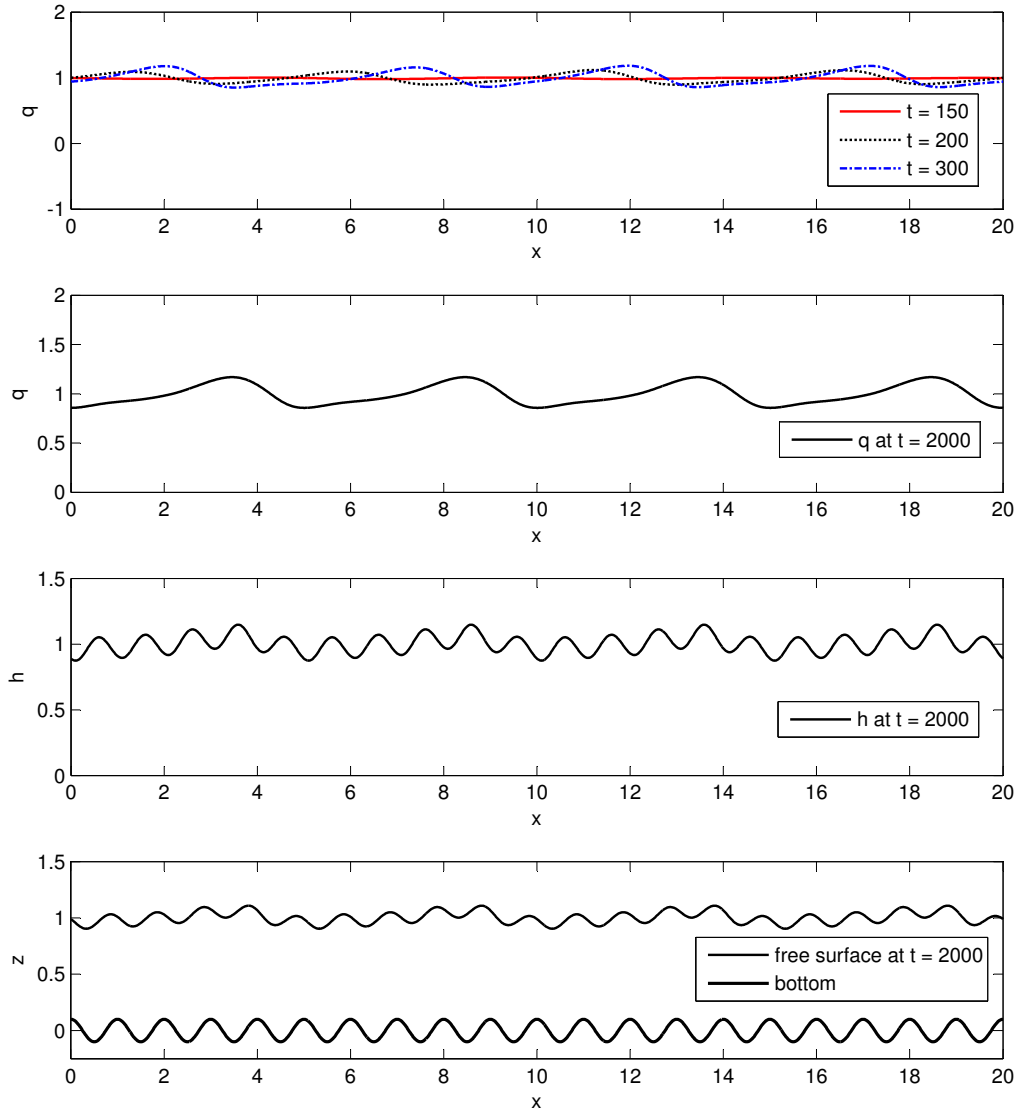


Figure 4.4: Volume flow rate distribution for a case with surface tension, simulated using the integral-boundary-layer model, for various times (top), and final volume flow rate, (second from top), fluid thickness (third from top), and bottom and free surface (bottom), shown fully developed. The flow parameters are $Re = 2.28$, $a_b = 0.1$, $\delta = 0.1$, $\cot \beta = 1.5$, and $We = 20.04$.

4.2 Numerical Solutions of the Full Navier-Stokes Equations

The full Navier-Stokes equations for the free surface flow down an inclined plane have also been solved by employing the CFD software package CFX. The numerical method used by CFX to solve the governing equations is a combination of the finite volume and finite element methods [35]. The domain is discretized into fluid elements, and control volumes are formed around element nodes. Momentum and mass are conserved over each control volume [35]. Solution variables and fluid properties are stored at the nodes, which are located within each control volume. The finite element method, using shape functions, is employed to calculate properties within fluid elements at the edges of the control volumes [35]. The High Resolution advection discretization scheme is used, which is a bounded second-order upwind scheme. It is bounded through the use of the flux-limiting methods of Barth and Jespersen [35]. A second-order backward Euler transient discretization scheme is used.

To locate the free surface, a volume-of-fluid method is used [36]. The volume fraction of one of the fluids is tracked as a solution variable using a volume fraction advection scheme [36]. This causes a smearing of the interface due to numerical diffusion and the possibility of multiple adjacent cells containing a volume fraction between zero and one; however, CFX uses a compressive scheme to minimize this diffusion [36]. Despite this, the interface is smeared over several mesh elements, rather than located at a discrete point. The interface location in this study is chosen as the contour along which the volume fractions of water and air are each 0.5. Additionally, a homogeneous multiphase model is used for the simulation, meaning a single flow field is calculated and shared by both fluids; this is an appropriate model for free-surface flows.

Surface tension is applied using the method described by Brackbill et al. [37]. A body force that is proportional to the volume fraction gradient is applied, so that the force is strong where the volume fraction of fluid is changing rapidly, which is near the surface. The surface tension body force is zero where the volume fraction is constant, away from an interface.

The setup and results for one particular case are shown here. The case has the following non-dimensional parameters: $Re = 2.28$, $\cot \beta = 1.5$, $We = 0$, $\delta = 0.1$, and $a_b = 0.1$; these are the same parameter values used in the simulations for which results are shown in figures 4.1 and 4.2. Physically, the setup involves a 0.1 mm thick layer of fluid flowing over a plane angled at 33.7° with bottom undulations of amplitude 0.01 mm and bottom wavelength 1 mm. The domain includes twenty bottom wavelengths with periodic boundary conditions

at both ends. A no-slip condition is enforced on the bottom surface, and atmospheric pressure is imposed at the top of the domain, with air allowed to enter or exit as required by the flow field. The properties of water are used, although surface tension is neglected. Due to the neglect of surface tension and evaporation, this case does not correspond to a physical situation, but was modified to obtain the desired non-dimensional parameters.

A two-dimensional simulation is conducted by creating a domain one element thick and enforcing symmetric boundary conditions on the sides. The domain is divided into 97926 hexahedral and wedge elements; an unstructured grid is used to conform the mesh to the waviness of the bottom topography. A section of the mesh showing one end and a little more than two bottom wavelengths is shown in figure 4.5.

The simulation is initialized using the steady-state fluid thickness calculated with the weighted residual model and the velocity profile assumed in the model. The initial pressure is hydrostatic. A time step of $\Delta t = 0.0005$ s is used.

The computational time required to solve this problem is significant; this particular case was solved on a single processor in approximately forty days. The same problem was solved on a much coarser grid in only five days; although the results match, the resolution is very poor. When surface tension is added, the computing time increases. A simulation identical to the one described above, but with surface tension added through a Weber number of about five, required over fifty days to complete. Finally, a simulation run in parallel on two processors and with a domain length of only ten bottom wavelengths completed in only about six days.

Figure 4.6 shows the non-dimensionalized volume flow rate and fluid interface after the flow has destabilized and developed roll waves. A volume fraction contour plot of a section of the domain is shown in figure 4.7, where one of the roll waves is visible. The smeared interface is also visible in this figure.

Finally, figure 4.8 shows the velocity profile at a vertical section of the flow compared to the profile assumed in the model development for two locations along the flow: one at the peak of a wave and the other away from any peaks. These locations are chosen because they represent the velocity profiles at the locations of minimum and maximum average velocity along the domain. The shape of the profile is the same at the two locations; the velocity profile within the wave but away from the peak would have the same shape and a magnitude between the two shown in the figure. The plot shows that the velocity profile predicted by CFX is very similar to the assumed profile; however there is a slight velocity

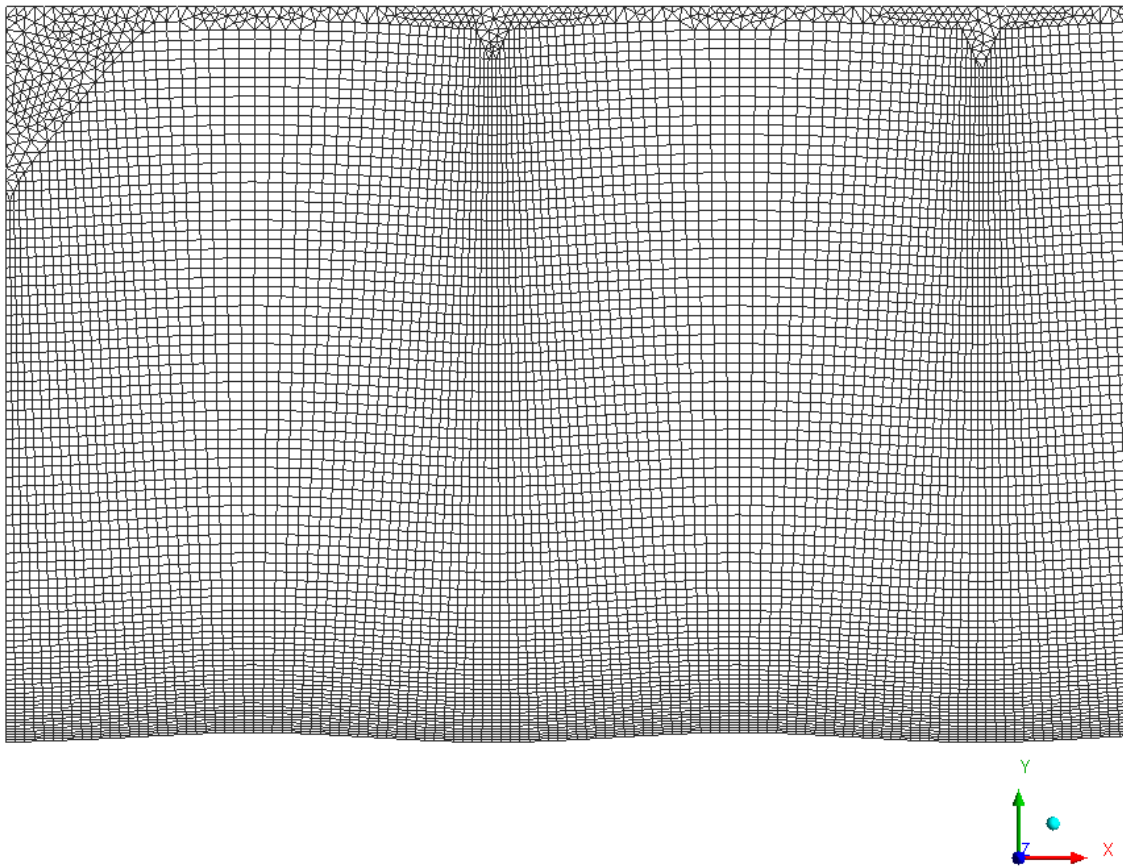


Figure 4.5: A section of the mesh used for a CFX simulation of flow down an inclined plane.

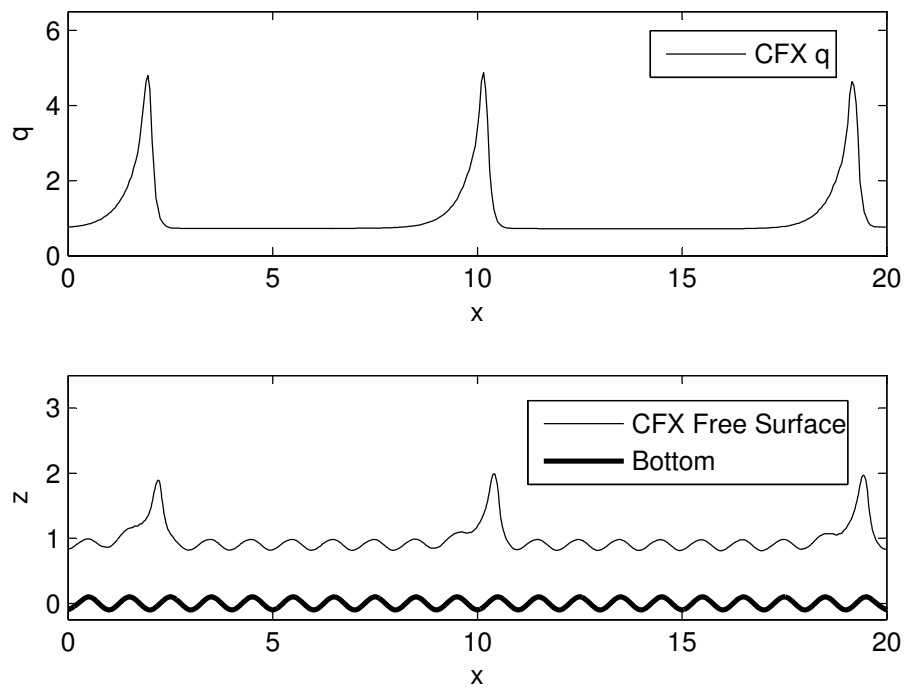


Figure 4.6: Volume flow rate (top) and fluid interface and bottom surface (bottom) of fully developed flow. The flow parameters are $Re = 2.28$, $a_b = 0.1$, $\delta = 0.1$, $\cot \beta = 1.5$, and $We = 0$.

Water . Volume Fraction
(Water Volume Fraction Contour)

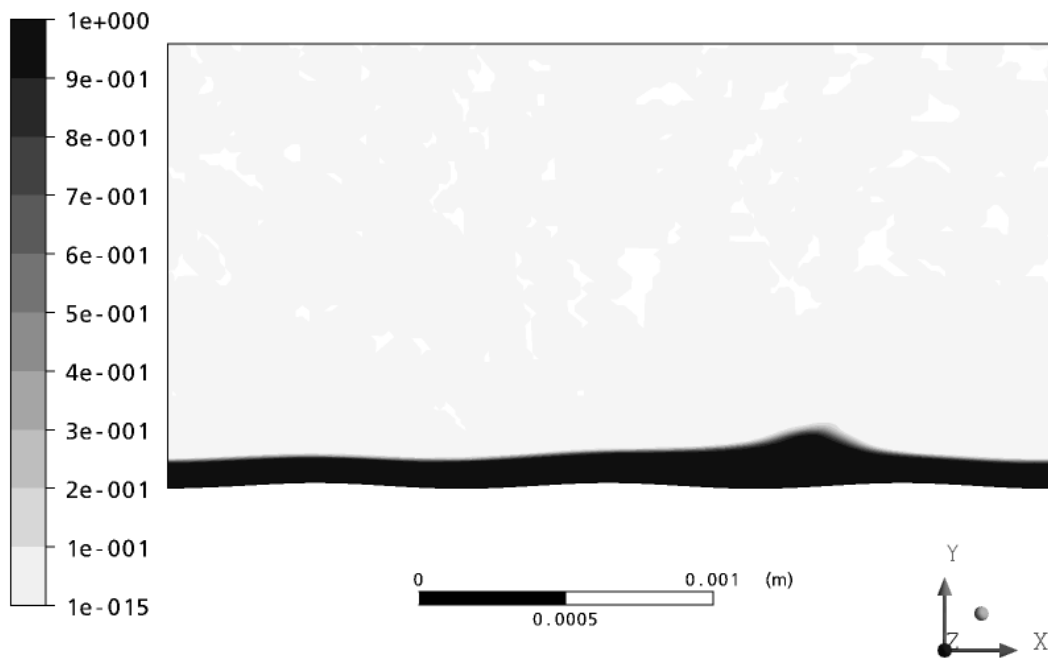


Figure 4.7: Volume fraction contour plot of a section of the domain for the fully developed flow, showing one roll wave. The flow parameters are $Re = 2.28$, $a_b = 0.1$, $\delta = 0.1$, $\cot \beta = 1.5$, and $We = 0$.

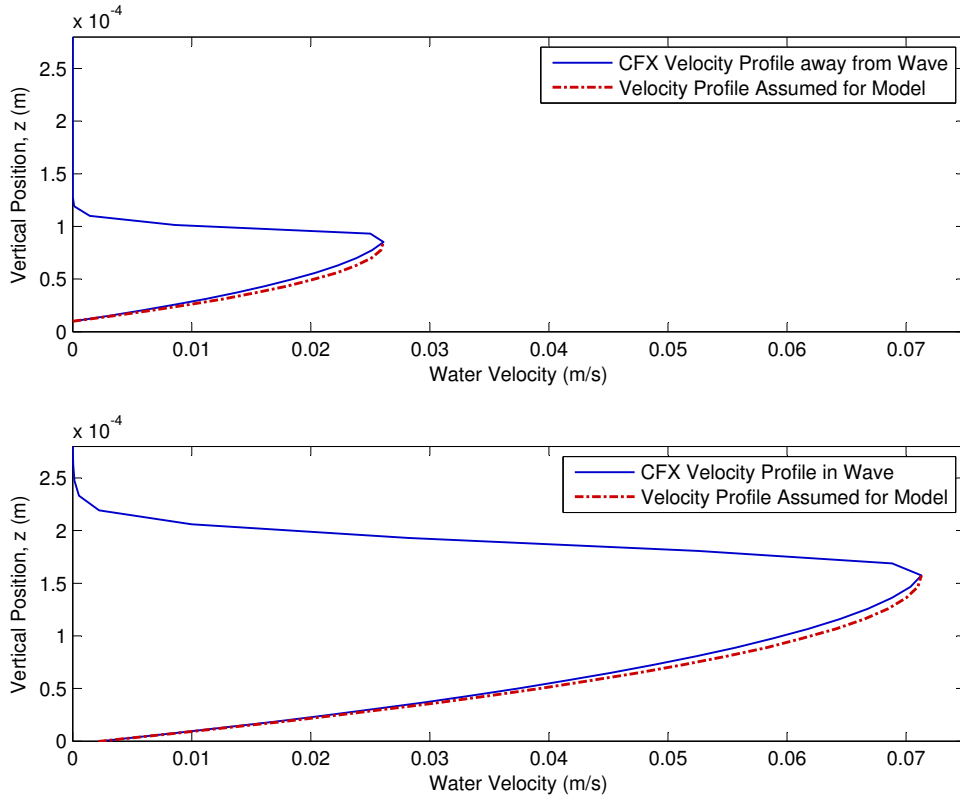


Figure 4.8: Velocity profile from CFX compared to model profile far from a wave (top) and in a wave (bottom). The flow parameters are $Re = 2.28$, $a_b = 0.1$, $\delta = 0.1$, $\cot \beta = 1.5$, and $We = 0$.

gradient at the free surface, and a steeper decline in velocity near the surface in the CFX results. Bottom topography does not appear impact the shape of the profile except to shift it up or down so that the velocity is zero at the bottom surface; both profiles have same shape, although the profile away from the wave was taken near a peak in the bottom topography, and the profile at the peak of the wave was taken at a trough in bottom topography.

Chapter 5

Results and Comparisons

Four comparisons of the models are made to determine which best predicts key features of the flow. First, the predictions of the critical Reynolds number, detailed in chapter 3, are contrasted and compared to the accepted theoretical result. Then, the neutral stability curves calculated from the model equations are compared to two sets of experimental data. Also, numerical simulations predicting the form of the fully developed interface are compared to those of the full Navier-Stokes equations. Finally, critical Reynolds number predictions for a wavy bottom case are compared with experimental data. Based on all of these results, the most realistic model that is able to faithfully predict key features of the flow is determined. While comparing the models, the effect of bottom topography and surface tension on the stability of the flow are also discussed in connection with the results presented.

5.1 Model Comparison

The three models are compared to determine which best predicts features of the flow. To evaluate and compare the performance of the models, four methods are employed. First, the critical Reynolds number at which the flow becomes unstable is calculated for the flat bottom case, and compared to the known theoretical value. Second, the neutral stability curve for each model is compared to two sets of experimental data collected by Liu et al. [16, 17]. Next, the evolution of the flow rate q , as predicted by the models, is compared to the solution of the full Navier-Stokes equations, which was obtained using the software package CFX. Finally, critical Reynolds number predictions for the weighted residual model for flow over a wavy bottom are compared to experimental results of Wierschem et al. [18]. Only the weighted residual and integral-boundary-layer models are included in the last two

comparisons since it will be clear from the first two comparisons that the SWM is the least realistic model.

5.1.1 Critical Reynolds Number for the Even Bottom Case

The critical Reynolds number for the case without bottom topography was calculated for each model, and the results are given in section 3.5. Here, they are compared to the theoretical value. The critical Reynolds number for a thin film flow down an even bottomed inclined plane has been determined by Benjamin [1] and Yih [2] using a perturbation solution of the corresponding Orr-Sommerfeld equation; this is taken to be the theoretical value. The result is that the critical Reynolds number is given by

$$Re_{crit} = \frac{5}{6} \cot \beta . \quad (5.1)$$

Performing a linear stability analysis on the shallow-water model, the integral-boundary-layer model, and the weighted residual model yields the following results:

$$Re_{crit}^{SWM} = \frac{5}{22} \cot \beta , \quad (5.2)$$

$$Re_{crit}^{IBL} = \cot \beta , \quad (5.3)$$

and

$$Re_{crit}^{WRM} = \frac{5}{6} \cot \beta , \quad (5.4)$$

respectively.

These results show that, of the three models considered, only the weighted residual model correctly predicts the critical Reynolds number. The integral-boundary-layer model predicts a critical Reynolds number slightly higher than the correct value, although it is still close. The shallow-water model gives a very poor prediction, significantly underestimating the critical Reynolds number.

5.1.2 Neutral Stability Curves

To further evaluate the performance of the three models, the neutral stability curves for each of the models are compared to experimental data. Two sets of experimental data are considered. The first is from experiments conducted by Liu, Paul, and Gollub in 1993 [16].

The experiment involved a glycerin-water film flowing down an incline at 5.6° . The material properties for the liquid include a kinematic viscosity of $\nu = (5.02 \pm 0.05) \times 10^{-6} \frac{\text{m}^2}{\text{s}}$, surface tension of $\gamma = (69 \pm 2) \times 10^{-3} \frac{\text{N}}{\text{m}}$, and a density of $\rho = 1.13 \frac{\text{g}}{\text{cm}^3}$. The Reynolds number at which the flow becomes unstable was measured for disturbances of various frequencies. The results are compared to the neutral stability curves of each of the three models in figure 5.1. The expressions for the neutral stability curves of the models are given in equations (3.28) to (3.30). It is worth noting that, because the material properties are set and the Reynolds number changes, the Weber number also changes along the curve.

As with the critical Reynolds number predictions, the weighted residual model most closely matches the experimental data. The integral-boundary-layer model is a slightly poorer predictor of the experimental data, suggesting that the flow will be stable at slightly higher Reynolds numbers than either the weighted residual model or the experimental data predict. The shallow water model again gives the poorest predictions, significantly underestimating the Reynolds number at which the flow will become unstable, for all wavenumbers. It should also be noted that the experimental data are for a very gentle incline, which is much more appropriate for the shallow-water model than for the integral-boundary-layer or weighted residual models; despite this, the weighted residual model gives the best predictions.

A second set of experimental data is compared to the model predictions in figure 5.2. These data were published by Liu, Schneider, and Gollub in 1995 [17]. The data are for a slightly different flow with a kinematic viscosity of $\nu = 2.3 \times 10^{-6} \frac{\text{m}^2}{\text{s}}$, surface tension of $\gamma = 67 \times 10^{-3} \frac{\text{N}}{\text{m}}$, and a density of $\rho = 1.07 \frac{\text{g}}{\text{cm}^3}$ down an incline of 4.0° . Again, the weighted residual model predicts a neutral stability curve closest to the experimental data. For most of the experimental data points, the weighted residual model curve is within the error bars; otherwise it is very close to the error bars. The integral-boundary-layer model is reasonably close, and the shallow water model gives the poorest results. It should also be noted that the experimental data in this case span a much larger range of Reynolds numbers. Recall that the models were developed assuming that the Reynolds number is $O(1)$; despite this, the weighted residual model predicts a neutral stability curve that falls within the error bars even at the highest Reynolds numbers for which experimental data are available. The critical Reynolds number predictions and the neutral stability curves compared with theoretical and experimental data show that the integral-boundary-layer and weighted residual models are much more reliable than the shallow-water model. For this reason, the shallow water model is excluded from further comparisons.

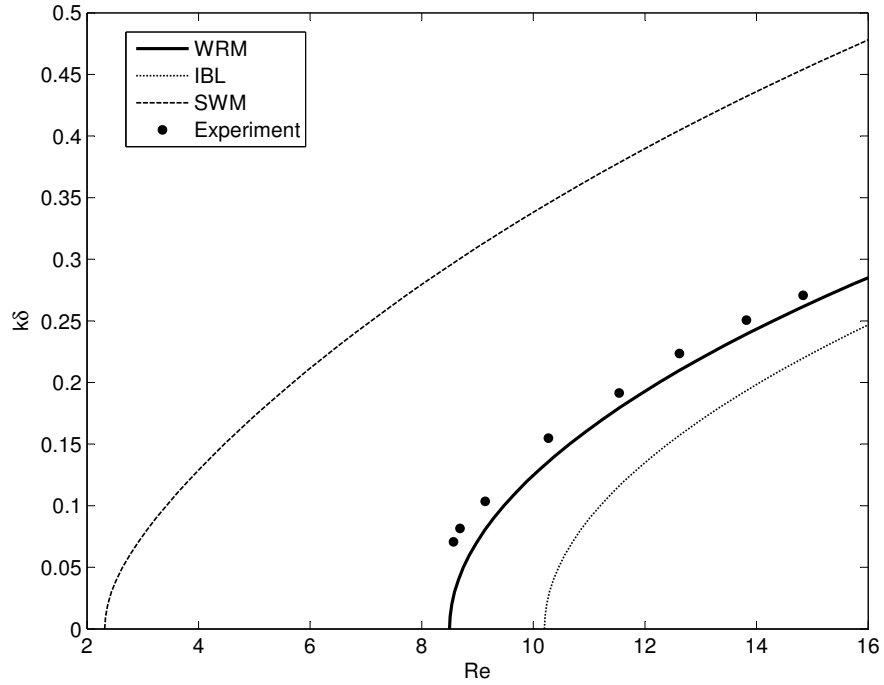


Figure 5.1: Neutral stability curves for each model compared to experimental data, reprinted from *Advances in Fluid Mechanics VIII*, Vol. 69, edited by M. Rahman and C.A. Brebbia, “Modelling gravity-driven flow over uneven surfaces,” pp.299-309, Copyright 2010, with permission from WIT Press, Southampton, UK [38]. The flow parameters are $\nu = (5.02 \pm 0.05) \times 10^{-6} \frac{\text{m}^2}{\text{s}}$, $\gamma = (69 \pm 2) \times 10^{-3} \frac{\text{N}}{\text{m}}$, $\rho = 1.13 \frac{\text{g}}{\text{cm}^3}$, and $\beta = 5.6^\circ$.

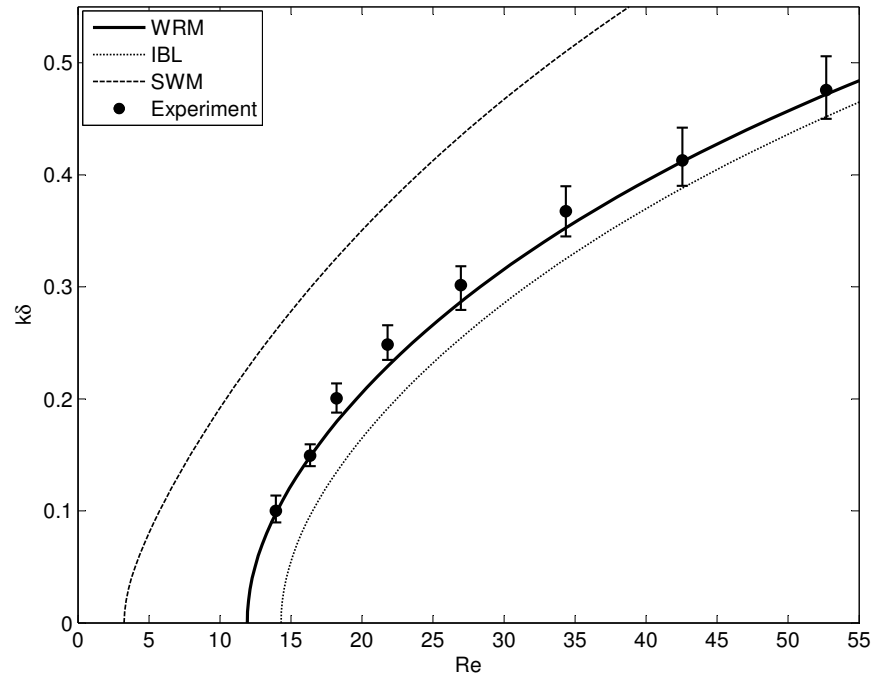


Figure 5.2: Neutral stability curves for each model compared to experimental data, modified and reprinted with permission from Cambridge University Press, from the article *Journal of Fluid Mechanics*, vol. 665, “Film flow over heated wavy inclined surfaces,” pp.418-456, Copyright 2010, by D’Alessio et al. [13]. The flow parameters are $\nu = 2.3 \times 10^{-6} \frac{\text{m}^2}{\text{s}}$, $\gamma = 67 \times 10^{-3} \frac{\text{N}}{\text{m}}$, $\rho = 1.07 \frac{\text{g}}{\text{cm}^3}$, and $\beta = 4.0^\circ$

5.1.3 Simulation Results Compared to Full Navier-Stokes Numerical Solutions

Numerical solutions of the model equations are compared to numerical simulations of the full Navier-Stokes equations to determine whether the models make reasonable predictions regarding the development of the fluid interface for unstable flows. The model equations are solved using the fractional step method described in section 4.1. Results using the weighted residual model and the integral-boundary-layer model are included; the shallow-water model is not considered due to the poor results in the previous comparisons. Also, the flow setup considered has a relatively steep incline that is appropriate for the integral-boundary-layer and weighted residual models, but is less appropriate for the shallow-water model. Numerical solutions to the full Navier-Stokes equations are obtained from the commercial software package CFX; the relevant numerical methods it uses are briefly described in section 4.2.

Results for each of the two models and from CFX are compared for a case having $Re = 2.28$, $\cot \beta = 1.5$, $We = 0$, $\delta = 0.1$, and $a_b = 0.1$; this is the case solved using CFX that was presented in section 4.2. Figure 5.3 shows the volume flow rate along the domain for each model and for CFX. Figure 5.4 shows the bottom topography and fluid interface.

The figures show that the number of peaks predicted by both models match the number of peaks predicted by CFX. The height of the peaks predicted by CFX is also closely matched by the weighted residual model; the integral-boundary-layer model predicts slightly shorter peaks. The location of the peaks is not expected to match between the model and CFX results because the results are not shown for the same time; they are simply shown for a fully developed interface in each case. However, the spacing between the peaks as predicted by CFX is not consistent with either of the models, which could be a minor shortcoming of the models. The reason for the discrepancy is unknown; however, Balmforth and Mandre [5] developed an amplitude equation which they used to demonstrate that a fully developed series of waves can be stable in two dimensions. They showed that if the distance between waves is small enough, the waves will combine and coarsening will occur, and if the distance is too large, instabilities will grow causing new waves to develop between existing waves. This indicates that the number of peaks and the spacing between them, of a fully developed interface within a domain of a given length, should vary insignificantly or not at all between occurrences of the same flow.

Comparisons between CFX and the model results are also made for a second case in which surface tension is included. The non-dimensional parameters are the same as in the case described above, with the exception of the Weber number, which is now non-zero so as

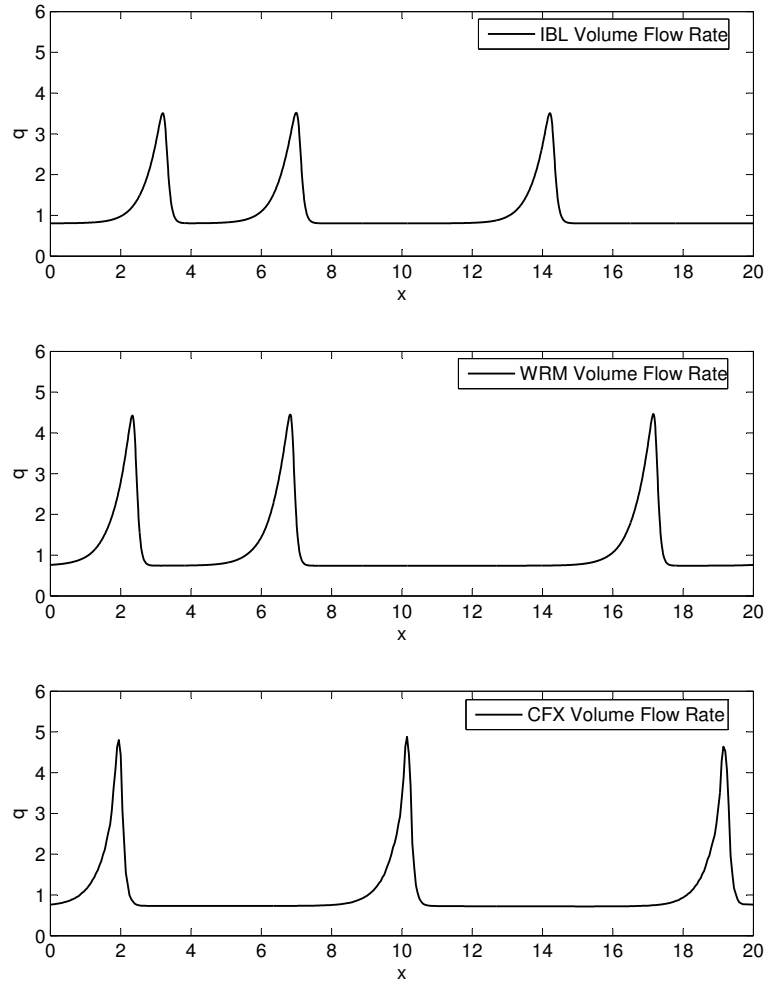


Figure 5.3: Volume flow rate along the domain for IBL, WRM, and CFX, reprinted from *Advances in Fluid Mechanics VIII*, Vol. 69, edited by M. Rahman and C.A. Brebbia, "Modelling gravity-driven flow over uneven surfaces," pp.299-309, Copyright 2010, with permission from WIT Press, Southampton, UK [38]. The flow parameters are $Re = 2.28$, $a_b = 0.1$, $\delta = 0.1$, $\cot \beta = 1.5$, and $We = 0$.

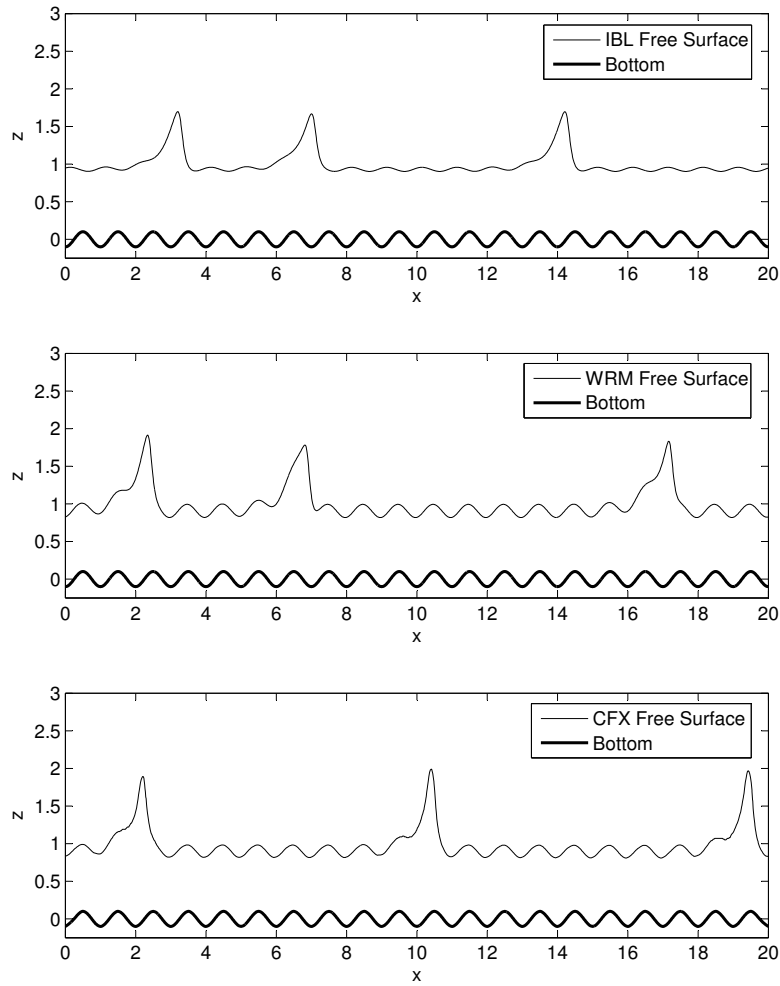


Figure 5.4: Free surface height and bottom position along the domain for IBL, WRM, and CFX, reprinted from *Advances in Fluid Mechanics VIII*, Vol. 69, edited by M. Rahman and C.A. Brebbia, "Modelling gravity-driven flow over uneven surfaces," pp.299-309, Copyright 2010, with permission from WIT Press, Southampton, UK [38]. The flow parameters are $Re = 2.28$, $a_b = 0.1$, $\delta = 0.1$, $\cot \beta = 1.5$, and $We = 0$.

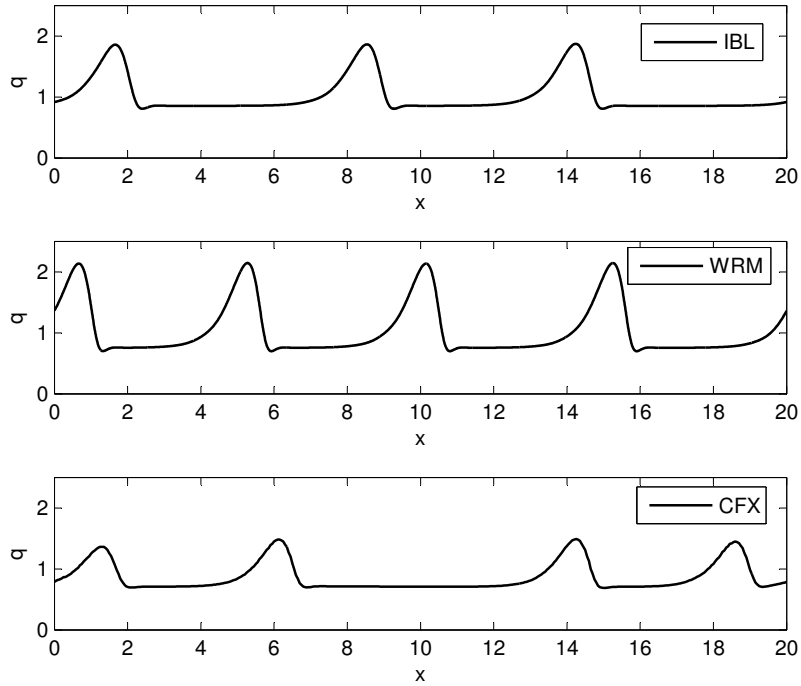


Figure 5.5: Volume flow rate along the domain for IBL, WRM, and CFX. The flow parameters are $Re = 2.28$, $a_b = 0.1$, $\delta = 0.1$, $\cot \beta = 1.5$, and $We = 5.05$.

to include surface tension. In this case, surface tension characterized by $We = 5.05$ is considered. The volume flow rate profile is shown in figure 5.5.

In this case, the number of peaks predicted by the weighted residual model matches the number of peaks in the CFX results, although the integral-boundary-layer model predicts one less peak. This suggests that the weighted residual model also predicts the interface development well when surface tension is included.

The peaks are much shorter in the CFX results than in either of the model results. However, this is not a good measure for evaluating the accuracy of the models because the CFX simulation is losing mass, which is causing the height of the peaks to decrease. The mass loss appears to be due to the inclusion of surface tension, as the mass loss for CFX cases with surface tension is approximately 6% after about 5 s of simulated time, whereas the mass loss for the previously discussed case without surface tension is only about 1.5% after almost 7 s of simulated time; these are the approximate times at which the results are shown. However, the mass loss is not expected to have an impact on the number of

peaks that develop because the number of peaks that develop by about 2 s stays constant for the remainder of the simulation; only the spacing, height, and relative height of the peaks change while most of the mass loss in the domain occurs. Therefore, the number of peaks is established before the mass loss becomes significant.

Both comparisons of the model solutions to the full Navier-Stokes equations show that the weighted residual model closely predicts the final shape of the interface calculated from the full equations. The integral-boundary-layer model also gives reasonable predictions, although the weighted residual model results are closer in the height of the peaks predicted for the first case, and in the number of peaks predicted in the second case.

5.1.4 Critical Reynolds Number with Bottom Topography

As a final method of validating the integral-boundary-layer and weighted residual models, the critical Reynolds number of flow over a wavy bottom, as predicted by the model equations, is compared to experimental results collected by Wierschem et al. [18]. To consider the effect of bottom topography on the stability of the flow, a sinusoidal bottom profile is assumed, which is consistent with the experiments performed by Wierschem et al. [18]. The critical Reynolds number for flow over a wavy bottom can be found from the model equations by applying Floquet theory to calculate the growth rate of disturbances of a given wavenumber. The Reynolds number at which the growth rate is zero is then determined for a sufficient selection of perturbation wavenumbers. The neutral stability curve can then be constructed, thus revealing the smallest Reynolds number for the onset of instability.

Floquet theory is applied to the linearized perturbation equations, which for the weighted residual model take the form,

$$\frac{\partial \hat{h}}{\partial t} + \frac{\partial \hat{q}}{\partial x} = 0, \quad (5.5)$$

$$\frac{\partial \hat{q}}{\partial t} + f_1 \frac{\partial^2 \hat{q}}{\partial x^2} + f_2 \frac{\partial \hat{q}}{\partial x} + f_3 \hat{q} + f_4 \frac{\partial^3 \hat{h}}{\partial x^3} + f_5 \frac{\partial^2 \hat{h}}{\partial x^2} + f_6 \frac{\partial \hat{h}}{\partial x} + f_7 \hat{h} = 0, \quad (5.6)$$

where the coefficients are given by f_1 to f_7 in Appendix A with $Bi = Ma = \delta_1 = 0$, and

are periodic functions of x . The perturbations are assumed to be of the form

$$\hat{h}(x, t) = e^{iKx + \sigma t} \sum_{n=-\infty}^{\infty} \hat{h}_n e^{in2\pi x} , \quad (5.7)$$

$$(5.8)$$

$$\hat{q}(x, t) = e^{iKx + \sigma t} \sum_{n=-\infty}^{\infty} \hat{q}_n e^{in2\pi x} . \quad (5.9)$$

The coefficients f_1 to f_7 are also expanded in a similar series. Truncating the complex Fourier series allows the problem to be re-written as a linear algebra problem; choosing a set of parameters and a perturbation wavenumber, this system of equations can be solved for the growth rate of the perturbation. The neutral stability curve is constructed by systematically searching for the Reynolds number at which the growth rate is zero for a set of perturbation wavenumbers, and the critical Reynolds number is then found. This process is described in detail in Appendix A.

The experimental results are compared to the model predictions in table 5.1. The experimental data collected by Wierschem et al. have the nondimensional parameters $a_b \delta = 0.05$, $9.7 \times 10^{-7} \leq We \leq 6.2 \times 10^{-5}$, and a domain length of three bottom wavelengths. For the calculations of the models' critical Reynolds numbers, the parameters used are $a_b = 0.5$, $\delta = 0.1$, and $We = 3.15 \times 10^{-5}$. The data include three angles of inclination, indicated in the first column on the left. The second column from the left gives the critical Reynolds number for flow over an even bottom incline at the given angle of inclination. The third column gives the experimental results of Wierschem et al. In the fourth column, the critical Reynolds number of the flow, according to transient solutions of the model equations, is given. To obtain this value, transient simulations with the appropriate parameters were run for various Reynolds numbers to determine at which Reynolds number the flow becomes unstable; a domain of ten bottom wavelengths was used because, for shorter domains, the results were found to vary with the domain length [13]. These data were collected by D'Alessio et al. [13]. The second column from the right gives the critical Reynolds number as predicted from the weighted residual model equations using a linear stability analysis with Floquet theory; these data were also collected by D'Alessio et al. [13]. Finally, on the far right, results of the linear stability analysis using Floquet theory with the integral-boundary-layer model are presented.

The table shows several results worth noting. First, it indicates that bottom topography stabilizes the flow, as the critical Reynolds numbers with bottom topography are greater than the corresponding even bottom case. This is discussed further in section 5.2. The comparison also shows that the linear stability analysis predictions for both models match

Table 5.1: Comparison between experimental, numerical and theoretical values of Re_{crit} for a wavy-incline case with $\delta = 0.1$.

θ	Re_{crit}^{even}	Re_{crit}		Re_{crit} Theoretical	
		Experimental [18]	WRM Numerical [13]	WRM [13]	IBL
15°	3.1	5.1 ± 0.4	(5.5,5.6)	5.6	6.3
30°	1.4	2.2 ± 0.2	(1.8,1.9)	1.7	2.4
40.7°	0.97	1.3 ± 0.1	(1.1,1.2)	1.1	1.5

the experimental results fairly well, with the integral-boundary-layer model performing slightly better for moderate inclines and the weighted residual model giving better results for gentle inclines. For steep inclines, the two models perform equally well. Finally, the critical Reynolds number found numerically, which includes non-linear effects, matches the experimental data extremely well, falling within 0.1 of the experimental error; this shows that even when the linear theoretical result is not within the error of the experiment, the model, which incorporates non-linear effects, closely predicts the experimental result.

In each of the first three comparisons, the weighted residual model yielded the best agreement with the corresponding reference solution; it best matched the theoretical value of the critical Reynolds number, the experimental neutral stability curves, and the numerical simulations of the full Navier-Stokes solutions. This shows that the weighted residual model is the most realistic of the three models considered. Further, it was found to perform quite well and on par with the integral-boundary-layer model in predicting the critical Reynolds number for flow over a wavy bottom. As such, it will be the only model used to consider the problem including bottom heating and porosity, which is the focus of chapter 6.

5.2 Effect of Surface Tension and Bottom Amplitude on Stability of Flow

To determine the effect of surface tension and bottom topography on the stability of the flow, an asymptotic analysis is conducted. This analysis shows how bottom topography, through a_b , and surface tension, through the Weber number, affect the steady state volume flow rate. More details of this analysis are provided in Appendix B. Each of the steady-state flow variables are expanded in a perturbation series about the small shallowness parameter, δ :

$$\begin{aligned}
u_s(x, z) &= u_0(x, z) + \delta u_1(x, z) + \delta^2 u_2(x, z) + \dots, \\
w_s(x, z) &= w_0(x, z) + \delta w_1(x, z) + \delta^2 w_2(x, z) + \dots, \\
p_s(x, z) &= p_0(x, z) + \delta p_1(x, z) + \delta^2 p_2(x, z) + \dots, \\
h_s(x) &= h_0 + \delta h_1(x) + \delta^2 h_2(x) + \dots
\end{aligned} \tag{5.10}$$

The steady-state series solution for h is found using the weighted residual model equations. The continuity equation requires that q is constant; assuming $q = 1$, the series for h is substituted into the steady-state model equation,

$$\begin{aligned}
&\frac{5\delta^2 \text{We}}{6} h_s^3 h_s''' - \frac{6\delta}{\text{Re}} h_s h_s'' + \frac{4\delta}{\text{Re}} (h_s')^2 - \left[\frac{5 \cot \beta}{2\text{Re}} h_s^3 + \frac{5\delta}{2\text{Re}} \zeta' - \frac{9}{7} \right] h_s' - \frac{15\delta}{4\text{Re}} \zeta'' h_s \\
&+ \left[\frac{5}{2\delta \text{Re}} - \frac{5 \cot \beta}{2\text{Re}} \zeta' + \frac{5\delta^2 \text{We}}{6} \zeta''' \right] h_s^3 = \frac{5}{2\delta \text{Re}} + \frac{5\delta}{\text{Re}} (\zeta')^2
\end{aligned} \tag{5.11}$$

This is separated into a closed problem at each order of δ and each of these is solved to find h_0, h_1, h_2, h_3 , and h_4 . For example, h_0, h_1 and h_2 are found to be

$$\begin{aligned}
h_0 &= 1, \\
h_1(x) &= \frac{\cot \beta}{3} \zeta'(x), \\
h_2(x) &= \frac{2}{3} \left(1 + \frac{\cot^2 \beta}{3} \right) [\zeta'(x)]^2 + \left(\frac{1}{2} - \frac{2\text{Re} \cot \beta}{35} + \frac{\cot^2 \beta}{9} \right) \zeta''(x).
\end{aligned} \tag{5.12}$$

The expansions for u_s, w_s , and p_s are substituted into the governing equations and boundary conditions, equations (2.23) to (2.25) and (2.26) to (2.28), resulting in a closed problem at each order of δ . For example, the leading order problem is found to be

$$\frac{\partial p_0}{\partial z} = -\frac{3 \cot \beta}{\text{Re}}, \quad \frac{\partial^2 u_0}{\partial z^2} = -3, \quad \frac{\partial w_0}{\partial z} = -\frac{\partial u_0}{\partial x}, \tag{5.13}$$

with boundary conditions

$$u_0 = w_0 = 0 \text{ at } z = \zeta(x) \quad \text{and} \quad p_0 = \frac{\partial u_0}{\partial z} = 0 \text{ at } z = 1 + \zeta(x). \tag{5.14}$$

The problem can be solved to find

$$\begin{aligned}
p_0(x, z) &= \frac{3 \cot \beta}{\text{Re}} (1 + \zeta - z), \\
u_0(x, z) &= -\frac{3}{2} (z - \zeta)^2 + 3(z - \zeta), \\
w_0(x, z) &= -\frac{3}{2} \zeta' (z - \zeta)^2 + 3\zeta' (z - \zeta).
\end{aligned} \tag{5.15}$$

These problems are solved to find solutions up to $O(\delta^4)$, which is where the Weber number first appears in the expression for the average volume flow rate. The streamwise velocity u_s can be evaluated at the free surface, which gives the even bottom value plus a *mean surface drift* that results from the wavy bottom [13]. To $O(\delta^2)$, this drift is,

$$\bar{u}_s - \frac{3}{2} \approx - \left(2 + \frac{7}{18} \cot^2 \beta \right) \pi^2 a_b^2 \delta^2 . \quad (5.16)$$

The deviation from the even bottom steady state velocity is a decrease in the overall velocity, which stabilizes the flow, as shown in the critical Reynolds number comparison to experimental data in section 5.2. This confirms that the effect of bottom topography and negligible surface tension is to stabilize the flow. To find the effect of surface tension, the volume flow rate is considered. The series solution for u is integrated in z through the fluid layer thickness and in x across one bottom wavelength to find the average volume flow rate. The resulting expression for the average volume flow rate is

$$\bar{Q}_s \approx - \left(2 + \frac{7}{18} \cot^2 \beta \right) \pi^2 a_b^2 \delta^2 + f(\text{We}, Re, a_b, \cot \beta) \pi^4 a_b^2 \delta^4 , \quad (5.17)$$

where

$$\begin{aligned} f(\text{We}, Re, a_b, \cot \beta) = & \left(38 - \frac{1193}{8} a_b^2 \right) \frac{\cot^4 \beta}{81} - \frac{152}{315} Re \cot^3 \beta + \left(66 + \frac{63139}{53900} Re^2 - 4a_b^2 \right) \frac{\cot^2 \beta}{9} \\ & - \left(\frac{59}{60} + \frac{76}{27} \text{We} \right) Re \cot \beta + \frac{51}{10} + \frac{16}{3} a_b^2 . \end{aligned} \quad (5.18)$$

This analysis, valid for $\text{We} = O(1)$, shows that surface tension has a stabilizing effect on the flow, as the volume flow rate of the fluid is decreased by increasing the Weber number. Decreasing the volume flow rate gives a lower Reynolds number for an otherwise similar flow of the same fluid layer thickness; however, since the Reynolds number is calculated assuming flow over an even bottom and is therefore not reduced by presence of surface tension and bottom topography, the critical Reynolds number must instead increase to correctly predict the onset of instability. This result is confirmed by D'Alessio et al. [13], using a linear stability analysis of the weighted residual model equations. However, D'Alessio et al. [13] also show that for larger surface tension, the effect of surface tension is reversed, and actually destabilizes the flow. These effects are discussed further in chapter 6.

Chapter 6

Thermoporous Problem

Although the basic problem addressed in Chapters 1 to 5 provides insight into the dynamics of thin film flow over an inclined plane, further details of the problem can be uncovered by considering the effects of other factors that would likely influence the flow. For example, heat transfer could affect the dynamics of the flow by causing variations in the flow properties, such as the surface tension. Furthermore, alternative bottom surface conditions such as a permeable, wavy bottom surface could also impact characteristics of the flow such as the flow rate and stability.

Bottom heating has been considered by Kalliadasis et al. [23], who studied flow over an even bottom using the integral-boundary-layer approach, by Scheid et al. [25], who used a specified flux rather than a constant temperature for the bottom boundary condition, and by Trevelyan et al. [7], who looked at flow over an even incline and analyzed the case of a constant temperature bottom and a bottom with a specified heat flux, using the weighted residual model.

Bottom porosity has been investigated in relation to this problem by Pascal [26], who studied the stability of the flow using the Orr-Sommerfeld equation, and by Pascal and D'Alessio [8], who applied the weighted residual model to the problem and also considered bottom topography. Similar problems have also been considered for particular applications, such as by Nong et al. [9], who have developed a model for tear flow over a permeable contact lens. Recently, Sadiq et al. [4] studied flow over an even bottom surface with both bottom heating and permeability. In this chapter, bottom heating, permeability, and bottom topography are all considered together, and a weighted residual model that describes this flow is developed. A specified bottom temperature condition is used, and a saturated permeable bottom surface is modelled using the Beavers and Joseph slip condition [27]. Removing bottom topography from the problem will enable comparisons to be made with

the results of Sadiq et al. [4].

6.1 Governing Equations and Boundary Conditions

The governing equations for the problem including heating and bottom permeability are the same as those for the isothermal, impermeable problem, with the addition of an equation describing the conservation of energy. The non-dimensional governing equations are

$$\frac{\partial u}{\partial x} + \frac{\partial w}{\partial z} = 0, \quad (6.1)$$

the continuity equation,

$$\delta Re \left(\frac{\partial u}{\partial t} + u \frac{\partial u}{\partial x} + w \frac{\partial u}{\partial z} \right) = -\delta Re \frac{\partial P}{\partial x} + 3 + \frac{\partial^2 u}{\partial z^2}, \quad (6.2)$$

which describes conservation of x -momentum,

$$\delta^2 Re \left(\frac{\partial w}{\partial t} + u \frac{\partial w}{\partial x} + w \frac{\partial w}{\partial z} \right) = -Re \frac{\partial P}{\partial z} - 3 \cot \beta + \delta \frac{\partial^2 w}{\partial z^2}, \quad (6.3)$$

which describes conservation of z -momentum, and

$$\delta Pe \left(\frac{\partial T}{\partial t} + u \frac{\partial T}{\partial x} + w \frac{\partial T}{\partial z} \right) = \frac{\partial^2 T}{\partial z^2}, \quad (6.4)$$

which describes the conservation of energy. The equations are non-dimensionalized using the same non-dimensional parameters and scaling as those used in section 2.1, with the addition of T , the fluid temperature, and $Pe = PrRe$, which is the Peclet number that quantifies the strength of advection compared to thermal diffusion. Temperature is non-dimensionalized so that the non-dimensional bottom temperature is unity and the ambient temperature outside of the flow is zero.

The interface boundary conditions are similar to those for the isothermal, impermeable problem, although there are additional terms due to the heating. As well, there are added boundary conditions at both the bottom surface and the interface to describe the temperature or heat transfer at these boundaries. Finally, the boundary conditions must be modified to deal with the porous interface along the bottom surface. Three additional non-dimensional parameters are required for the boundary conditions. These are the Biot and Marangoni numbers, which describe the heating, and a parameter to describe the permeability of the bottom. The permeability parameter is another small parameter, as

shown by Beavers and Joseph [27], and is assumed to be $O(\delta)$. These non-dimensional parameters are defined as

$$Bi = \frac{\alpha_g H}{\rho c_p \kappa_T}, \quad Ma = \frac{\gamma \Delta T}{\rho U^2 H}, \quad \delta_1 = \frac{\sqrt{\kappa}}{\alpha H}, \quad (6.5)$$

where α_g is the convective heat transfer coefficient at the free surface, c_p is the specific heat capacity at constant pressure, κ_T is the thermal diffusivity, γ describes the decrease in surface tension with increase in temperature, κ is the permeability of the bottom surface, $\Delta T = T_b - T_a$ is the change in temperature from the ambient surroundings to the bottom surface, and α is a dimensionless parameter related to the permeable bottom properties, described by Beavers and Joseph [27].

At the free surface, the dimensional dynamic conditions are

$$\begin{aligned} P_a + \hat{n} \cdot \tau \cdot \hat{n} &= -\sigma(T) \vec{\nabla} \cdot \hat{n}, \\ \hat{n} \cdot \tau \cdot \hat{t} &= \vec{\nabla} \sigma(T) \cdot \hat{t}. \end{aligned} \quad (6.6)$$

The normal and tangential vectors at the interface are given by

$$\hat{n} = \left(\begin{array}{c} -\frac{\partial(\zeta+h)}{\partial x} \\ 1 \end{array} \right) \frac{1}{\sqrt{1 + \left(\frac{\partial(\zeta+h)}{\partial x} \right)^2}}, \quad (6.7)$$

and

$$\hat{t} = \left(\begin{array}{c} 1 \\ \frac{\partial(\zeta+h)}{\partial x} \end{array} \right) \frac{1}{\sqrt{1 + \left(\frac{\partial(\zeta+h)}{\partial x} \right)^2}}, \quad (6.8)$$

respectively. The surface tension is assumed to vary linearly with temperature according to the equation

$$\sigma = \sigma_0 - \gamma(T - T_0), \quad (6.9)$$

where σ_0 is the surface tension at T_0 , and γ quantifies the change in surface tension with temperature. The dynamic boundary condition can then be non-dimensionalized and written in the following way for the specific problem of flow down an inclined, wavy plane:

$$P - P_a = \frac{2\delta}{Re \left(1 + \delta^2 \left(\frac{\partial(h+\zeta)}{\partial x} \right)^2 \right)} \left(\frac{\partial w}{\partial z} - \frac{\partial h + \zeta}{\partial x} \frac{\partial u}{\partial z} \right) - \delta^2 \frac{We - MaT}{\left(1 + \delta^2 \left(\frac{\partial(h+\zeta)}{\partial x} \right)^2 \right)^{\frac{3}{2}}} \frac{\partial^2(h+\zeta)}{\partial x^2}, \quad (6.10)$$

which ensures continuous normal stress across the interface [13], and

$$\begin{aligned} & \left(\frac{\partial u}{\partial z} + \delta^2 \frac{\partial w}{\partial x} \right) \left(1 - \delta^2 \left(\frac{\partial(h+\zeta)}{\partial x} \right)^2 \right) - 4\delta^2 \frac{\partial(h+\zeta)}{\partial x} \frac{\partial u}{\partial x} \\ & = -MaRe\delta \sqrt{\left(1 + \delta^2 \left(\frac{\partial(h+\zeta)}{\partial x} \right)^2 \right)} \left(\frac{\partial T}{\partial x} + \frac{\partial(h+\zeta)}{\partial x} \frac{\partial T}{\partial z} \right) , \end{aligned} \quad (6.11)$$

which describes continuous tangential stress across the interface [13]. Retaining only terms to $O(\delta^2)$, these conditions become

$$\left. \begin{aligned} & p - \frac{2\delta}{Re} \frac{\partial w}{\partial z} + \delta^2 (We - MaT) \frac{\partial^2(h+\zeta)}{\partial x^2} \\ & \frac{\partial u}{\partial z} - 4\delta^2 \frac{\partial(h+\zeta)}{\partial x} \frac{\partial u}{\partial x} + MaRe\delta \left(\frac{\partial T}{\partial x} + \frac{\partial(h+\zeta)}{\partial x} \frac{\partial T}{\partial z} \right) = 0 \end{aligned} \right\} \text{at } z = \eta . \quad (6.12)$$

The kinematic condition at the interface remains unchanged from the isothermal and impermeable problem, and is given non-dimensionally by

$$\frac{\partial h}{\partial t} = w - u \left(\zeta' + \frac{\partial h}{\partial x} \right) . \quad (6.13)$$

Finally, the heat transfer at the interface occurs through convection, and is described in dimensional form by

$$\vec{\nabla} T \cdot \hat{n} = \frac{-\alpha_g}{\rho c_p \kappa_T} (T - T_a) . \quad (6.14)$$

Temperature is non-dimensionalized using

$$\hat{T} = \frac{T - T_a}{T_b - T_a} , \quad (6.15)$$

the Biot number given in equation (6.5) is used, and the normal vector at the surface defined by equation (6.7) is used to simplify and non-dimensionalize the boundary condition to

$$-BiT \sqrt{1 + \delta^2 \left(\frac{\partial(h+\zeta)}{\partial x} \right)^2} = \frac{\partial T}{\partial z} - \delta^2 \frac{\partial(h+\zeta)}{\partial x} \frac{\partial T}{\partial x} \text{ at } z = \eta , \quad (6.16)$$

where the hats on the non-dimensional temperature have been dropped. To $O(\delta^2)$, this becomes

$$-BiT \left(1 + \frac{\delta^2}{2} \left(\frac{\partial(h+\zeta)}{\partial x} \right)^2 \right) = \frac{\partial T}{\partial z} - \delta^2 \frac{\partial(h+\zeta)}{\partial x} \frac{\partial T}{\partial x} \text{ at } z = \eta . \quad (6.17)$$

The bottom boundary conditions include two expressions that come from the Beavers and Joseph slip condition, which has been extended by Saffman [28] to apply to uneven bottom topography. The bottom slip condition, derived by Saffman [28] and used by Pascal and D'Alessio [8], is given in dimensional vector form by

$$\frac{\partial v^{\parallel}}{\partial \hat{n}} = \vec{\nabla} v^{\parallel} \cdot \hat{n} = \frac{\alpha}{\sqrt{\kappa}} (v^{\parallel} - v_p^{\parallel}) , \quad (6.18)$$

where v^{\parallel} is the tangential part of the velocity along the bottom surface, \hat{n} is the normal vector along the bottom surface, given in equation (2.6), and the subscript p indicates a quantity in the permeable medium. The tangential velocity is given by

$$v^{\parallel} = \frac{u + \zeta' w}{\sqrt{1 + (\zeta')^2}} . \quad (6.19)$$

Equation (6.18) can be evaluated to find

$$\begin{aligned} & \frac{1}{(1 + (\zeta')^2)^2} [(1 + (\zeta')^2) (u_z + \zeta' w_z - \zeta' u_x - \zeta' \zeta'' w - (\zeta')^2 w_x) + (\zeta')^2 \zeta'' (u + \zeta' w)] = \\ & \frac{\alpha}{\sqrt{\kappa}} \frac{1}{\sqrt{1 + (\zeta')^2}} (u + \zeta' w - (u_p + \zeta' w_p)) . \end{aligned} \quad (6.20)$$

This expression is non-dimensionalized using the previously given scales as well as some additional information. First, the characteristic velocity in the porous medium compared to that in the fluid layer is assumed to be $O(\delta^3)$. This is because the characteristic velocity scale in the porous medium is given by

$$U_p = O\left(\frac{\kappa}{\mu} \rho g \sin \beta\right) . \quad (6.21)$$

Using the velocity scale given in equation (2.17), the order of magnitude of the ratio of the two scales is found to be

$$\frac{U_p}{U} = O\left(\left(\frac{\sqrt{\kappa}}{H}\right)^2\right) = O(\alpha^2 \delta_1^2) . \quad (6.22)$$

From the experiments of Beavers and Joseph [27], it can be assumed that $\alpha^2 = O(\delta)$; also, δ_1 is assumed to be $O(\delta)$, so $\frac{U_p}{U} = O(\delta^3)$. In this way, the velocities in the porous medium can be neglected since the model will only be second order. Equation (6.20) can therefore be non-dimensionalized and, neglecting higher order terms, simplified to

$$\delta_1 \frac{\partial u}{\partial z} = u + \delta^2 \zeta' w . \quad (6.23)$$

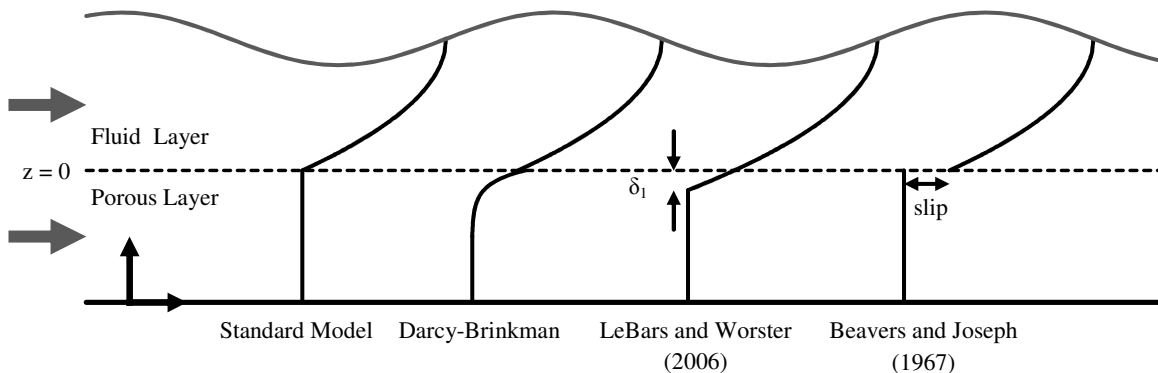


Figure 6.1: Models for flow over a porous layer, adapted from LeBars and Worster [39], reprinted with permission from Cambridge University Press.

The other bottom boundary condition comes from the requirement that the normal velocity out of the porous medium equals the normal velocity into the fluid layer, which simply comes from conservation of mass. This condition can be expressed as

$$v^\perp = v_p^\perp . \quad (6.24)$$

where v^\perp is the normal velocity at the bottom surface given by

$$v^\perp = \frac{u\zeta' - w}{\sqrt{1+(\zeta')^2}} . \quad (6.25)$$

This condition can be non-dimensionalized in the same way as equation (6.18). To second order, the boundary condition is

$$w = u\zeta' . \quad (6.26)$$

These boundary conditions come from the idea that there is a difference, or ‘slip-velocity’, between the flow through the porous layer and the flow at the porous interface. The physical interpretation of this model, along with three others, is shown in figure 6.1.

The figure shows four models for flow over porous surfaces. On the far left, a standard model of matching the flow at the interface to the flow through the porous layer is shown [9]. Shown second from the left is the Darcy-Brinkman model, which comes from a set of equations that model both the flow in the liquid layer and the flow in the porous layer in a single domain [39]. This model reveals a thin boundary layer in the porous region at the edge of the liquid layer, which causes the fluid at the liquid-porous interface to have a velocity

higher than the fluid in the bulk of the porous layer; however, since the Darcy-Brinkman equations model both the porous and liquid layers in one domain, they cannot be used directly to obtain a boundary condition at the interface for the current problem. Instead, this idea is reflected in the Beavers and Joseph model, shown on the far right, which defines a slip velocity between the flow through the porous medium and the flow in the liquid layer at the porous boundary. This slip velocity models the effect of the boundary layer in the porous medium, and also gives a specific boundary condition for the liquid layer at the porous interface. Third from the left of figure 6.1, the recent LeBars and Worster model is shown. This model matches the liquid velocity to the velocity through the porous layer at a point slightly below the porous interface, where this distance is approximately the thickness of the viscous boundary layer in the porous region [39]. This model is not used for the current problem because it does not give a boundary condition at the liquid-porous interface. The Beavers and Joseph model is used here because it provides the most accurate boundary condition at the porous interface, so the liquid layer can be modelled separately from the porous layer, and it is more accurate than the standard model [27].

A condition on the heat transfer at the bottom surface is also required, and a constant temperature condition is imposed using

$$T = 1 . \tag{6.27}$$

Trevelyan et al. [7] consider both constant temperature and specified heat flux boundary conditions, noting that the specified heat flux is more accurate when modelling the flow using a wall that loses heat to both the fluid and the ambient air. However, in certain applications, the constant temperature boundary condition may be more appropriate, such as in the application considered by Nong et al. [9], which was a tear layer flowing over a contact lens. In that case, the eye would be maintained at a constant temperature as a result of the body heating the eye. Furthermore, for small $Pe = PrRe$ and in the long wave limit, Trevelyan et al. [7] note that the critical conditions are identical, so in this case, either condition could be used to investigate the impact of heating on the stability of the flow. In the current problem, only the constant temperature boundary condition is used, as it is the simplest to implement and it is also relevant to some applications.

6.2 Model Development

The weighted residual model, which was shown to be the most accurate in making predictions about the flow over a wavy, isothermal, impermeable surface, is developed for the problem including heating and bottom permeability. The model is developed in a way that is very similar to the basic problem discussed in Chapter 3. The pressure is eliminated

from equations (6.2) and (6.3) by integrating the z -momentum equation from z to the free surface and applying the normal stress dynamic boundary condition for the pressure at the free surface. The expression for $P(x, z, t)$ is then used in the x -momentum equation to eliminate pressure. This leaves the continuity equation, a single momentum equation, and the energy equation. Velocity and temperature profiles are then assumed; the velocity profile is chosen to be

$$u(x, z, t) = \frac{3q}{2(h^3 + 3\delta_1 h^2)} b + \frac{\delta Ma Re}{4h} \frac{\partial \theta}{\partial x} b_1 \quad \text{where}$$

$$b = (z - \zeta)(2h + z - \zeta) + 2\delta_1 h \quad \text{and} \quad (6.28)$$

$$b_1 = (z - \zeta)(2h - 3(z - \zeta)) .$$

It is chosen to satisfy the boundary conditions to $O(\delta)$ and to satisfy

$$\int_{\zeta}^{h+\zeta} u(x, z, t) dz = q(x, t) . \quad (6.29)$$

It is not possible to satisfy the bottom slip condition involving u to $O(\delta\delta_1)$ while also satisfying equation (6.29), so the boundary condition is only satisfied to $O(\delta)$; this is acceptable because δ_1 is assumed to be $O(\delta)$, so the error is approximately $O(\delta^2)$. The temperature profile, chosen to be linear to match the steady state solution, is

$$T = 1 + \frac{\theta - 1}{h} (z - \zeta) , \quad (6.30)$$

where θ is the temperature at the interface. This profile satisfies the bottom temperature boundary condition, but not the surface temperature boundary condition. However, the surface temperature boundary condition is used in the development of the model when the equations are integrated in z , so its effect is accounted for in the model. The momentum and energy equations are then multiplied by weight functions before integrating in z . The weight functions used are b from equation (6.28) for the momentum equation, and $(z - \zeta)$ for the energy equation, which is the shape of the temperature profile. The equations are then integrated through the fluid layer thickness to eliminate the z -dependence. The final model equations are

$$\frac{\partial h}{\partial t} + \frac{\partial q}{\partial x} = 0 ,$$

$$\begin{aligned}
& \delta (h + 2\delta_1) \frac{\partial q}{\partial t} = \delta^3 h W\tilde{e} \left(\zeta''' + \frac{\partial^3 h}{\partial x^3} \right) \\
& + \frac{\delta^2}{Re} \left(\frac{9}{2} h \frac{\partial^2 q}{\partial x^2} - \frac{9}{2} \frac{\partial q}{\partial x} \frac{\partial h}{\partial x} - 6q \frac{\partial^2 h}{\partial x^2} - \frac{15}{4} q \zeta'' + \frac{q}{h} \left(4 \left(\frac{\partial h}{\partial x} \right)^2 - 5 (\zeta')^2 - \frac{5}{2} \frac{\partial h}{\partial x} \zeta' \right) \right) \\
& + \delta^2 h Re Ma \left(\frac{1}{48} h^2 \frac{\partial^2 \theta}{\partial x \partial t} + \frac{15}{224} h q \frac{\partial^2 \theta}{\partial x^2} + \frac{19}{336} h \frac{\partial q}{\partial x} \frac{\partial \theta}{\partial x} + \frac{5}{112} q \frac{\partial \theta}{\partial x} \frac{\partial h}{\partial x} \right) \\
& + \delta \left(\frac{9}{7} \frac{q^2}{h} \frac{\partial h}{\partial x} - \frac{45}{16} \delta_1 \frac{q^2}{h^2} \zeta' - \frac{5}{2} Ma \frac{\partial \theta}{\partial x} \left(\frac{h}{2} + \delta_1 \right) - \frac{17}{7} q \frac{\partial q}{\partial x} \left(1 + \frac{\delta_1}{h} \right) \right) \\
& + \delta \left(-\frac{5}{2} \frac{h \cot(\beta)}{Re} \left(\frac{\partial h}{\partial x} + \zeta' \right) (h + 3\delta_1) \right) + \frac{5}{2} \frac{h}{Re} (h + 3\delta_1) - \frac{5}{2} \frac{q}{h Re} , \\
& \delta h \frac{\partial \theta}{\partial t} = \delta^2 \left(-\frac{3}{2} \frac{Bi}{Pe} \theta \left(\zeta' + \frac{\partial h}{\partial x} \right)^2 + \frac{3}{40} Ma Re h^2 \left(\frac{\partial \theta}{\partial x} \right)^2 + \frac{h}{Pe} \frac{\partial^2 \theta}{\partial x^2} + \frac{1}{Pe} \frac{\partial \theta}{\partial x} \frac{\partial h}{\partial x} \right) \\
& + \delta^2 (\theta - 1) \left(\frac{3}{80} Ma Re h \left(h \frac{\partial^2 \theta}{\partial x^2} + 2 \frac{\partial \theta}{\partial x} \frac{\partial h}{\partial x} \right) + \frac{3}{Pe h} \zeta' \frac{\partial h}{\partial x} + \frac{2}{Pe h} \left(\frac{\partial h}{\partial x} \right)^2 - \frac{3}{2Pe} \zeta'' - \frac{1}{Pe} \frac{\partial^2 h}{\partial x^2} \right) \\
& + \delta (\theta - 1) \left(\frac{\delta_1}{h} \left(\frac{21}{40} \frac{\partial q}{\partial x} - \frac{21}{40} \frac{q}{h} \frac{\partial h}{\partial x} + \frac{9}{2} \frac{q}{h} \zeta' \right) - \frac{7}{40} \frac{\partial q}{\partial x} \right) \\
& + \delta \frac{q}{20} \zeta' \left(21 \frac{\delta_1}{h} - 27 \right) - \frac{3}{Pe h} (\theta - 1) - 3 \frac{Bi}{Pe} \theta .
\end{aligned} \tag{6.31}$$

Although the equations appear more complicated than the original governing equations, they are useful in analytical and numerical analyses such as calculating the critical Reynolds number over a wavy bottom and conducting transient simulations to compute the development of interfacial waves.

6.3 Steady-State Solutions

The steady-state solutions for the even bottom case can be found from the model equations by setting ζ and all x and t derivatives to zero. From the continuity equation, q is constant, and the scaling for q must be chosen; two logical options exist. If $q_s = 1$ is chosen, the momentum and energy equations give

$$h_s = 1 - \delta_1 + \delta_1^2 + O(\delta_1^3) , \quad \theta_s = \frac{1}{1+Bi} + \frac{Bi}{(1+Bi)^2} \delta_1 - \frac{Bi}{(1+Bi)^3} \delta_1^2 + O(\delta_1^3) . \tag{6.32}$$

Alternatively, q_s can be chosen so that $h_s = 1$; in this case, the steady-state solution for flow over an even bottom is

$$h_s = 1 , \quad q_s = 1 + 3\delta_1 , \quad \theta_s = \frac{1}{1+Bi} . \tag{6.33}$$

The scalings h_s , q_s , and θ_s give the steady-state solutions for flow over an even bottom incline. When bottom topography is included, the steady-state solution for q is given by either $q = 1$ or $q = 1 + 3\delta_1$. The steady-state solutions for h and θ vary with position due to bottom topography; however, the average of these quantities across one bottom wavelength is given by the corresponding scale of the even bottom solution.

The steady-state solution for flow over a wavy bottom is found using the Matlab `bvp4c` algorithm in the same way as the steady-state solutions for the isothermal, impermeable case were found. Because the model includes one additional equation and variable, the setup is slightly different; however, the problem is again re-written as a system of first order differential equations and solved using Matlab's `bvp4c` routine. The steady-state model equations for the problem including heating, permeability, and bottom topography are

$$\begin{aligned}
0 &= \delta^3 h We \left(\zeta''' + \frac{\partial^3 h}{\partial x^3} \right) \\
&+ \frac{\delta^2}{Re} \left(-6q \frac{\partial^2 h}{\partial x^2} - \frac{15}{4} q \zeta'' + \frac{q}{h} \left(4 \left(\frac{\partial h}{\partial x} \right)^2 - 5 (\zeta')^2 - \frac{5}{2} \frac{\partial h}{\partial x} \zeta' \right) \right) \\
&+ \delta^2 h Re Ma \left(\frac{15}{224} h q \frac{\partial^2 \theta}{\partial x^2} + \frac{5}{112} q \frac{\partial \theta}{\partial x} \frac{\partial h}{\partial x} \right) \\
&+ \delta \left(\frac{9}{7} \frac{q^2}{h} \frac{\partial h}{\partial x} - \frac{45}{16} \delta_1 \frac{q^2}{h^2} \zeta' - \frac{5}{2} Ma \frac{\partial \theta}{\partial x} \left(\frac{h}{2} + \delta_1 \right) \right) \\
&+ \delta \left(-\frac{5}{2} \frac{h \cot(\beta)}{Re} \left(\frac{\partial h}{\partial x} + \zeta' \right) (h + 3\delta_1) \right) + \frac{5}{2} \frac{h}{Re} (h + 3\delta_1) - \frac{5}{2} \frac{q}{h Re} , \\
\\
0 &= \delta^2 \left(-\frac{3}{2} \frac{Bi}{Pe} \theta \left(\zeta' + \frac{\partial h}{\partial x} \right)^2 + \frac{3}{40} Ma Re h^2 \left(\frac{\partial \theta}{\partial x} \right)^2 + \frac{h}{Pe} \frac{\partial^2 \theta}{\partial x^2} + \frac{1}{Pe} \frac{\partial \theta}{\partial x} \frac{\partial h}{\partial x} \right) \\
&+ \delta^2 (\theta - 1) \left(\frac{3}{80} Ma Re h \left(h \frac{\partial^2 \theta}{\partial x^2} + 2 \frac{\partial \theta}{\partial x} \frac{\partial h}{\partial x} \right) + \frac{3}{Pe h} \zeta' \frac{\partial h}{\partial x} + \frac{2}{Pe h} \left(\frac{\partial h}{\partial x} \right)^2 - \frac{3}{2Pe} \zeta'' - \frac{1}{Pe} \frac{\partial^2 h}{\partial x^2} \right) \\
&+ \delta (\theta - 1) \frac{\delta_1}{h} \left(-\frac{21}{40} \frac{q}{h} \frac{\partial h}{\partial x} + \frac{9}{2} \frac{q}{h} \zeta' \right) \\
&+ \delta \frac{q}{20} \zeta' \left(21 \frac{\delta_1}{h} - 27 \right) - \frac{3}{Pe h} (\theta - 1) - 3 \frac{Bi}{Pe} \theta .
\end{aligned} \tag{6.34}$$

Steady-state solutions over one bottom wavelength show the effect on fluid layer thickness and interface temperature of bottom heating and permeability in figures 6.2 and 6.3. All parameters are kept constant except the permeability parameter and the Biot and Marangoni numbers, which are varied to show the effect of heating and permeability.

Figure 6.2 shows the steady-state solutions for the scaling when $q_s = 1$. The top panel shows that adding bottom porosity reduces the fluid layer thickness. This occurs because the velocity throughout the fluid layer is increased due to the bottom slip velocity, and since the volume flow rate remains constant, the fluid height must decrease. The second panel shows that adding heating has very little effect on the fluid layer thickness; adding heating to the case with porosity similarly has little effect on the fluid layer thickness.

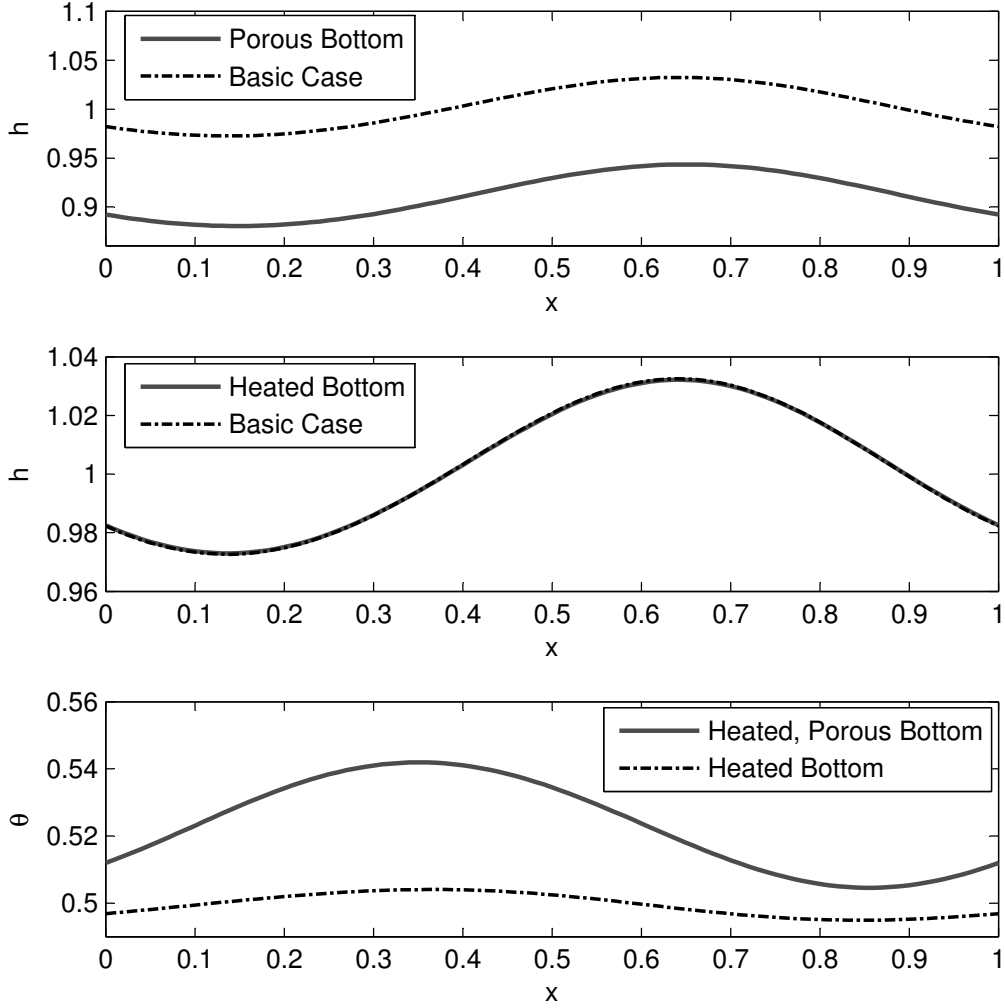


Figure 6.2: Fluid thickness h and interface temperature θ over one bottom wavelength for $a_b = 0.1$, $\delta = 0.1$, $\cot \beta = 1$, $We = 5$, and $Re = 1$; for cases with porosity, $\delta_1 = 0.1$, and for cases with heating, $Bi = Ma = 1$. The scaling $q_s = 1$ is used.

Finally, in the bottom panel, it is shown that adding bottom permeability increases the magnitude and variation in the surface temperature. The increase in magnitude is due to the thinner fluid layer, which brings the interface closer to the heated bottom surface.

Figure 6.3 compares steady-state solutions using the scaling $h_s = 1$. The top panel shows the effect of adding porosity on fluid layer thickness, which is to increase the overall variation; this occurs because the fluid can cross the bottom boundary, and tends to flow into the boundary near the minimum of the fluid layer thickness, and out of the bottom boundary near the maximum of the fluid layer thickness, thus exaggerating these extremes. This also explains why the temperature variation is greater for the porous bottom case, shown in the bottom panel of both figures 6.2 and 6.3. Since bottom porosity increases the variation of fluid layer thickness, the interface temperature will also vary more across one bottom wavelength. As with the other scaling, the second panel of figure 6.3 also shows that adding heating has a negligible effect on the fluid layer thickness.

Figure 6.4 and 6.5 show the effect of permeability on the alignment of the peaks and troughs of the fluid layer thickness and interface temperature. If the fluid were stationary, the interface temperature would be greatest where the fluid layer is thinnest because this is where the interface is closest to the heated bottom. Similarly, the interface temperature would be lowest at a peak in fluid layer thickness. Due to the movement of the fluid, the curves are shifted slightly so that the peak in interface temperature occurs slightly after the trough in fluid thickness, as seen in figure 6.4. Adding permeability, however, shifts the interface temperature curve even more, resulting in a greater gap between the point at which the fluid layer is thickest and the point at which the interface temperature is smallest, as seen in figure 6.5. In this case, the gap increases by about 0.12 bottom wavelengths. This is also seen in the numerical solutions of the model equations, shown in section 6.6.

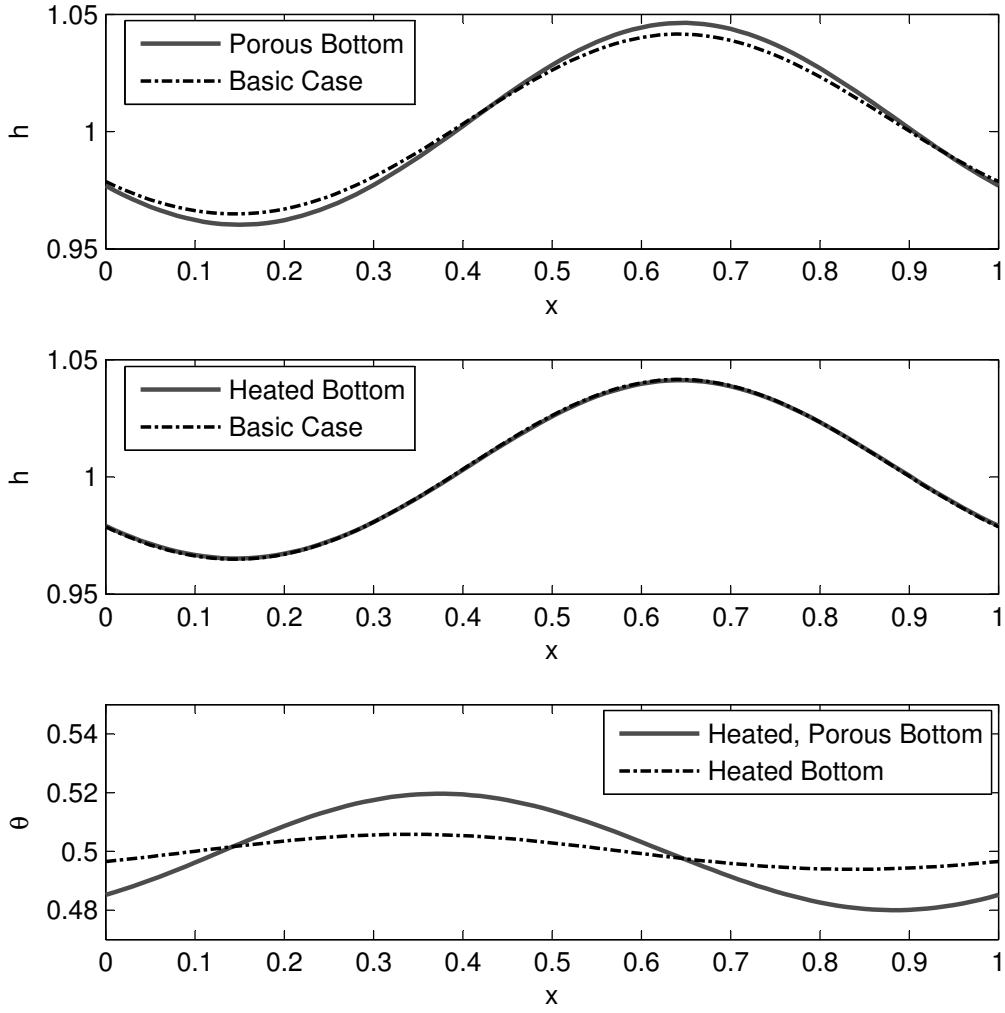


Figure 6.3: Fluid thickness h and interface temperature θ over one bottom wavelength for $a_b = 0.1$, $\delta = 0.1$, $\cot \beta = 1$, $We = 5$, $Bi = Ma = 1$, and $Re = 1$; for cases with porosity, $\delta_1 = 0.1$. The scaling $h_s = 1$ is used.

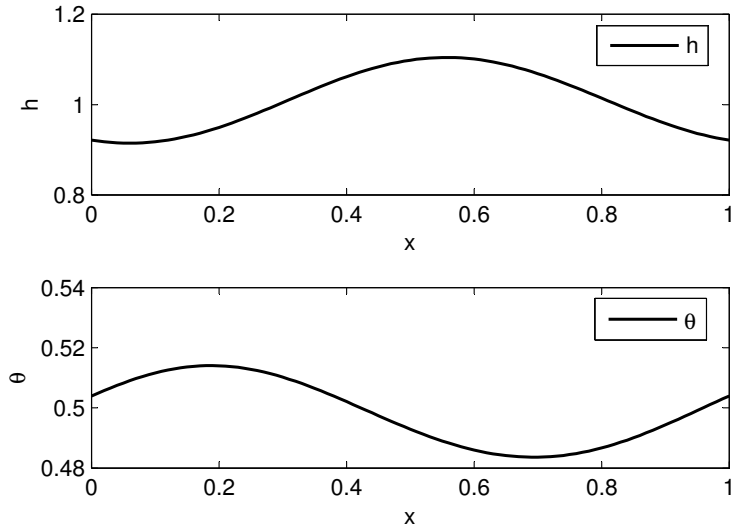


Figure 6.4: Fluid layer thickness and interface temperature over one bottom wavelength for $a_b = 0.1$, $\delta = 0.1$, $\cot \beta = 1$, $We = 100$, $Bi = Ma = 1$, $Re = 1$, and $\delta_1 = 0$.

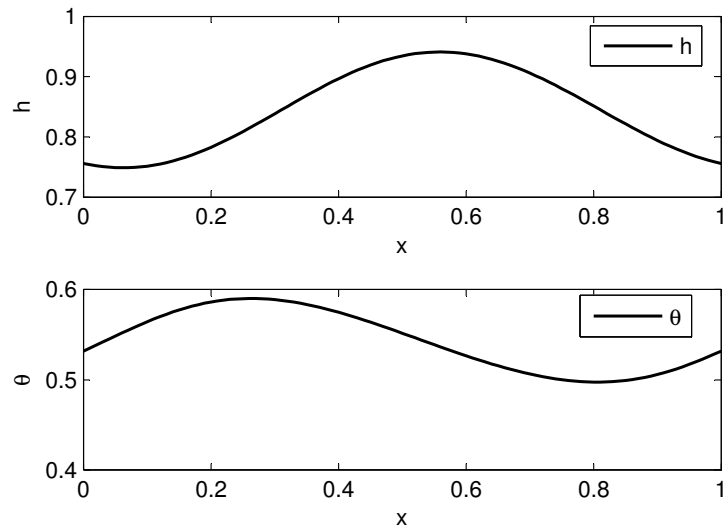


Figure 6.5: Fluid layer thickness and interface temperature over one bottom wavelength for $a_b = 0.1$, $\delta = 0.1$, $\cot \beta = 1$, $We = 100$, $Bi = Ma = 1$, $Re = 1$, and $\delta_1 = 0.2$. The scaling $q_s = 1$ is used.

6.4 Linear Stability with an Even Bottom

The linear stability analysis for determining the critical Reynolds number for the even bottom problem with both bottom heating and permeability is approached using two different methods. First, the Benney equation is developed, and a linear stability analysis is performed on the resulting equation. An alternative stability method making use of the WRM equations is also employed. The results from the two methods are compared to each other and to the results obtained by Sadiq et al. [4]. From these comparisons, the performance of the weighted residual model can be assessed. The expressions for the critical Reynolds number are also used to determine the effect of heating and bottom permeability on the stability of the flow.

6.4.1 Linear Stability using the Benney Equation

To develop the Benney equation, the governing equations and boundary conditions are used directly. Each of the primitive variables, u , w , p , and T , is expanded in a perturbation series about the shallowness parameter δ , as shown below:

$$\begin{aligned}u &= u_0 + \delta u_1 + O(\delta^2) , \\w &= w_0 + \delta w_1 + O(\delta^2) , \\p &= p_0 + \delta p_1 + O(\delta^2) , \\T &= T_0 + \delta T_1 + O(\delta^2) .\end{aligned}\tag{6.35}$$

By substituting these expansions into the governing equations and the dynamic and bottom boundary conditions, problems at each order of δ can be formulated. The solutions from the $O(1)$ and $O(\delta)$ problems are used in the derivation of the Benney equation; the $O(1)$ problem is solved below. The governing equations at leading order are

$$\begin{aligned}\frac{\partial u_0}{\partial x} + \frac{\partial w_0}{\partial z} &= 0 , \\3 + \frac{\partial^2 u_0}{\partial z^2} &= 0 , \\Re \frac{\partial p_0}{\partial z} + 3 \cot \beta &= 0 , \\\frac{\partial^2 T_0}{\partial z^2} &= 0 .\end{aligned}\tag{6.36}$$

The dynamic condition at the free surface gives

$$\left. \begin{aligned} p_0 &= 0 \\ \frac{\partial u_0}{\partial z} &= 0 \end{aligned} \right\} \text{ at } z = 1 + \zeta , \quad (6.37)$$

and the free surface heat transfer condition gives

$$\frac{\partial T_0}{\partial z} = -BiT_0 \text{ at } z = 1 + \zeta . \quad (6.38)$$

Finally, the bottom boundary conditions are

$$\left. \begin{aligned} w_0 &= \zeta' u_0 \\ u_0 &= \delta_1 \frac{\partial u_0}{\partial z} \\ T_0 &= 1 \end{aligned} \right\} \text{ at } z = \zeta . \quad (6.39)$$

Equations (6.36) to (6.39) can be solved to find u_0 , w_0 , p_0 , and T_0 . The solutions are

$$\begin{aligned} u_0 &= \frac{-3}{2}(z^2 + \zeta^2) + 3z(h + \zeta) - 3h\zeta + 3h\delta_1 , \\ w_0 &= \frac{-3}{2} \left(\zeta' + \frac{\partial h}{\partial x} \right) (z - \zeta)^2 + 3 \left(\zeta' h - \delta_1 \frac{\partial h}{\partial x} \right) (z - \zeta) + 3\zeta' h \delta_1 , \\ p_0 &= \frac{3 \cot \beta}{Re} (z - \zeta - h) , \\ T_0 &= 1 + (\zeta - z) \frac{Bi}{1+hBi} . \end{aligned} \quad (6.40)$$

The $O(\delta)$ problem is then considered, and u_1 and w_1 are found. The $\frac{\partial h}{\partial t}$ terms from u_1 and w_1 are eliminated using the $O(1)$ kinematic condition. The following Benney equation is then obtained from the kinematic condition at $O(\delta)$:

$$\frac{\partial h}{\partial t} = w_0 - (u_0 + \delta u_1) \left[\frac{\partial h}{\partial x} + \frac{d\zeta}{dx} \right] + \delta w_1 . \quad (6.41)$$

The final Benney equation for the even bottom problem including both heating and bottom permeability is

$$\begin{aligned} \frac{\partial h}{\partial t} + 6\delta_1 h \frac{\partial h}{\partial x} + \frac{\partial h^3}{\partial x} + \delta \frac{\partial}{\partial x} \left(\frac{6}{5} Re \left(h^6 \frac{\partial h}{\partial x} + 6\delta_1 h^5 \frac{\partial h}{\partial x} + \frac{25}{2} \delta_1^2 h^4 \frac{\partial h}{\partial x} \right) \right) \\ + \delta \frac{\partial}{\partial x} \left(\frac{Ma Re Bi}{(1+hBi)^2} h \frac{\partial h}{\partial x} \left(\frac{h}{2} + \delta_1 \right) - \cot \beta (3\delta_1 h^2 + h^3) \frac{\partial h}{\partial x} \right) = 0 \end{aligned} \quad (6.42)$$

The Benney equation is an evolution equation for the fluid layer thickness, $h(x, t)$. It is valid when the flow is close to the steady-state. Therefore, it accurately describes the flow for a short time after the flow destabilizes, and can thus be used to find the Reynolds number at which the flow becomes unstable. To find the critical Reynolds number for the flow, a linear stability analysis is performed on the Benney equation. The fluid thickness h is perturbed about the steady-state value as follows: $h = h_s + \hat{h}$, and the perturbation, \hat{h} , is assumed to have the form, $\hat{h} = h_0 e^{ik(x-ct)}$. This is substituted into the Benney equation, which is then linearized in the perturbation. The critical Reynolds number is found by requiring that $\Im(c) = 0$. This leads to

$$Re_{crit}^{Ben} = \frac{5}{6} \cot \beta \frac{3\delta_1 h_s^2 + h_s^3}{h_s^6 + 6\delta_1 h_s^5 + \frac{25}{2} \delta_1^2 h_s^4 + \frac{5}{6} \frac{MaBi}{(1+h_s Bi)^2} h_s \left(\frac{h_s}{2} + \delta_1 \right)}. \quad (6.43)$$

For the scaling $q_s = 1$, the expression is

$$Re_{crit}^{Ben} = \frac{5}{6} \cot \beta \frac{1}{1 + \frac{5}{12} \frac{MaBi}{(1+Bi(1-\delta_1+\delta_1^2))^2} (\delta_1^2+1) + \frac{7}{2} \delta_1^2}, \quad (6.44)$$

while for the scaling $h_s = 1$, the critical Reynolds number is given by

$$Re_{crit}^{Ben} = \frac{5}{6} \cot \beta \frac{1+3\delta_1}{1+6\delta_1 + \frac{25}{2} \delta_1^2 + \frac{5}{12} \frac{MaBi}{(1+Bi)^2} (1+2\delta_1)}. \quad (6.45)$$

This result has a similar form to equation (2.42), which gives the critical Reynolds number for flow over an isothermal, impermeable surface. Further, this expression accounts for the influence of permeability through the parameter δ_1 , and heating through the parameters Bi and Ma . It can be seen from equation (6.43) that both heating and permeability individually cause the critical Reynolds number to fall below the value of $\frac{5}{6} \cot \beta$, and hence destabilize the flow. Also, the combined effect of heating and permeability is to further destabilize the flow; this can be seen from the term in the denominator in which the heating and permeability parameters multiply each other. This term further decreases the critical Reynolds number of the flow.

6.4.2 Linear Stability using the Model Equations

An alternative method for determining the critical Reynolds number, which takes advantage of the WRM equations, was also carried out. Each variable in the model equations,

h , q , and θ , are perturbed about the steady-state value as follows:

$$q = q_s + q_0 e^{ik(x-ct)}, \quad (6.46)$$

$$h = h_s + h_0 e^{ik(x-ct)}, \quad (6.47)$$

$$\theta = \theta_s + \theta_0 e^{ik(x-ct)}. \quad (6.48)$$

The variables are substituted into the model equations, which are then linearized in the perturbations. The three equations are then combined to yield a dispersion equation involving c and k . For neutral stability, the phase speed is set to $c = s + 0i$ where s , the phase speed of the disturbances, is given by $s = 3h_s(h_s + 2\delta_1)$. The phase speed is close to three, which is the value for isothermal impermeable flow; however, it is modified slightly to account for permeability. The critical Reynolds number can then be found and is given by

$$Re_{crit}^{WRM} = \frac{5}{6} \cot \beta \frac{h_s^2(h_s + 3\delta_1)}{h_s^3(h_s + 2\delta_1)^3 + \frac{1}{7}q_s^2 - \frac{17}{7}h_s(h_s + 2\delta_1)(h_s + \delta_1)q_s + \frac{5}{12} \frac{MaBi(h_s + 2\delta_1)}{1 + h_s Bi} h_s \theta_s}. \quad (6.49)$$

For the scaling $q_s = 1$, the critical Reynolds number is

$$Re_{crit}^{WRM} = \frac{5}{6} \cot \beta \frac{1}{1 + \frac{5}{12} \frac{MaBi}{(1+Bi)^2} \left(1 + \frac{2Bi}{1+Bi} \delta_1 + \frac{1+2Bi^2}{(1+Bi)^2} \delta_1^2 \right) + \frac{29}{7} \delta_1^2}, \quad (6.50)$$

while for the scaling $h_s = 1$, the critical Reynolds number is

$$Re_{crit}^{WRM} = \frac{5}{6} \cot \beta \frac{1+3\delta_1}{1+6\delta_1 + \frac{92}{7} \delta_1^2 + \frac{5}{12} \frac{MaBi(1+2\delta_1)}{(1+Bi)^2}}. \quad (6.51)$$

The critical Reynolds number obtained using this method is again of a similar form to equation (2.42), with a correction term to account for heating and permeability. It is also very similar to the expression for the critical Reynolds number obtained using the Benney approach; the terms agree to $O(\delta_1)$, where δ_1 is assumed to be a small parameter.

6.4.3 Comparison of Linear Stability Results

The expressions for the critical Reynolds number obtained from the two methods can be compared to theoretical values for various limiting cases. This is done in table 6.1. The theoretical values have been obtained from perturbation expansion solutions of the Orr-Sommerfeld equation from previously published studies. The scaling $h_s = 1$ is used for the case with permeability because the theoretical results were found using this scaling [4, 26]. The table shows that in the isothermal, impermeable limit, both the Benney method and the weighted residual model stability method reproduce the theoretical result. Also, both

Table 6.1: Comparison of critical Reynolds number for limiting cases to Orr-Sommerfeld result

Limiting Case	Re_{crit}^{WRM}	Re_{crit}^{Ben}	Re_{crit}^{Theor}
Isothermal and Impermeable $Bi = Ma = \delta_1 = 0$	$\frac{5}{6} \cot \beta$	$\frac{5}{6} \cot \beta$	$\frac{5}{6} \cot \beta$ [1, 2]
Impermeable $\delta_1 = 0$	$\frac{5}{6} \cot \beta \frac{1}{1 + \frac{5}{12} \frac{MaBi}{(1+Bi)^2}}$	$\frac{5}{6} \cot \beta \frac{1}{1 + \frac{5}{12} \frac{MaBi}{(1+Bi)^2}}$	$\frac{5}{6} \cot \beta \frac{1}{1 + \frac{5}{12} \frac{MaBi}{(1+Bi)^2}}$ [7]
Isothermal $Bi = Ma = 0$	$\frac{5}{6} \cot \beta \frac{1+3\delta_1}{1+6\delta_1 + \frac{92}{7}\delta_1^2}$	$\frac{5}{6} \cot \beta \frac{1+3\delta_1}{1+6\delta_1 + \frac{25}{2}\delta_1^2}$	$\frac{5}{6} \cot \beta \frac{1+3\delta_1}{1+6\delta_1 + \frac{25}{2}\delta_1^2}$ [8, 26]

methods give the theoretical result in the impermeable limit. In the isothermal limit, the Benney method gives the same result as that found by Pascal [26] and by Sadiq et al. [4] from the Orr-Sommerfeld equation; this is expected since both methods derive the result from the governing equations and boundary conditions, without making the assumptions used to derive the model. However, the weighted residual model stability method differs slightly at $O(\delta_1^2)$. All methods agree to $O(\delta_1)$ where δ_1 is a small parameter, so the difference is small, indicating that the weighted residual model predicts the critical Reynolds number reasonably well. For the combined thermal and permeable case, the weighted residual model stability method and the Benney methods also agree with the Orr-Sommerfeld result to $O(\delta_1)$, although this is not listed in the table.

Sadiq et al. [4] also consider the problem with both heating and permeability, and find the following expression for the critical Reynolds number:

$$Re_{crit}^{Sad} = \frac{5}{6} \cot \beta \frac{(1+3\delta_1)}{1+6\delta_1 + \frac{25}{2}\delta_1^2 + \frac{15}{2}\delta_1^3 + \frac{5}{12} \frac{1+2\delta_1}{(1+Bi)^2} MaBi} . \quad (6.52)$$

They derive this result from a perturbation solution to the Orr-Sommerfeld equation and use the scaling $h_s = 1$. This expression also matches equations (6.45) and (6.51) to $O(\delta_1)$, indicating that the weighted residual model is able to predict the critical Reynolds number with the combined effects of heating and bottom permeability to second-order. This level of agreement is to be expected since the WRM is a second-order model.

6.4.4 Effect of Heating and Porosity on Stability

The effects of heating and permeability on the critical Reynolds number are illustrated in figures 6.6 to 6.9. Plotted in the diagrams are the critical Reynolds numbers using the scaling $q_s = 1$ as obtained from equations (6.44) and (6.50). Figure 6.6 shows how increasing

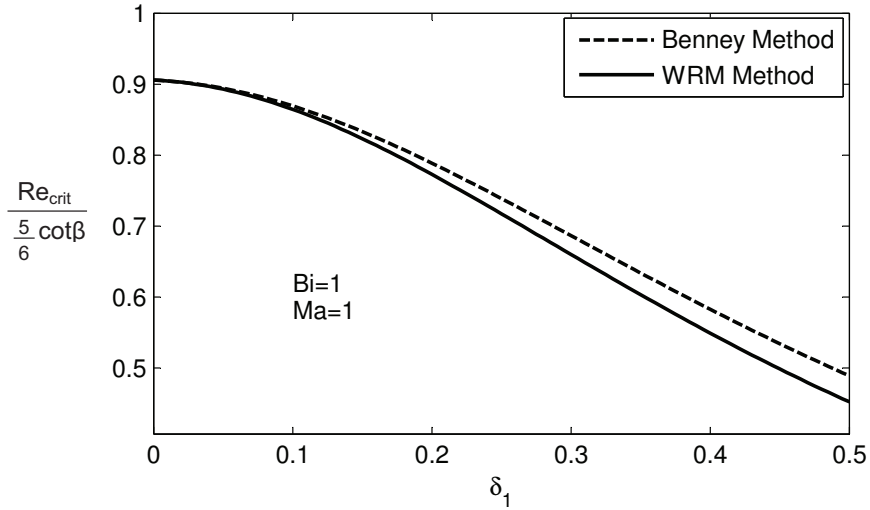


Figure 6.6: Effect of increasing δ_1 on the critical Reynolds number.

the permeability of the bottom surface affects the critical Reynolds number. The curves correspond to a case with bottom heating, although the same trend would be observed for other values of the Biot and Marangoni number, as well as for the isothermal case. The plot reveals that increasing the permeability of the bottom destabilizes the flow and hence decreases the critical Reynolds number. Increasing the permeability allows for slip along the bottom and therefore increases the overall velocity and volume flow rate; an increased volume flow rate has the opposite effect of the decreased volume flow rate discussed in section 5.2, and the flow is therefore destabilized.

It can be seen from figure 6.7 that increasing the Marangoni number also decreases the critical Reynolds number. The Marangoni number measures the variation in surface tension due to the temperature difference between the bottom surface and the surroundings. This result indicates that heating causes a variation in surface tension, which results in a less stable flow. The variation in surface tension causes fluid to be drawn to areas of higher surface tension. Since surface tension increases with decreasing temperature, the peaks of the disturbances will have higher surface tension since they are further from the bottom. Hence fluid is drawn toward the peaks, causing the disturbances to grow and therefore destabilizing the flow.

Figure 6.8 shows how the critical Reynolds number changes when the Biot and Marangoni numbers are varied simultaneously. Again, it shows that increasing these two parameters together destabilizes the flow. Figure 6.9 shows how varying the Biot number, while holding

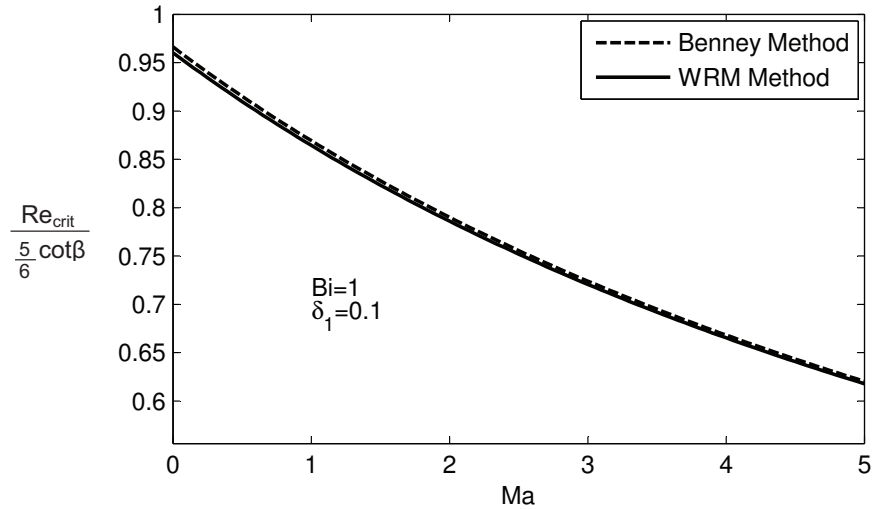


Figure 6.7: Effect of increasing Ma on the critical Reynolds number.

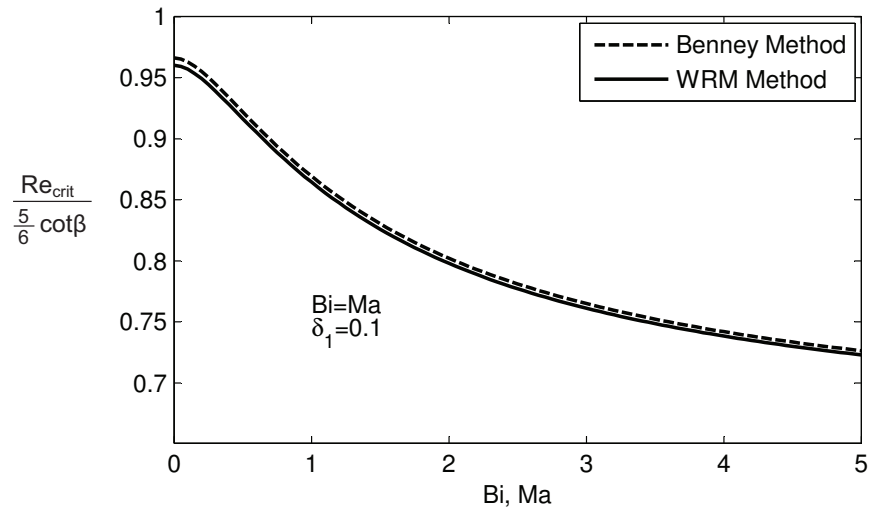


Figure 6.8: Effect of increasing Ma and Bi together on the critical Reynolds number.

the Marangoni number and permeability parameter constant, affects the stability of the flow. In this case, there is a specific Biot number at which the flow is most unstable; increasing the Biot number from zero to that value destabilizes the flow, but increasing it beyond that value brings the critical Reynolds number closer to the isothermal limit.

The effect of heating and permeability on the stability of the flow can also be realized

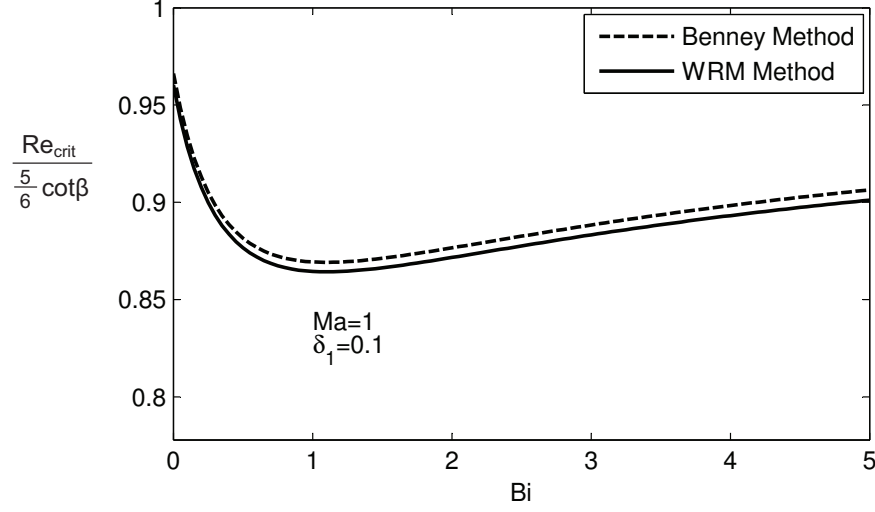


Figure 6.9: Effect of increasing Bi on the critical Reynolds number.

by differentiating the expression for the critical Reynolds number with respect to the parameters. Since

$$\frac{\partial Re_{cr}}{\partial Ma} = -\frac{5}{12} \frac{Bi(\delta_1^2+1)}{\left(1 + \frac{5}{12} \frac{MaBi(\delta_1^2+1)}{(1+Bi(1-\delta_1^2+\delta_1^2))^2 + \frac{7}{2}\delta_1^2}\right)^2 (1+Bi(1-\delta_1^2+\delta_1^2))^2} < 0, \quad (6.53)$$

increasing the Marangoni number clearly decreases the critical Reynolds number. Similarly,

$$\frac{\partial Re_{cr}}{\partial \delta_1} = -\frac{\frac{5}{6} \frac{MaBi\delta_1}{(1+Bi(1-\delta_1^2+\delta_1^2))^2} - \frac{5}{6} \frac{MaBi^2(\delta_1^2+1)(2\delta_1-1)}{(1+Bi(1-\delta_1^2+\delta_1^2))^3} + 7\delta_1}{\left(1 + \frac{5}{12} \frac{MaBi(\delta_1^2+1)}{(1+Bi(1-\delta_1^2+\delta_1^2))^2 + \frac{7}{2}\delta_1^2}\right)^2} < 0, \quad (6.54)$$

provided $\delta_1 < 0.5$; because δ_1 is assumed to be small and of order δ , this is expected to hold. Considering changes in the Biot number, however, it is easily shown that, for equation (6.50),

$$\frac{\partial Re_{cr}}{\partial Bi} = 0 \text{ when } Bi = \frac{1}{1-\delta_1+\delta_1^2}. \quad (6.55)$$

This agrees with figure 6.9, which shows a minimum occurring near $Bi = 1$.

The critical Reynolds number is a minimum for a Biot number near one because the interface temperature changes the most with changes in fluid layer thickness for that value. When the Biot number is much less than one, the interface temperature is very close to the bottom surface temperature; therefore, changes in fluid layer thickness result in small

interface temperature variations. When the Biot number is much larger than one, the interface temperature is close to the ambient temperature, and again, changes in the fluid layer thickness cause only small changes in the interface temperature. Thus, in both of these cases, the surface tension variation is small, and the destabilizing Marangoni effect is minimized. However, for a Biot number near one, the temperature variation is largest, so the surface tension also varies the most along the interface, and the Marangoni effect is most pronounced.

6.5 Linear Stability with Bottom Topography

The method for determining the critical Reynolds number for flow over a wavy bottom described in section 5.1.4 is used here to calculate neutral stability curves for various sets of parameters. Because heating and permeability are included, a slightly different set of equations are used; more details on the application of Floquet theory for the linear stability analysis of flow over a wavy inclined plane with heating and bottom permeability can be found in Appendix A. Figures 6.10 to 6.15 show the effect of varying the flow parameters on the neutral stability curve with the scaling $q_s = 1$. The neutral stability curves are plotted as K , the Bloch wavenumber, versus Re , the Reynolds number. Here, the Bloch wavenumber is used because Floquet theory is required to deal with the bottom waviness, and it represents the wavenumber of the perturbation.

In figure 6.10, neutral stability curves are shown for various angles of inclination, for three bottom amplitudes. The curves show that decreasing the angle of inclination, which corresponds to increasing $\cot \beta$, increases the critical Reynolds number, and shifts the entire curve to the right, toward higher Reynolds numbers. This is expected based on the expression for the critical Reynolds number for an even bottom, $Re_{cr}^{even} = \frac{5}{6} \cot \beta$. Furthermore, increasing $\cot \beta$, combined with a large bottom amplitude, changes the shape of the neutral stability curve, as seen in the bottom two panels of the figure. The critical Reynolds number is shifted from the long-wave limit up to a non-zero wavenumber, resulting in shorter waves being the most unstable. This is most pronounced in the curve corresponding to $\cot \beta = 5$ in the bottom panel of figure 6.10; here the critical Reynolds number occurs for a perturbation having a wavelength approximately equal to twice the bottom wavelength, which is equal to one.

The effect of bottom topography is shown in figure 6.11, in which the curves from figure 6.10 are arranged to highlight the impact of varying the bottom topography. It can be seen that for each of the inclinations shown, increasing the bottom amplitude stabilizes the flow by shifting the curve to the right and therefore increasing the critical Reynolds

number. The plots also show how increasing both the bottom amplitude and $\cot \beta$ changes the shape of the curve, as mentioned above.

The combined effect of surface tension and bottom topography on the stability of the flow is shown in figure 6.12. Shown in the top panel is a case with an even bottom; it is clear that surface tension does not affect the critical Reynolds number in the absence of bottom topography. However, the shape of the neutral stability curve is altered when surface tension is increased; for shorter wavelengths, the flow becomes stable as surface tension is increased. The two cases with bottom topography show that increasing the surface tension from $We = 5$ to $We = 10$ shifts the neutral stability curve to the right, which increases the critical Reynolds number and stabilizes the flow. This agrees with the predictions of the asymptotic analysis discussed in section 5.2, which indicated that when bottom topography and weak surface tension are combined, the flow rate is decreased and therefore the flow is stabilized. However, further increasing the surface tension actually reverses the combined effect of bottom topography and surface tension and thus destabilizes the flow. This result is consistent with the reversal in stability reported by D'Alessio et al. [13].

Figure 6.13 shows the effect of increasing the shallowness parameter δ , or increasing the fluid thickness relative to the characteristic length of the bottom topography. Results are shown for two different values of bottom amplitude. The even bottomed case is not shown because the shallowness parameter, δ , is arbitrary for the even bottomed case; the neutral stability curve should be plotted as $k\delta$ versus Re in this case, as seen in the earlier comparisons to the experimental data. For both amplitudes shown in the figure, increasing the thickness relative to the bottom wavelength stabilizes the flow; that is, bottom topography having a shorter wavelength stabilizes the flow compared to that having a longer bottom wavelength. However, it must be remembered that the underlying assumption that $\delta \ll 1$ puts a restriction on the bottom wavelength allowed; it requires that the bottom wavelength must be long compared to the fluid layer thickness.

The effect of bottom permeability on the stability of the flow is shown in figure 6.14. Two cases are shown: one with heating in the top panel, and one without heating in the bottom panel. In each case, the neutral stability curves with and without permeability are both shown, and in each case, it can be seen that adding permeability decreases the critical Reynolds number and thus destabilizes the flow. Adding permeability also changes the shape of the neutral stability curve by increasing the wavenumber corresponding to the most unstable disturbance.

Finally, the effect of bottom heating on the stability of the flow is shown in figure 6.15. Two sets of neutral stability curves are shown; in the top panel, the bottom topography

characterized by $a_b = 0.3$ is used, and in the bottom panel, the bottom topography is described by $a_b = 0.4$. The curves show that increasing heating while holding other parameters constant destabilizes the flow, even when bottom topography is included. Also, varying the Marangoni number can alter the value of the most unstable wavenumber, as seen in the top panel of figure 6.15. For flows with a large bottom amplitude and a small angle of inclination, the the shape of the curve can change such that the critical Reynolds number occurs for a non-zero wavenumber, as seen in figure 6.10. Increasing the Marangoni number, however, causes the shape of the curve to take on a form similar to that observed when the bottom amplitude is small; thus the critical Reynolds number can occur for a perturbation wavenumber of zero if the Marangoni number is sufficiently large, as seen in figure 6.15.

The neutral stability curves for flow over a wavy bottom show that most of the trends seen for an even bottom persist when bottom topography is added. The exception is that bottom waviness can change the wavenumber of the most unstable perturbations. Further, the plots confirm that adding bottom topography and weak surface tension stabilizes the flow, while the combination of strong surface tension and bottom topography destabilizes the flow.

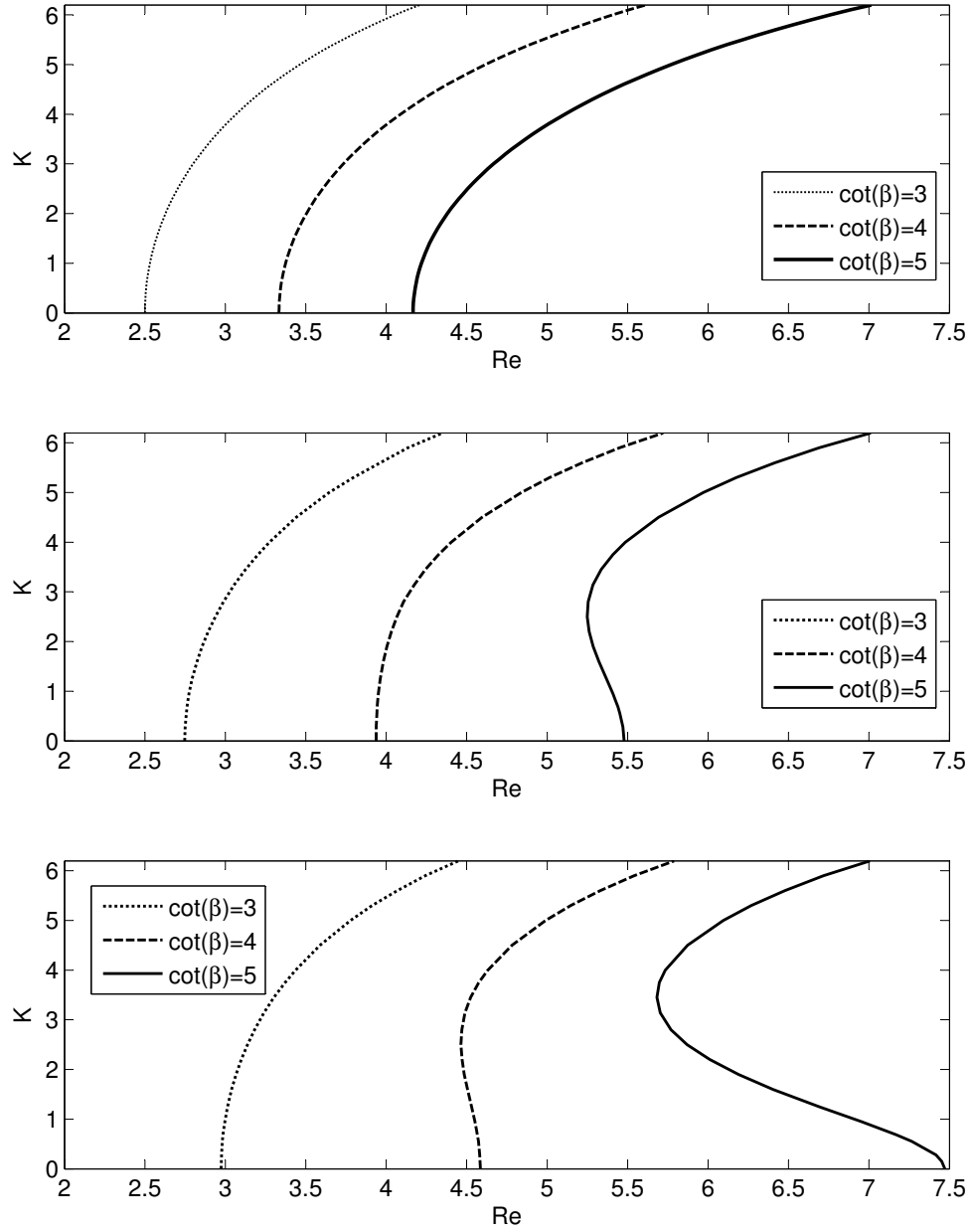


Figure 6.10: Effect of increasing $\cot \beta$ for the isothermal, impermeable case where $\delta = 0.05$ and $W\dot{e} = 5$, with even bottom (top), $a_b = 0.3$ (middle), and $a_b = 0.4$ (bottom).

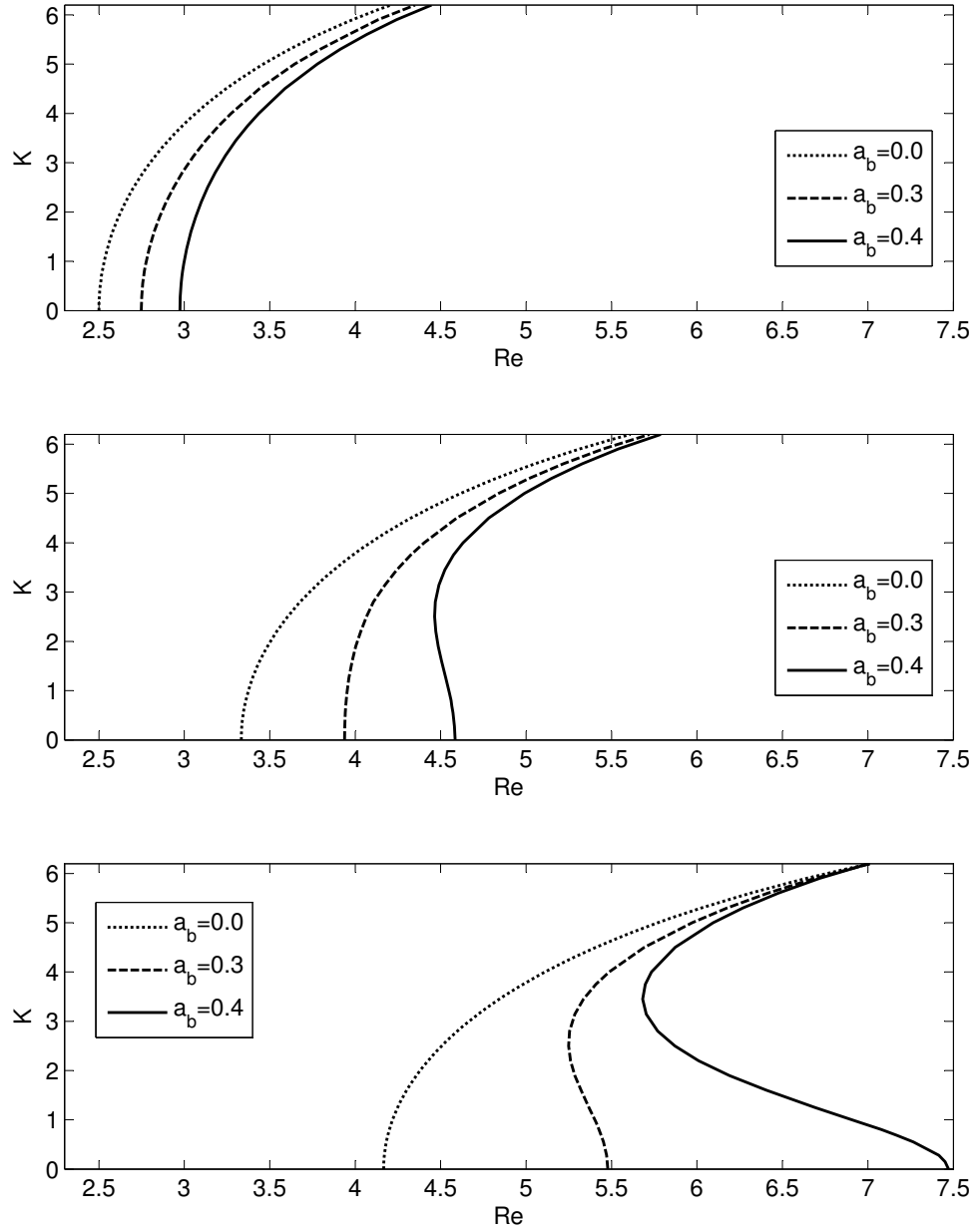


Figure 6.11: Effect of increasing a_b for the isothermal, impermeable case where $\delta = 0.05$ and $\tilde{We} = 5$, with $\cot \beta = 3$ (top), $\cot \beta = 4$ (middle), and $\cot \beta = 5$ (bottom).

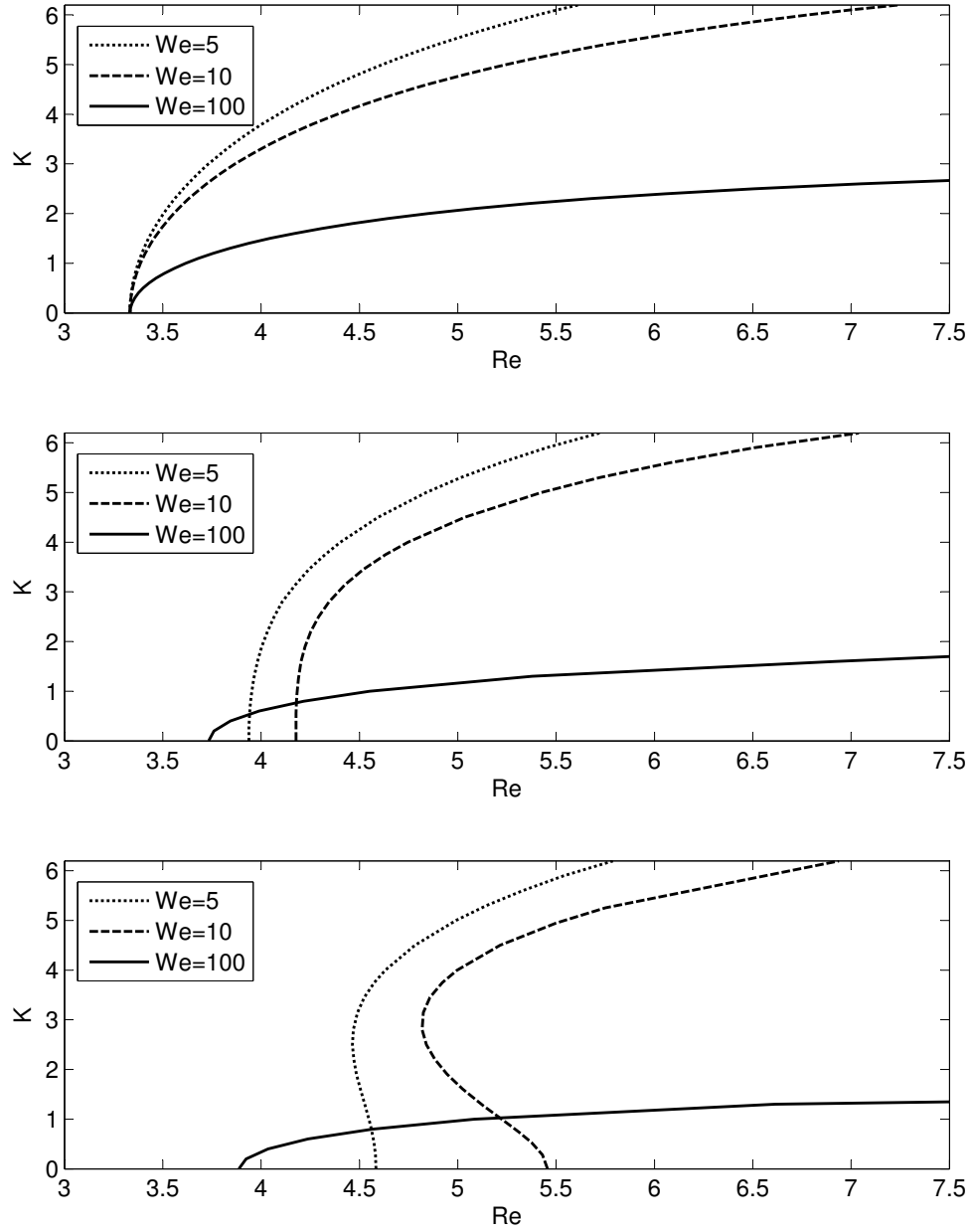


Figure 6.12: Effect of increasing We for the isothermal, impermeable case where $\delta = 0.05$ and $\cot \beta = 4$, with $a_b = 0.0$ (top), $a_b = 0.3$ (middle), and $a_b = 0.4$ (bottom).

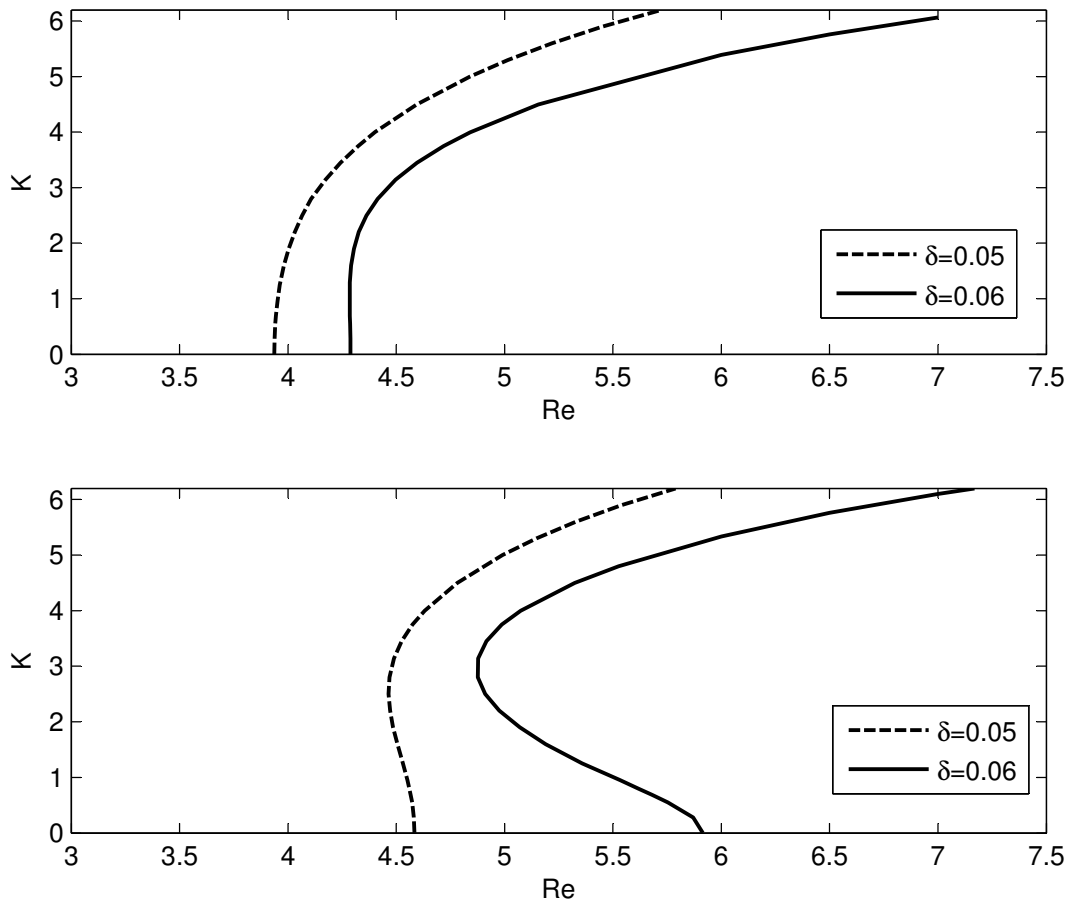


Figure 6.13: Effect of increasing δ for the isothermal, impermeable case where $We = 5$ and $\cot \beta = 4$, with $a_b = 0.3$ (top), and $a_b = 0.4$ (bottom).

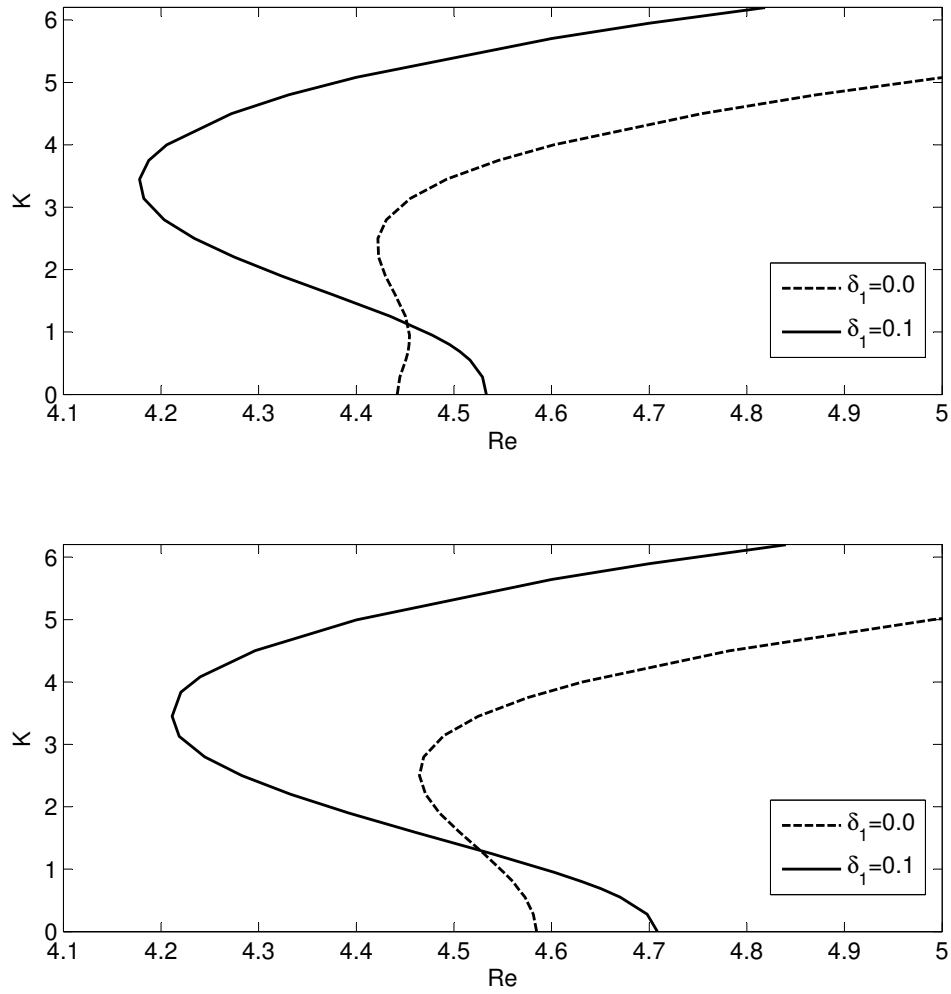


Figure 6.14: Effect of increasing δ_1 for the case where $\delta = 0.05$, $We = 5$, $a_b = 0.4$, $\cot \beta = 4$, $Pr = 7$, and $Bi = 1$, with $Ma = 0.2$, (top) and $Ma = 0$, (bottom).

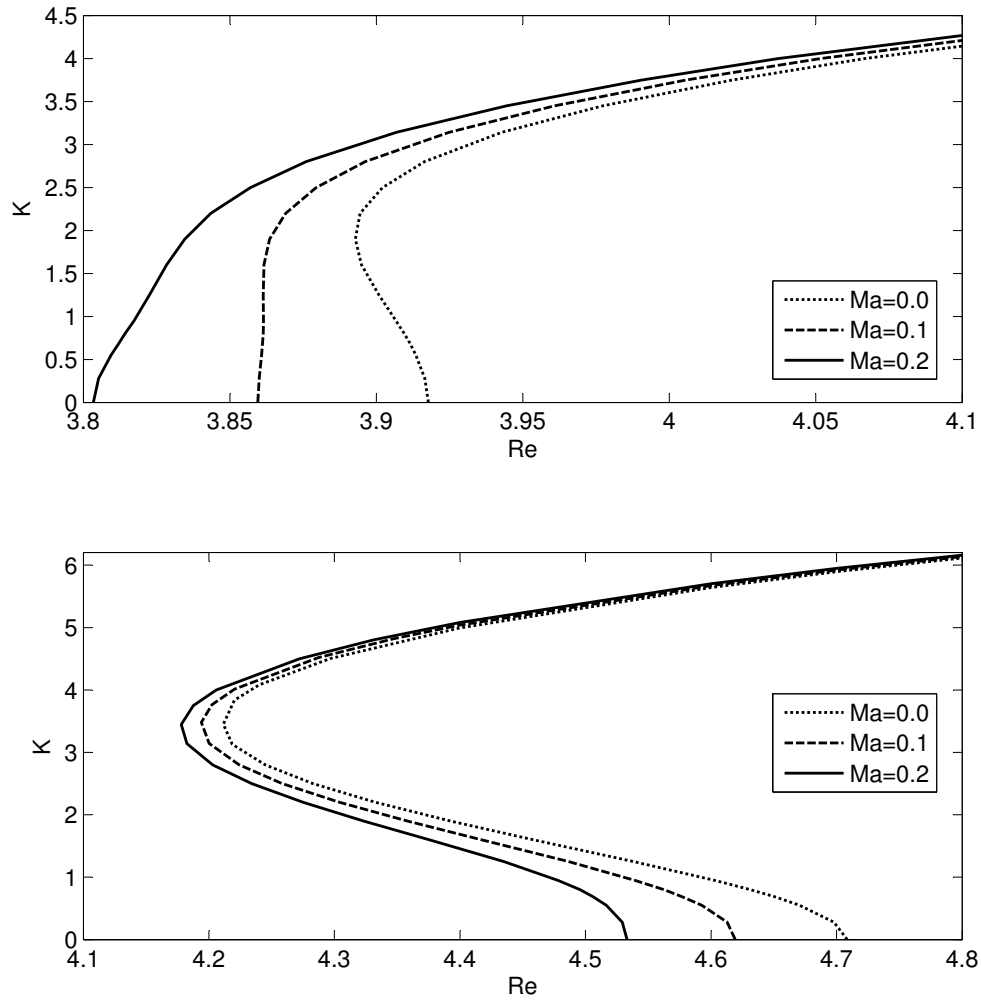


Figure 6.15: Effect of increasing Ma for the case where $\delta = 0.05$, $We = 5$, $\cot \beta = 4$, $Pr = 7$, $Bi = 1$, and $\delta_1 = 0.1$, with $a_b = 0.3$, (top) and $a_b = 0.4$, (bottom).

6.6 Numerical Simulation Results

The weighted residual model including heating and permeability is solved numerically using the fractional step method in a similar manner as described in section 4.1. The main difference is in the inclusion of the energy equation. The development of the interface with time is shown for one case in figure 6.16. The case includes bottom topography, surface tension and heating. A perturbation with a wavelength equal to the length of the domain is initially imposed; because the flow is unstable, the perturbation grows into a wave that eventually maintains its shape and continuously cycles through the domain.

The fully developed results for the same case are compared to results for the corresponding isothermal, impermeable case in figure 6.17. The two simulations are started with the steady-state solutions as the initial conditions. The resulting fully-developed volume flow rate, height, and interface temperature along the domain are shown in the figure with the scaling $q_s = 1$. The volume flow rate, shown in the top panel, indicates that the wave formed for the thermal permeable case is slightly more pronounced than that for the isothermal impermeable case. This is to be expected since it has already been shown that, in general, heating and permeability tend to destabilize the flow. The wave is also more pronounced due to the variation in surface tension; the surface tension is greater when the fluid temperature is lower and is therefore greatest at the peak of the wave. Fluid tends to be drawn to areas of higher surface tension, increasing the height of the wave.

The middle panel shows the fluid layer thickness. Near the middle of the domain, away from the q -waves in the panel above, the fluid layer thickness is greater for the isothermal impermeable case. This is simply because the bottom slip results in higher velocity for the permeable case, so because the volume flow rate is the same, the fluid layer is thinner for the permeable case. The fluid layer thickness at the peak of the q -wave for the thermal permeable case is greater than that for the isothermal impermeable case for the same reasons that the wave is more pronounced in the top panel.

The surface temperature, plotted in the bottom panel, shows the constant temperature in the isothermal case compared to the varying interface temperature in the case with bottom heating. The temperature varies with the bottom topography, and a dip in temperature coincides with the wave crest, where the much thicker fluid layer results in a temperature closer to the ambient temperature. The shift between the locations of the local maximum fluid layer thickness and minimum interface temperature that occur periodically with the bottom topography is also apparent in these results; the minimum temperature occurs further downstream than expected, based on the results of D'Alessio et al. [13], due to the bottom permeability.

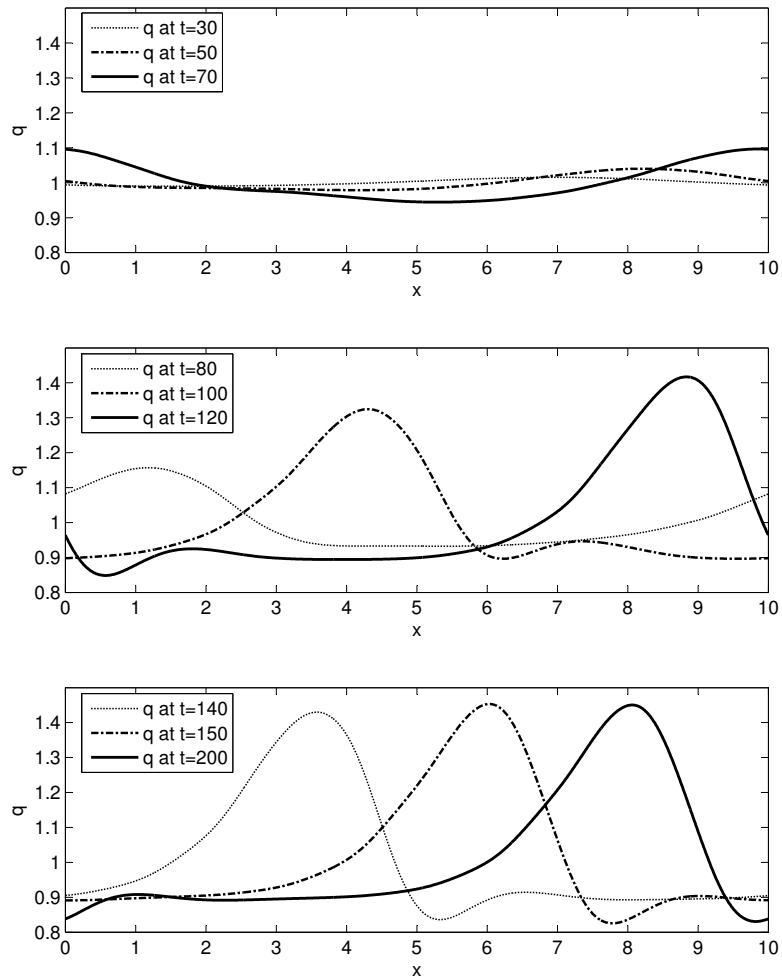


Figure 6.16: Volume flow rate evolution in time for a case with heating and permeability. $Re = 1.0$, $\delta = 0.1$, $\cot \beta = 0.5$, $We = 100$, $a_b = 0.2$, $Bi = Ma = 1$, and $\delta_1 = 0.1$. The WRM with the scaling $q_s = 1$ is used.

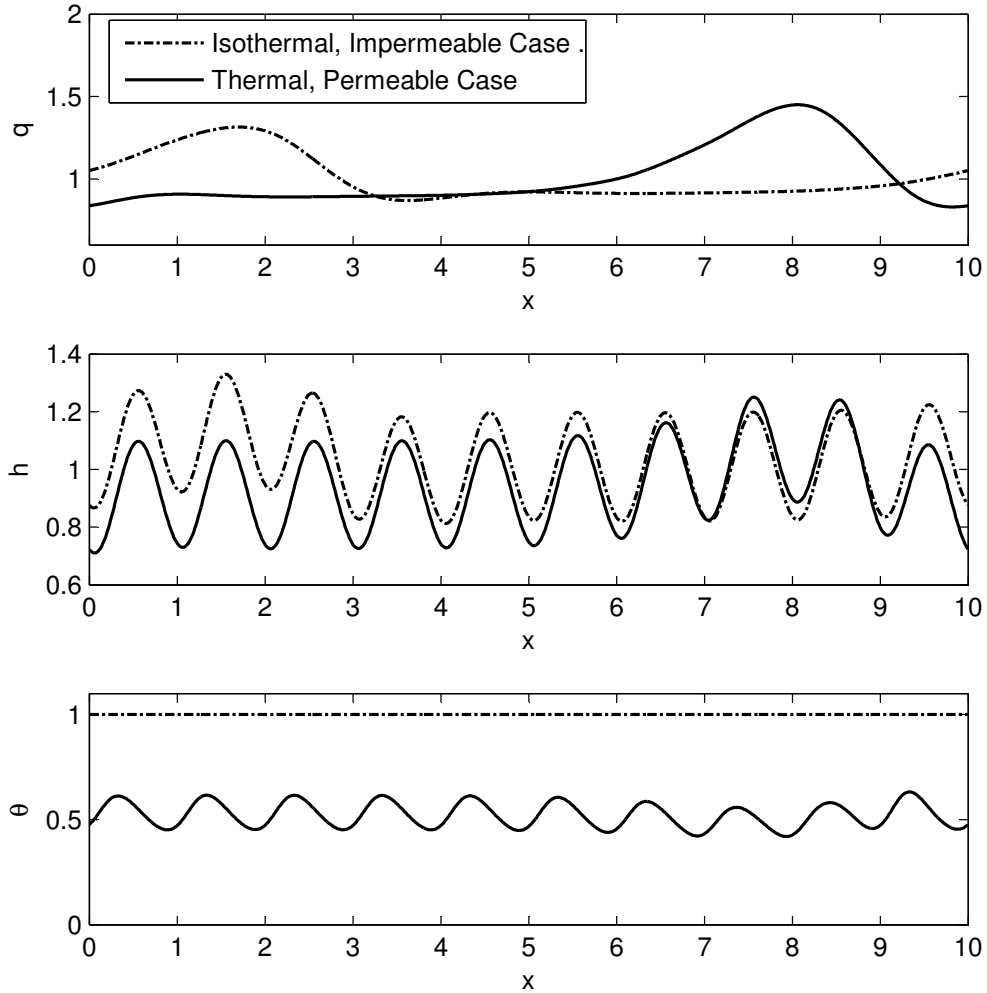


Figure 6.17: Comparison between a case with heating and bottom permeability and an impermeable, isothermal case at $t=200$. Both have $Re = 1.0$, $\delta = 0.1$, $\cot \beta = 0.5$, $We = 100$, $a_b = 0.2$, and a domain length of ten bottom wavelengths. The case with heating and permeability has $Bi = Ma = 1$ and $\delta_1 = 0.1$. The WRM with the scaling $q_s = 1$ is used.

6.6.1 Comparison to Full Navier-Stokes Numerical Solutions

Finally, the numerical results from the weighted residual model for a case with bottom permeability are compared to CFX results for the corresponding case. Heating is not included because the Marangoni effect requires surface tension, and CFX simulations with surface tension were problematic due to mass loss, as discussed in section 5.1.3. The flow considered is isothermal with surface tension being neglected, and an even bottom is used; however, bottom permeability is included. The flow parameters are $Re = 1.75$, $\delta = 0.089$, $\delta_1 = 0.14$, $\cot \beta = 1.38$. The permeability parameter value is based on the values of Foametal A used in the experiments by Beavers and Joseph [27, 40]. In CFX, the porous bottom is simulated by including a porous layer in the domain, which is saturated with fluid. A momentum loss term is included in the governing equations to model the porous layer; this term is based on the permeability of the material and the volume fraction of solid material. Figure 6.18 compares the CFX and weighted residual model results. The figure shows that the number of peaks match. The spacing is similar as are the height of the peaks, although the peaks in the weighted residual model results are slightly taller and farther apart. Other model simulations of the porous bottom problem match the corresponding CFX results fairly well; the results indicate that the weighted residual model continues to predict the flow well, even when permeability is added.

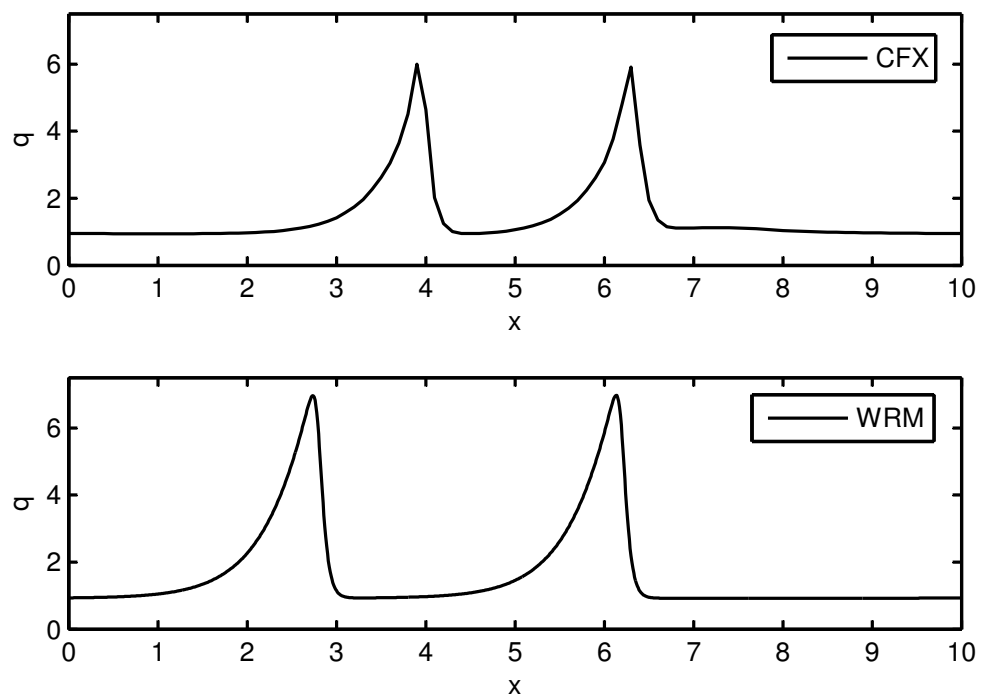


Figure 6.18: CFX and WRM results for a case with bottom porosity. The flow parameters are $Re = 1.75$, $\delta = 0.089$, $\delta_1 = 0.14$, $\cot \beta = 1.38$, and $We = Ma = Bi = a_b = 0$.

Chapter 7

Conclusions

In the first part of this study, three models for flow down a wavy inclined plane were compared. The development of each model and the assumptions made were described. The models were then compared by considering the predictions they make regarding the critical Reynolds number for flow over an even bottom, the neutral stability curve, the interface development in unstable flows, and the critical Reynolds number for flow over a wavy bottom. Based on the origins of the models, the SWM is expected to give the poorest results due to the assumptions inherent in its development; empirical terms were added to the shallow-water equations to account for viscosity and bottom friction, whereas these effects are properly included in the governing equations of the other two models. The IBL model is expected to perform better than the SWM because it is derived directly from the governing equations. However, it is known to erroneously predict the critical Reynolds number, whereas the weighted residual model, which is specifically developed to correct this shortfall, is expected to give the best results.

Comparing the critical Reynolds number predictions of the models to the theoretical result, which has been determined by others [1,2,14] using the Orr-Sommerfeld equation, it was found that only the WRM reproduces the theoretical value. The IBL model comes close, slightly over-predicting the correct result, and the shallow water model significantly under-predicts the correct value. Neutral stability curves were then compared to two sets of experimental data collected by Liu et al. [16] and Liu et al. [17]. Again, the WRM gives the best results, the IBL model predicts a curve shifted slightly to the right, while the SWM predicts a curve shifted significantly to the left. Based on these results, only the IBL model and the WRM were included in the remaining comparisons.

The IBL model and WRM were then solved numerically, using the fractional step method, for unstable cases. The results were compared to numerical solutions of the full Navier-

Stokes equations, obtained using the commercial software package CFX. Two cases were compared; the first excludes surface tension, and the second includes it. In both cases, the models gave results similar to those obtained using CFX; however, the WRM results were slightly better. In the first case, both models predicted the same number of peaks as CFX, although the height of the CFX peaks was better matched by the WRM. In the case with surface tension, the WRM correctly predicted the number of peaks calculated by CFX, whereas the IBL model predicted one less peak.

Finally, the critical Reynolds number for flow over a wavy bottom, as predicted by the WRM and the IBL model, were compared to experimental data. In this comparison, both models provided reasonable predictions, and both performed reasonably well. The results of this comparison also indicate that bottom topography has a stabilizing effect on the flow. To investigate this, an asymptotic analysis was conducted to determine the combined effect of bottom topography and weak surface tension, and it was found that bottom topography and weak surface tension acting together stabilize the flow. However, by constructing neutral stability curves for flow over a wavy bottom, it was later shown that the combination of strong surface tension and bottom topography destabilizes the flow, as found by D'Alessio et al. [13]. From these comparisons, it can be concluded that, overall, the WRM best predicts the features of flow over a wavy inclined plane. Based on this conclusion, the WRM was developed to include the effects of heating and bottom permeability.

The weighted residual method was extended to include both the effects of bottom heating and bottom permeability. A constant bottom temperature was applied, and a variation of the Beavers and Joseph slip condition [26–28] was used to model the bottom permeability. The results obtained from a linear stability analysis of the model equations were compared to those from the corresponding Benney equation and the two were found to agree; they also agree with the results of Sadiq et al. [4], who used the Orr-Sommerfeld equation to predict the critical Reynolds number. This confirms that the WRM continues to make accurate predictions regarding the stability of the flow, even when the model is extended to include bottom heating and permeability. The expression for the critical Reynolds number indicates that both heating and permeability destabilize the flow, as reported in the literature [7, 26], and that the interaction of the two effects is to further destabilize the flow. It was also found that increasing the bottom permeability or the Marangoni number monotonically destabilizes the flow for relevant values of the parameters. However, there is a specific Biot number for which the flow is most unstable. This is because, when the interface temperature is halfway between the bottom and the ambient temperatures, the interface temperature varies the most with changes in fluid layer thickness, thus enhancing the Marangoni effect; this occurs for a Biot number near one, at which the flow is most unstable.

As a final test of the WRM, numerical solutions of the full Navier-Stokes equations were compared to the model predictions for the case with bottom permeability without heating. A comparison with CFX for the case with heating is problematic due to the mass loss that occurs in CFX as a result of surface tension. However, the results with bottom permeability showed that the model does closely predict the CFX results, confirming that the WRM, when extended to include permeability, does predict the features of the flow well.

Future work on this problem could include investigating whether the Beavers and Joseph slip condition is the most appropriate for flow over a wavy bottom, or whether another condition, such as the LeBars and Worster model [39], should be applied. As well, simulations of the full Navier-Stokes and energy equations should be conducted for comparison to the WRM predictions to confirm that the model, including both of these effects, accurately predicts the development of the interface. Finally, three-dimensional instabilities and flows could be considered.

APPENDICES

Appendix A

Linear Stability over a Wavy Bottom with Heating and Porosity

A linear stability analysis of the model equations, (6.31), for flow over a wavy inclined plane with bottom heating and permeability is conducted by using Floquet theory. This procedure is outlined here. A similar analysis using the IBL model, equations (3.12) and (3.13), for isothermal impermeable flow was also performed. The linearized perturbation equations corresponding to equation (6.31) are

$$\frac{\partial \hat{h}}{\partial t} + \frac{\partial \hat{q}}{\partial x} = 0 , \quad (\text{A.1})$$

$$\frac{\partial \hat{q}}{\partial t} + f_1 \frac{\partial^2 \hat{q}}{\partial x^2} + f_2 \frac{\partial \hat{q}}{\partial x} + f_3 \hat{q} + f_4 \frac{\partial^3 \hat{h}}{\partial x^3} + f_5 \frac{\partial^2 \hat{h}}{\partial x^2} + f_6 \frac{\partial \hat{h}}{\partial x} + f_7 \hat{h} + f_8 \frac{\partial^2 \hat{\theta}}{\partial x t} + f_9 \frac{\partial^2 \hat{\theta}}{\partial x^2} + f_{10} \frac{\partial \hat{\theta}}{\partial x} = 0 , \quad (\text{A.2})$$

$$\frac{\partial \hat{\theta}}{\partial t} + g_1 \frac{\partial^2 \hat{\theta}}{\partial x^2} + g_2 \frac{\partial \hat{\theta}}{\partial x} + g_3 \hat{\theta} + g_4 \frac{\partial \hat{q}}{\partial x} + g_5 \hat{q} + g_6 \frac{\partial^2 \hat{h}}{\partial x^2} + g_7 \frac{\partial \hat{h}}{\partial x} + g_8 \hat{h} = 0 , \quad (\text{A.3})$$

where the hats denote perturbations. The coefficients $f_1 - f_{10}$ and $g_1 - g_8$ are

$$\begin{aligned}
f_1 &= \frac{1}{q_t(h+2\delta_1)\delta h^2} \left[\frac{-9}{2} \frac{\delta^2}{Re} h^3 \right] , \\
f_2 &= \frac{1}{q_t(h+2\delta_1)\delta h^2} \left[\frac{-19}{336} \delta^2 Ma Reh^4 \theta_x + \frac{17}{7} \delta \delta_1 h + \frac{9}{2} \frac{\delta^2}{Re} h^2 h_x + \frac{17}{7} \delta h^2 \right] , \\
f_3 &= \frac{1}{q_t(h+2\delta_1)\delta h^2} \left[6 \frac{\delta^2}{Re} h^2 h_{xx} - \frac{18}{7} \delta h h_x + \frac{45}{8} \delta \delta_1 \zeta' - 4 \frac{\delta^2}{Re} h (h_s)^2 + \frac{5}{2} \frac{h}{Re} + \frac{15}{4} \frac{\delta^2}{Re} \zeta'' h^2 + \frac{5}{2} \frac{\delta^2}{Re} h h_x \zeta' \right. \\
&\quad \left. - \frac{15}{224} \delta^2 Re Mah^4 \theta_{xx} - \frac{5}{112} \delta^2 Re Mah^3 \theta_x h_x + 5 \frac{\delta^2}{Re} (\zeta')^2 h \right] , \\
f_4 &= \frac{1}{q_t(h+2\delta_1)\delta h^2} \left[\frac{-5}{6} \delta^3 We h^3 (3\delta_1 + h) \right] , \\
f_5 &= \frac{1}{q_t(h+2\delta_1)\delta h^2} \left[6 \frac{\delta^2}{Re} h^2 \right] , \\
f_6 &= \frac{1}{q_t(h+2\delta_1)\delta h^2} \left[\frac{5}{2} \frac{\delta}{Re} \cot \beta h^4 - 8 \frac{\delta^2}{Re} h h_x - \frac{5}{112} \delta^2 Re Mah^3 \theta_x + \frac{15}{2} \frac{\delta}{Re} \cot \beta \delta_1 h^3 - \frac{9}{7} \delta h + \frac{5}{2} \frac{\delta^2}{Re} h \zeta' \right] , \\
f_7 &= \frac{1}{q_t(h+2\delta_1)\delta h^2} \left[\left(\frac{-15}{2} \delta_1 - \frac{10}{3} h \right) h^2 \delta^3 We (h_{xxx} + \zeta''') + 10 \frac{\delta}{Re} \cot \beta h^3 (h_x + \zeta') + 12 \frac{\delta^2}{Re} h h_{xx} \right. \\
&\quad - 10 \frac{H^3}{Re} + \frac{45}{2} \frac{\delta}{Re} \cot \beta \delta_1 \zeta' h^2 - \frac{45}{2} \frac{\delta_1}{Re} h^2 - \frac{9}{7} \delta h_x + 5 \delta Ma \delta_1 h \theta_x + \frac{15}{4} \delta Mah^2 \theta_x \\
&\quad + 5 \frac{\delta^2}{Re} (\zeta')^2 + \frac{15}{2} \frac{\delta^2}{Re} \zeta'' h + \frac{5}{2} \frac{\delta^2}{Re} \zeta' h_x - \frac{15}{56} \delta^2 Re Mah^3 \theta_{xx} - 4 \frac{\delta^2}{Re} (h_x)^2 \\
&\quad \left. + \frac{5}{2} \frac{1}{Re} - \frac{15}{112} \delta^2 Re Mah^2 \theta_x h_x + \frac{45}{2} \frac{\delta}{Re} \cot \beta \delta_1 h^2 h_x \right] , \\
f_8 &= \frac{1}{q_t(h+2\delta_1)\delta h^2} \left[\frac{-1}{48} \delta^2 Re Mah^5 \right] , \\
f_9 &= \frac{1}{q_t(h+2\delta_1)\delta h^2} \left[\frac{-15}{224} \delta^2 Re Mah^4 \right] , \\
f_{10} &= \frac{1}{q_t(h+2\delta_1)\delta h^2} \left[\frac{5}{4} h + \frac{5}{2} \delta_1 - \frac{5}{112} \delta Reh h_x \right] Ma \delta h^2 , \tag{A.4}
\end{aligned}$$

$$\begin{aligned}
g_1 &= \delta \left[\frac{3}{80} MaReh(1 - \theta) - \frac{1}{Pe} \right] , \\
g_2 &= \frac{1}{\delta Pe h^3} \left[\frac{1}{20} \delta Pe h (27h - 21\delta_1) + \frac{3}{40} \delta^2 Pe MaReh^3 (h_x(1 - \theta) - 2h\theta) - \delta^2 h^2 h_x \right] , \\
g_3 &= \frac{1}{\delta Pe h^3} \left[-3\delta^2 \zeta' h h_x + 3\delta^2 Bi \zeta' h^2 h_x - \frac{3}{80} \delta^2 Pe MaReh^3 \theta_{xx} + 3Bi h^2 + \delta^2 h^2 h_{xx} \right. \\
&\quad \left. + \frac{3}{2} \delta^2 Bi h^2 h_x - 2\delta^2 h (h_x)^2 + 3h + \frac{3}{2} \delta^2 \zeta'' h^2 \right. \\
&\quad \left. + \frac{3}{20} \delta^2 Bi (\zeta')^2 h^2 + \frac{21}{20} \delta Pe \delta_1 h_x - \frac{9}{2} \delta Pe \delta_1 \zeta' - \frac{3}{40} \delta^2 Pe MaReh^3 \theta_x h_x \right] , \\
g_4 &= \frac{1}{h^2} \left[\frac{7}{40} (1 - \theta) (3\delta_1 - h) \right] , \\
g_5 &= \frac{1}{h^3} \left[(1 - \theta) \left(\frac{9}{2} \zeta' - \frac{21}{40} h_x \right) \delta_1 - \frac{21}{40} \delta_1 h \theta_x + \frac{27}{20} h^2 \theta_x \right] , \\
g_6 &= \frac{1}{Pe h} [\delta(\theta - 1)] , \\
g_7 &= \frac{1}{\delta Pe h^3} h_x \left[(1 - \theta) \left(\frac{3}{40} \delta^2 Pe Re Ma h^3 \theta_x + 4\delta^2 h h_x \right. \right. \\
&\quad \left. \left. + 3\delta^2 \zeta' h - \frac{21}{20} \delta Pe \delta_1 \right) + 3\delta^2 Bi h^2 \theta (\zeta' + h_x) - \delta^2 h^2 \theta_x \right] , \\
g_8 &= \frac{1}{\delta Pe h^3} \left[\left(\frac{3}{20} \delta^2 Pe MaReh^3 \theta_{xx} - 2\delta^2 h h_{xx} - 3\delta^2 \zeta'' h + \frac{9}{40} \delta^2 Pe MaReh^2 \theta_x h_x \right. \right. \\
&\quad \left. \left. + 2\delta^2 (h_x)^2 + 3\delta^2 \zeta' h_x - 3 \right) (1 - \theta) + 3\delta^2 Bi h \theta (\zeta' + h_x)^2 + \frac{27}{10} \delta Pe h \theta_x - 3\delta^2 h^2 \theta_{xx} \right. \\
&\quad \left. - \frac{3}{10} \delta^2 Pe MaReh^3 (\theta_x)^2 + 6Bi h \theta - 2\delta^2 h \theta_x h_x \right] , \tag{A.5}
\end{aligned}$$

where subscripts indicate partial derivatives. Setting $Ma = Bi = \delta_1 = 0$ reproduces equation (5.6), which applies to the isothermal impermeable problem for the weighted residual model. The perturbations are expanded in a complex Fourier series as follows:

$$\begin{aligned}
\hat{h} &= e^{\sigma t + iKx} \sum_{n=-\infty}^{\infty} \hat{h}_n e^{in2\pi x} , \\
\hat{q} &= e^{\sigma t + iKx} \sum_{n=-\infty}^{\infty} \hat{q}_n e^{in2\pi x} , \\
\hat{\theta} &= e^{\sigma t + iKx} \sum_{n=-\infty}^{\infty} \hat{\theta}_n e^{in2\pi x} .
\end{aligned} \tag{A.6}$$

Since the coefficients, equations (A.4) and (A.5), are periodic functions due to the periodic nature of the bottom topography, they can also be expanded in a complex Fourier series given by

$$f_k = \sum_{n=-\infty}^{\infty} \hat{f}_{k,n} e^{in2\pi x} \quad \text{where } k = 1, 2, \dots, 10 . \tag{A.7}$$

The same is done for $g_1 - g_8$. The series are then truncated, and only terms from $-N$ to N are included, where N is taken to be sufficiently large so as not to influence the results.

When these series are substituted into equations (A.1) to (A.3), a system of equations results, which can be expressed as a generalized eigenvalue problem given by

$$\mathbf{A}\vec{V} = \sigma\mathbf{B}\vec{V}, \quad (\text{A.8})$$

where

$$\mathbf{A} = \left(\begin{array}{c|c|c} \mathbf{A}^1 & \mathbf{A}^2 & \mathbf{A}^3 \\ \hline \mathbf{A}^4 & \mathbf{0} & \mathbf{0} \\ \hline \mathbf{A}^7 & \mathbf{A}^8 & \mathbf{A}^9 \end{array} \right), \quad (\text{A.9})$$

$$\mathbf{B} = \left(\begin{array}{c|c|c} \mathbf{I} & \mathbf{0} & \mathbf{B}^3 \\ \hline \mathbf{0} & \mathbf{I} & \mathbf{0} \\ \hline \mathbf{0} & \mathbf{0} & \mathbf{I} \end{array} \right), \quad (\text{A.10})$$

and

$$\vec{V} = \begin{pmatrix} q_{-N} \\ \vdots \\ q_N \\ h_{-N} \\ \vdots \\ h_N \\ \theta_{-N} \\ \vdots \\ \theta_N \end{pmatrix}. \quad (\text{A.11})$$

The sub-matrices $\mathbf{A}^1 - \mathbf{A}^9$ and \mathbf{B}^3 are each $(2N + 1) \times (2N + 1)$ square matrices with the elements given by

$$\begin{aligned}
\mathbf{A}^1_{l,m} &= f_{3,l-m} + i[K + 2\pi(m - 1 - N)]f_{2,l-m} - [K + 2\pi(m - 1 - N)]^2 f_{1,l-m} , \\
\mathbf{A}^2_{l,m} &= f_{7,l-m} + i[K + 2\pi(m - 1 - N)]f_{6,l-m} - [K + 2\pi(m - 1 - N)]^2 f_{5,l-m} \\
&\quad - [K + 2\pi(m - 1 - N)]^3 f_{4,l-m} , \\
\mathbf{A}^3_{l,m} &= i[K + 2\pi(m - 1 - N)]f_{10,l-m} - [K + 2\pi(m - 1 - N)]^2 f_{9,l-m} , \\
\mathbf{A}^4_{l,m} &= \delta_{l,m} i[K + 2\pi(m - 1 - N)] , \\
\mathbf{A}^7_{l,m} &= g_{5,l-m} + i[K + 2\pi(m - 1 - N)]g_{4,l-m} , \\
\mathbf{A}^8_{l,m} &= g_{8,l-m} + i[K + 2\pi(m - 1 - N)]g_{7,l-m} - [K + 2\pi(m - 1 - N)]^2 g_{6,l-m} , \\
\mathbf{A}^9_{l,m} &= g_{3,l-m} + i[K + 2\pi(m - 1 - N)]g_{2,l-m} - [K + 2\pi(m - 1 - N)]^2 g_{1,l-m} , \\
\mathbf{B}^3_{l,m} &= i[K + 2\pi(m - 1 - N)]f_{8,l-m} , \tag{A.12}
\end{aligned}$$

where $\delta_{l,m}$ in $\mathbf{A}^4_{l,m}$ is the Kronecker Delta. Matrices \mathbf{A}^1 - \mathbf{A}^3 and \mathbf{B}^3 come from the momentum equations, \mathbf{A}^4 comes from the conservation of mass equation, and \mathbf{A}^7 - \mathbf{A}^9 come from the energy equation. The vector \vec{V} has length $(6N + 3)$.

It is clear from the form of matrix \mathbf{B} , which is upper-triangular with ones along the diagonal, that \mathbf{B} is non-singular and hence equation (A.8) can be converted to the standard eigenvalue problem. For a given set of parameters and perturbation wavenumber, σ can be found using the matrix system equation (A.8) and the Matlab routine $\text{eig}(\mathbf{A}, \mathbf{B})$. In the absence of heating and permeability, $\mathbf{B} = \mathbf{I}$, and equation (A.8) reduces to the standard eigenvalue problem; σ can then be found using the Matlab routine $\text{eig}(\mathbf{A})$. A number of σ values equal to $6N + 3$ will be found; the appropriate value is determined by examining the phase speed given by $c = \frac{\Im(\sigma)}{K}$. The phase speed should be near $c = 3$, which is the exact value for the even bottom impermeable case, as noted in sections 2.2.1 and 2.2.2; further, adding permeability only modifies this value slightly, as shown in section 6.4.2. Only few eigenvalues, typically one or two, were found to satisfy this criterion, and of these, the value with the largest growth rate determines the stability of the flow.

Appendix B

Effect of Surface Tension on Flow Stability

The effect of surface tension on the stability of the flow is investigated by conducting an asymptotic analysis of the governing steady-state equations. The steady-state flow variables are expanded in power series of δ as follows:

$$\begin{aligned}u_s(x, z) &= u_0 + \delta u_1 + \delta^2 u_2 + \dots , \\w_s(x, z) &= w_0 + \delta w_1 + \delta^2 w_2 + \dots , \\p_s(x, z) &= p_0 + \delta p_1 + \delta^2 p_2 + \dots , \\h_s(x, z) &= 1 + \delta h_1 + \delta^2 h_2 + \dots .\end{aligned}\tag{B.1}$$

These expansions are substituted into the steady-state, isothermal governing equations, given by

$$\begin{aligned}\frac{\partial u}{\partial x} + \frac{\partial w}{\partial z} &= 0 , \\ \delta Re \left(u \frac{\partial u}{\partial x} + w \frac{\partial u}{\partial z} \right) &= -\delta Re \frac{\partial p}{\partial x} + 3 + \delta^2 \frac{\partial^2 u}{\partial x^2} + \frac{\partial^2 u}{\partial z^2} , \\ \delta^2 Re \left(u \frac{\partial w}{\partial x} + w \frac{\partial w}{\partial z} \right) &= -Re \frac{\partial p}{\partial z} - 3 \cot \beta + \delta^3 \frac{\partial^2 u}{\partial x^2} + \delta \frac{\partial^2 u}{\partial z^2} .\end{aligned}\tag{B.2}$$

The series expansions are also substituted into the boundary conditions given by

$$\left. \begin{aligned} p - \frac{2\delta}{Re} \frac{\partial w}{\partial z} + \delta^2 We \frac{\partial^2(h+\zeta)}{\partial x^2} = 0 \\ \frac{\partial u}{\partial z} - 4\delta^2 \frac{\partial(h+\zeta)}{\partial x} \frac{\partial u}{\partial x} + \delta^2 \frac{\partial w}{\partial x} = 0 \end{aligned} \right\} \text{ at } z = h + \zeta , \quad (\text{B.3})$$

and

$$\left. \begin{aligned} u = 0 \\ w = 0 \end{aligned} \right\} \text{ at } z = \zeta . \quad (\text{B.4})$$

The surface boundary conditions are expanded in a Taylor series about $z = 1 + \zeta$. This allows problems at each order of δ to be formulated. The leading order problem is

$$\begin{aligned} \frac{\partial u_0}{\partial x} + \frac{\partial w_0}{\partial z} &= 0 , \\ 3 + \frac{\partial^2 u_0}{\partial z^2} &= 0 , \\ 3 \cot \beta + Re \frac{\partial p_0}{\partial z} &= 0 , \end{aligned} \quad (\text{B.5})$$

subject to the boundary conditions

$$\left. \begin{aligned} p_0 = 0 \\ \frac{\partial u_0}{\partial z} = 0 \end{aligned} \right\} \text{ at } z = 1 + \zeta , \quad (\text{B.6})$$

and

$$\left. \begin{aligned} u_0 = 0 \\ w_0 = 0 \end{aligned} \right\} \text{ at } z = \zeta . \quad (\text{B.7})$$

This problem can be solved to find

$$\begin{aligned} u_0 &= \frac{3}{2}(z - \zeta)(\zeta - z + 2) , \\ w_0 &= \frac{3}{2}(z - \zeta)(\zeta - z + 2) \frac{d\zeta}{dx} , \\ p_0 &= \frac{3 \cot \beta}{Re} (\zeta - z + 1) . \end{aligned} \quad (\text{B.8})$$

The order δ problem is

$$\begin{aligned}
\frac{\partial u_1}{\partial x} + \frac{\partial w_1}{\partial z} &= 0 , \\
Re \left(u_0 \frac{\partial u_0}{\partial x} + w_0 \frac{\partial u_0}{\partial z} + \frac{\partial p_0}{\partial x} \right) &= \frac{\partial^2 u_1}{\partial z^2} , \\
Re \frac{\partial p_1}{\partial z} &= \frac{\partial^2 w_0}{\partial z^2} ,
\end{aligned} \tag{B.9}$$

subject to the boundary conditions

$$\left. \begin{aligned}
p_1 + h_1 \frac{\partial p_0}{\partial z} + \frac{2}{Re} \frac{d\zeta}{dx} \frac{\partial u_0}{\partial z} &= \frac{2}{Re} \frac{\partial w_0}{\partial z} \\
\frac{\partial u_1}{\partial z} + h_1 \frac{\partial^2 u_0}{\partial z^2} &= 0
\end{aligned} \right\} \text{ at } z = 1 + \zeta , \tag{B.10}$$

and

$$\left. \begin{aligned}
u_1 &= 0 \\
w_1 &= 0
\end{aligned} \right\} \text{ at } z = \zeta . \tag{B.11}$$

For this problem, a series expansion solution for the steady fluid layer thickness, h_s , is required. The series solution of the weighted residual model, as described in section 3.4 is used. The steady-state WRM equation,

$$\begin{aligned}
\frac{5\delta^2 We}{6} h_s^3 h_s''' - \frac{6\delta}{Re} h_s h_s'' + \frac{4\delta}{Re} (h_s')^2 - \left[\frac{5 \cot \beta}{2Re} h_s^3 + \frac{5\delta}{2Re} \zeta' - \frac{9}{7} \right] h_s' - \frac{15\delta}{4Re} \zeta'' h_s \\
+ \left[\frac{5}{2\delta Re} - \frac{5 \cot \beta}{2Re} \zeta' + \frac{5\delta^2 We}{6} \zeta''' \right] h_s^3 = \frac{5}{2\delta Re} + \frac{5\delta}{Re} (\zeta')^2
\end{aligned} , \tag{B.12}$$

is used to find a series solution for h_s up to $O(\delta^4)$. The first few terms are

$$\begin{aligned}
h_s &= 1 + \delta \frac{\cot \beta}{3} \zeta'(x) \\
&+ \delta^2 \left(\frac{2}{3} \left(1 + \frac{\cot^2 \beta}{3} \right) [\zeta'(x)]^2 + \left(\frac{1}{2} - \frac{2Re \cot \beta}{35} + \frac{\cot^2 \beta}{9} \right) \zeta''(x) \right) + O(\delta^3) .
\end{aligned} \tag{B.13}$$

The order δ problem from the governing equations can then be solved to find

$$\begin{aligned}
u_1 &= \frac{1}{2} \cot \beta \zeta' (\zeta - z) (3\zeta - 3z + 4) , \\
w_1 &= \frac{1}{2} \cot \beta (\zeta - z) \left((\zeta - z)^2 \zeta'' + (2\zeta'' + 3(\zeta')^2) (\zeta - z) + 4(\zeta')^2 \right) , \\
p_1 &= \frac{1}{Re} \zeta' (3\zeta - 3z + 3 + \cot^2 \beta) .
\end{aligned} \tag{B.14}$$

This process is continued to find solutions up to order δ^4 . The free-surface velocity, $u_s(z = 1 + \zeta)$, and from this the average value across one bottom wavelength, \bar{u}_s , is computed. The mean surface drift, U_s , is then defined as the difference between \bar{u}_s and the corresponding value for the even bottom, steady-state problem [13]. The mean surface drift is given by the expression

$$\begin{aligned} U_s &= \bar{u}_s - \frac{3}{2} = \int_0^1 u_s(x, z = 1 + \zeta) dx - \int_0^1 u_0(x, z = 1 + \zeta) dx \\ &= - \left(2 + \frac{7}{9} \cot^2 \beta \right) \pi^2 a_b^2 \delta^2 - \left(f(Re, a_b, \cot \beta) + \frac{152}{27} \cot \beta Re We \right) \pi^4 a_b^2 \delta^4, \end{aligned} \quad (\text{B.15})$$

where

$$\begin{aligned} f(Re, a_b, \cot \beta) &= \frac{286}{105} Re \cot \beta + \frac{304}{315} Re \cot^3 \beta - \frac{12113}{44100} Re^2 \cot^2 \beta - 14 - \frac{136}{9} \cot^2 \beta \\ &- \frac{76}{81} \cot^4 \beta + \frac{8}{9} a_b^2 \cot^2 \beta + \frac{298}{81} a_b^2 \cot^4 \beta - \frac{5}{3} a_b^4. \end{aligned} \quad (\text{B.16})$$

The first term on the right-hand-side of equation (B.15) indicates that bottom topography decreases the average surface velocity, and the second term indicates that surface tension also decreases this quantity. This result shows that bottom topography and weak surface tension stabilize the flow, as it slows down the flow. This result can also be reached by considering the average volume flow rate. This is found by integrating the fluid velocity $u_s(x, z)$ across one bottom wavelength, from $x = 0$ to $x = 1$, and through the depth of the fluid, from $z = \zeta$ to $z = 1 + \zeta$, as follows:

$$\bar{Q}_s = \int_0^1 \int_{\zeta}^{1+\zeta} u_s(x, z) dz dx = 1 - \left(2 + \frac{7}{18} \cot^2 \beta \right) \pi^2 a_b^2 \delta^2 + g(We, Re, a_b, \cot \beta) \pi^4 a_b^2 \delta^4, \quad (\text{B.17})$$

where

$$\begin{aligned} g(We, Re, a_b, \cot \beta) &= \left(38 - \frac{1193}{8} a_b^2 \right) \frac{\cot^4 \beta}{81} - \frac{152}{315} Re \cot^3 \beta + \left(66 + \frac{63139}{53900} Re^2 - 4a_b^2 \right) \frac{\cot^2 \beta}{9} \\ &- \left(\frac{59}{60} + \frac{76}{27} We \right) Re \cot \beta + \frac{51}{10} + \frac{16}{3} a_b^2. \end{aligned} \quad (\text{B.18})$$

This shows that the volume flow rate is also decreased by bottom topography and weak surface tension, and hence stabilizes the flow.

PERMISSIONS

**CAMBRIDGE UNIVERSITY PRESS LICENSE
TERMS AND CONDITIONS**

Feb 01, 2011

This is a License Agreement between Kelly A Ogden ("You") and Cambridge University Press ("Cambridge University Press") provided by Copyright Clearance Center ("CCC"). The license consists of your order details, the terms and conditions provided by Cambridge University Press, and the payment terms and conditions.

All payments must be made in full to CCC. For payment instructions, please see information listed at the bottom of this form.

License Number	2600350872939
License date	Feb 01, 2011
Licensed content publisher	Cambridge University Press
Licensed content publication	The Journal of Fluid Mechanics
Licensed content title	
Licensed content author	M. LE BARS and M. GRAE WORSTER
Licensed content date	Dec 31, 1969
Volume number	550
Issue number	-1
Start page	149
End page	173
Type of Use	Dissertation/Thesis
Requestor type	Author
Portion	Full article
Author of this Cambridge University Press article	No
Author / editor of the new work	Yes
Order reference number	
Territory for reuse	World
Title of your thesis / dissertation	Flow Down a Wavy Inclined Plane
Expected completion date	Mar 2011
Estimated size(pages)	118
Billing Type	Invoice
Billing Address	Unit 308 383 Albert Street Waterloo, ON N2L6E3 Canada
Customer reference info	
Total	0.00 USD

[Terms and Conditions](#)

TERMS & CONDITIONS

Cambridge University Press grants the Licensee permission on a non-exclusive non-transferable basis to reproduce, make available or otherwise use the Licensed content 'Content' in the named territory 'Territory' for the purpose listed 'the Use' on Page 1 of this Agreement subject to the following terms and conditions.

1. The License is limited to the permission granted and the Content detailed herein and does not extend to any other permission or content.
2. Cambridge gives no warranty or indemnity in respect of any third-party copyright material included in the Content, for which the Licensee should seek separate permission clearance.
3. The integrity of the Content must be ensured.
4. The License does extend to any edition published specifically for the use of handicapped or reading-impaired individuals.
5. The Licensee shall provide a prominent acknowledgement in the following format: author/s, title of article, name of journal, volume number, issue number, page references, © Cambridge Journals, reproduced with permission.

Other terms and conditions: None

v1.0

Gratis licenses (referencing \$0 in the Total field) are free. Please retain this printable license for your reference. No payment is required.

If you would like to pay for this license now, please remit this license along with your payment made payable to "COPYRIGHT CLEARANCE CENTER" otherwise you will be invoiced within 48 hours of the license date. Payment should be in the form of a check or money order referencing your account number and this invoice number RLNK10923838.






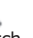





Once you receive your invoice for this order, you may pay your invoice by credit card. Please follow instructions provided at that time.

**Make Payment To:
Copyright Clearance Center
Dept 001
P.O. Box 843006
Boston, MA 02284-3006**

If you find copyrighted material related to this license will not be used and wish to cancel, please contact us referencing this license number 2600350872939 and noting the reason for cancellation.

Questions? customercare@copyright.com or +1-877-622-5543 (toll free in the US) or +1-978-646-2777.


Open Folder

Inbox: Re: Permission to use figures from paper published by WIT Press
(5 of 915)  

Mark as: Move Copy This message to Back to Inbox ◀ ▶
[Delete](#) [Reply](#) [Forward](#) [Redirect](#) [View Thread](#) [Blacklist](#) [Whitelist](#) [Message Source](#) [Save as](#) [Print](#) [Report as Spam](#)
[Report as Innocent](#) [Headers](#)

Date: Mon, 07 Feb 2011 12:18:00 +0000 [07:18:00 EST]

From: Brian Privett <bprivett@witpress.com> 

To: kaogden@uwaterloo.ca

Cc: Dee Halzack <DHalzack@witpress.com>

Subject: Re: Permission to use figures from paper published by WIT Press

Thank you for your enquiry regarding permissions.

Publication: 'Advances in Fluid Mechanics VIII'

ISBN 978-1-84564-476-5.

Editors: M. Rahman & C.A. Brebbia

Material for which reproduction permission is sought:

Paper: Modelling Gravity-Driven Flow over Uneven Surfaces

Author(s): Kelly Ogden *et al*

Proposed Use: Thesis.

As per your request, we hereby grant you permission to reproduce the aforementioned material in print and electronic format at no charge subject to the following conditions:

If any part of the material to be used (for example, figures) has appeared in our publication with credit or acknowledgement to another source, permission must also be sought from that source. If such permission is not obtained then that material may not be included in your publication/copies.

Suitable acknowledgement to the source must be made, either as a footnote or in a reference list at the end of your publication, as follows:

"Reprinted from Publication title, Vol number (if applicable), Author(s) or Editor(s), Title of article or chapter, Pages No., Copyright (Year), with permission from WIT Press, Southampton, UK".

This permission is granted for non-exclusive world English rights only. For other languages please reapply separately for each one required.

Reproduction of this material is confined to the purpose for which permission is hereby given.

Yours sincerely,

Brian Privett

--

Head of Production & Editorial

Email: bprivett@witpress.com

=====

WIT PRESS ... for scientists by scientists

WIT Press is committed to Open Access and the free flow of information.

WIT Press, Ashurst Lodge, Ashurst, Southampton SO40 7AA, UK.
Tel : 44 (0)238 029 3223 Fax : 44 (0)238 029 2853
Company registration number 4741634

=====

WIT Press on the web - visit <http://www.witpress.com>
Download individual Wessex Institute conference papers from our WIT
eLIBRARY

WESSEX INSTITUTE on the web: <http://www.wessex.ac.uk>

VIEW 2011 Call for Papers at:
<http://www.wessex.ac.uk/11-conferences.html>

BEASY on the web: <http://www.beasy.com>

=====

Delete | Reply | Forward | Redirect | View Thread | Blacklist | Whitelist | Message Source | Save as | Print | Report as Spam |
Report as Innocent | Headers

Mark as: Move | Copy | This message to Back to Inbox ◀ ▶

References

- [1] T. Benjamin, “Wave formation in laminar flow down an inclined plane,” *J. Fluid Mech.*, vol. 2, pp. 554–574, 1957.
- [2] C.-S. Yih, “Stability of liquid flow down an inclined plane,” *The Physics of Fluids*, vol. 6, pp. 321–334, 1963.
- [3] S. D’Alessio, J. Pascal, and H. Jasmine, “Instability in gravity-driven flow over uneven surfaces,” *Physics of Fluids*, vol. 21, pp. 062105–1 – 062105–11, 2009.
- [4] I. Sadiq, R. Usha, and S. Joo, “Instabilities in a liquid film flow over an inclined heated porous substrate,” *Chemical Engineering Science*, vol. 65, pp. 4443–4459, 2010.
- [5] N. Balmforth and S. Mandre, “Dynamics of roll waves,” *J. Fluid Mech.*, vol. 514, pp. 1–33, 2004.
- [6] U. Thiele, B. Goyeau, and M. Velarde, “Stability analysis of thin film flow along a heated porous wall,” *Physics of Fluids*, vol. 21, pp. 014103–1 – 014103–16, 2009.
- [7] P. Trevelyan, B. Scheid, C. Ruyer-Quil, and S. Kalliadasis, “Heated falling films,” *J. Fluid. Mech.*, vol. 592, pp. 295–334, 2007.
- [8] J. Pascal and S. D’Alessio, “Instability in gravity riven flow over uneven permeable surfaces,” *International Journal of Multiphase Flow*, vol. 36, pp. 449–459, 2010.
- [9] K. Nong and D. Anderson, “The film evolution over a thin porous layer: modeling a tear film on a contact lens,” *SIAM Journal of Applied Mathematics*, vol. 70, no. 7, pp. 2771–2795, 2010.
- [10] Kapitza, “1,” *J. Fluid Mech.*, vol. 475, pp. 377–408, 1948.
- [11] Kapitza and Kapitza, “2,” *J. Fluid Mech.*, vol. 475, pp. 377–408, 1949.

- [12] R. Dressler, “Mathematical solution of the problem of roll-waves in inclined open channels,” *Communications on Pure and Applied Mathematics*, vol. 2, pp. 149 – 194, 1949.
- [13] S. D’Alessio, J. Pascal, H. Jasmine, and K. Ogden, “Film flow over heated wavy inclined surfaces,” *J. Fluid Mech.*, vol. 665, pp. 418 – 456, 2010.
- [14] D. Benney, “Long waves on liquid films,” *Journal of Mathematics and Physics*, vol. 45, pp. 150–155, 1966.
- [15] V. Y. Shkadov, “Wavy flow regimes of a thin layer of viscous fluid subject to gravity,” *Izv. Akad. Nauk SSSP, Mekh. Zhidk Gaza*, vol. 2, no. 1, pp. 43–51, 1967.
- [16] J. Liu, J. Paul, and J. Gollub, “Measurements of the primary instabilities of film flows,” *J. Fluid Mech.*, vol. 250, pp. 69–101, 1993.
- [17] J. Liu, J. Schneider, and J. Gollub, “Three-dimensional instabilities of film flow,” *Physics of Fluids*, vol. 7, pp. 55–67, 1995.
- [18] A. Wierschem, C. Lepski, and N. Aksel, “Effect of long undulated bottoms on thin gravity-driven films,” *Acta Mechanica*, vol. 179, pp. 41–66, 2005.
- [19] B. Ramaswamy, S. Chippada, and S. W. Joo, “A full-scale numerical study of interfacial instabilities in thin-film flows,” *J. Fluid Mech.*, vol. 325, pp. 163–194, 1996.
- [20] C. Ruyer-Quil and P. Manneville, “Modeling film flows down inclined planes,” *The European Physical Journal B*, vol. 6, pp. 277–292, 1998.
- [21] C. Ruyer-Quil and P. Manneville, “Improved modeling of flows down inclined planes,” *The European Physical Journal B*, vol. 15, pp. 357–369, 2000.
- [22] C. Ruyer-Quil and P. Manneville, “Further accuracy and convergence results on the modeling of flows down inclined planes by weighted residual approximations,” *Physics of Fluids*, vol. 14, pp. 170–183, 2002.
- [23] S. Kalliadasis, A. Kiyashko, and E. Demekhin, “Marangoni instability of a thin liquid film heated from below by a local heat source,” *J. Fluid Mech.*, vol. 475, pp. 377–408, 2003.
- [24] C. Ruyer-Quil, B. Scheid, S. Kalliadasis, M. Velarde, and R. Zeytounian, “Thermocapillary long waves in a liquid film flow. part 1. low-dimensional formulation,” *J. Fluid Mech.*, vol. 538, pp. 199–222, 2005.

- [25] B. Scheid, C. Ruyer-Quil, S. Kalliadasis, M. Velarde, and R. Zeytounian, “Thermocapillary long waves in a liquid film flow. part 2. linear stability and nonlinear waves,” *J. Fluid Mech.*, vol. 538, pp. 223–244, 2005.
- [26] J. Pascal, “Linear stability of fluid flow down a porous inclined plane,” *J. Phys. D: Appl. Phys.*, vol. 32, pp. 417–422, 1999.
- [27] S. Beavers and D. Joseph, “Boundary conditions at a naturally permeable wall,” *J. Fluid Mech.*, vol. 30, pp. 197–207, 1967.
- [28] P. Saffman, “On the boundary condition at the interface of a porous medium,” *Stud. Appl. Maths*, vol. 1, pp. 93–101, 1971.
- [29] R. V. Craster and O. K. Mater, “Dynamics and stability of thin liquid films,” *Reviews of Modern Physics*, vol. 81, pp. 1131–1198, 2009.
- [30] H. Squire, “On the stability for three-dimensional disturbances of viscous fluid flow between parallel walls,” *Proceedings of the Royal Society of London. Series A, Containing Papers of a Mathematical and Physical Character*, vol. 142, no. 847, pp. 621–628, 1933.
- [31] P. Gent, “The energetically consistent shallow water equations,” *Journal of the Atmospheric Sciences*, vol. 50, pp. 1323 – 1325, 1993.
- [32] R. LeVeque, *Finite volume methods for hyperbolic problems*. Cambridge University Press, 2002.
- [33] S. D’Alessio and J. Pascal, “Simulating flows over wavy inclined surfaces,” *The 2009 International Conference on Scientific Computing CSC 2009 Meeting*, vol. July 13-16, no. Las Vegas, USA, 2009.
- [34] R. LeVeque and H. Yee, “A study of numerical methods for hyperbolic conservation laws with stiff source terms,” *Journal of Computational Physics*, vol. 86, pp. 187–210, 1990.
- [35] ANSYS, *ANSYS CFX Solver Theory Guide, ANSYS CFX Release 11.0*. ANSYS Europe, Ltd., 2006.
- [36] P. Zwart, *Numerical modelling of free surface and cavitating flows*. VKI Lecture Series, ANSYS Canada Ltd, 2005.
- [37] J. Brackbill, D. Kothe, and C. Zemach, “A continuum method for modelling surface tension,” *Journal of Computational Physics*, vol. 100, pp. 335–354, 1992.

- [38] K. Ogden, S. D'Alessio, and J. Pascal, *Advances in Fluid Mechanics VIII, Vol. 69*, ch. Modelling gravity-driven flow over uneven surfaces, pp. 299–309. Southampton, UK: WIT Press, 2010.
- [39] M. LeBars and M. Worster, “Interfacial conditions between a pure fluid and a porous medium: Implications for binary alloy solidification,” *J. Fluid Mech.*, vol. 550, pp. 149–173, 2006.
- [40] R. Johnson, *The handbook of fluid dynamics*. CRC Press LLC, 1998.
- [41] T. Benjamin, “The development of three-dimensional disturbances in an unstable film of liquid flowing down an inclined plane,” *J. Fluid Mech*, vol. 10, pp. 401–419, 1961.